LINKING AEROSOL HYGROSCOPICITY, VOLATILITY, AND OXIDATION WITH CLOUD CONDENSATION NUCLEI ACTIVITY: FROM LABORATORY TO AMBIENT PARTICLES

A Thesis
Presented to
The Academic Faculty

by

Kate M. Cerully

In Partial Fulfillment
of the Requirements for the Degree
Doctor of Philosophy in the
School of Chemical and Biomolecular Engineering

Georgia Institute of Technology
May 2014

LINKING ORGANIC AEROSOL VOLATILITY WITH CLOUD CONDENSATION NUCLEI ACTIVITY AND HYGROSCOPICITY: FROM LABORATORY TO AMBIENT PARTICLES

Approved by:

Dr. Athanasios Nenes, Advisor
School of Chemical and Biomolecular Engineering and School of Earth and Atmospheric Sciences
Georgia Institute of Technology

Dr. Greg Huey
School of Earth and Atmospheric Sciences
Georgia Institute of Technology

Dr. Nga L. Ng
School of Chemical and Biomolecular Engineering and School of Earth and Atmospheric Sciences
Georgia Institute of Technology

Dr. Rodney Weber
School of Earth and Atmospheric Sciences
Georgia Institute of Technology

Dr. Michael Filler
School of Chemical and Biomolecular Engineering
Georgia Institute of Technology

Date Approved: December 19, 2013

Dedicated to my loving family and friends…

ACKNOWLEDGEMENTS

I sincerely thank all of my family and friends for their unceasing support throughout this journey. To my family, thank you for listening, for offering guidance, and for continuing to love me even when I don't listen. Mom and dad, there are no words to express my thankfulness and love for you. Jenn, Jon, Laura, and David, I'm grateful for, among other things, your patience and humor. Laura, David, Kristen, and Brad, I'm so thankful for the time we shared when you lived in Atlanta and for being my support group as I moved to a new city and stage in life. To my friends from Atlanta Westside, you have provided such an amazing outlet for me, grounded in faith and love for God and for other people. Anna Banana and Felicia, I'm so thankful for your dear friendships. To the Heck, Pittman, Pettit, Stone, Teachey, DeBardeleben, Henegar, Cruz, Crews, Sayler, Hasner, Cox, Pearson, Gloria, Gunn, and Gilbert families, thank you for taking me in as part of your families, for sharing your children with me, and for taking interest in my wellbeing. I am encouraged by your love and generosity and, of course, by the amazing experience of getting to see life through your children's eyes. To Amanda and Will, my sweet Atlanta parents, thank you for your constant presence in my life and for making sure I never spend a holiday without family.

I'd also like to express my gratitude to all of the people who have made this work possible and spent countless hours advising, encouraging, helping, and enlightening me. I am especially thankful for to get my hands dirty in the lab and the opportunity to explore aerosol instrumentation. Thank you to my thesis and thesis proposal committee members for providing input, ideas, and, in several cases, collaborating on research projects. I'd

like to thank Josie Giles for her support and cheerleading. To Dave Tanner, thank you for your assistance in building and understanding electronic systems, always with patience and a smile. Thank you to collaborators from the Carnegie Mellon University CAPS lab, Rutgers University, NOAA, and Georgia Tech. Thank you to my undergraduate professors, especially Dr. Shannon, for helping me believe that I could make it through graduate school and for countless recommendation letters. And, of course, thank you to my fellow group members throughout the years for sharing your knowledge, stories, and baked goods with me. Thanks especially to James for your contributions to the thermodenuder model development, Molly and Rich for your help in the construction of the thermodenuder, and Tomi for your contributions to the Hyytiälä dataset. Finally, a very special thank you goes to Shannon, Terry, Ricardo, and Katerina, for your assistance throughout grad school, and most of all, for being good friends along the way.

TABLE OF CONTENTS

LIST OF TABLES

LIST OF FIGURES

SUMMARY

The indirect effect of atmospheric aerosol on climate remains a large source of uncertainty in anthropogenic climate change prediction. An important fraction of this uncertainty arises from the impacts of organic compounds on cloud droplet formation. This research investigates the link between aerosol volatility, hygroscopicity, and oxidation with cloud condensation nuclei (CCN) activity. Data were collected from a variety of laboratory and ambient studies and supplemented with the new construction and evaluation of a thermodenuder, an instrument designed to probe aerosol volatility. Conventional thinking says that organic aerosol hygroscopicity, typically represented by the hygroscopicity parameter κ, increases with oxidation, most commonly represented by the oxygen to carbon ratio of the aerosol, O:C. Results, though, indicate that the link between organic aerosol hygroscopicity and oxidation is not always straightforward. In some of these cases, though, the relationship may be due to the use of O:C as a measure of oxidation, and the average carbon oxidation state, $\overline{OS}_c$, appears to be a better indicator of oxidation. The link between organic aerosol hygroscopicity and oxidation has been further extended to include the relationship with aerosol volatility – organic aerosol hygroscopicity and oxidation are expected to increase as aerosol volatility decreases. In chamber and ambient studies, the least volatile fraction of the aerosol also appeared to be the least hygroscopic, contradictory to current thinking; however, in both cases, thermally-denuded aerosol showed greater oxidation, in terms of $\overline{OS}_c$, than non-denuded aerosol, most likely due to the presence of gas-phase surfactants or oligomers. Thermal-denuding of ambient aerosol had only a small impact on the total aerosol hygroscopicity

(relative change in κ < 12%) for mass losses as high as approximately 35%. While the relationship between organic aerosol hygroscopicity, oxidation, and volatility may not always be straightforward within individual studies, when placed in the context of numerous published studies from a variety of different environment, the overall trend of increasing organic hygroscopicity with O:C still holds. This is also true for volatilized aerosol, though the magnitude of organic hygroscopicity is generally lower than that of non-denuded aerosol. These findings illuminate the need for better understanding of oxidative process on aerosol and further study of the effects of volatility on aerosol properties, in order to determine to what degree the proposed relationship of increased organic aerosol hygroscopicity and oxidation with decreased volatility may hold true in the ambient.

CHAPTER 1

INTRODUCTION

1.1 AEROSOL-CLOUD-CLIMATE INTERACTIONS

Atmospheric aerosol directly affect climate through scattering and absorbing solar radiation and indirectly affect climate by acting as cloud condensation nuclei (CCN; Twomey, 1974, 1977). The ability of aerosol to act as CCN, based on their size and chemical composition (Section 1.2), affects the concentration of cloud droplets and therefore, the albedo, or reflectivity, of clouds. This indirect effect of aerosol is illustrated in Figure 1.1 where, for a clean environment, there are few particles and few CCN, resulting in a cloud with fewer droplets. In contrast, a relatively polluted environment with more particles and more CCN will result in a cloud with more droplets and thus, higher albedo (Figure 1.1). The aerosol indirect effect is one of the largest sources of negative radiative forcing, or global cooling, on Earth's climate and remains a large source of uncertainty in climate change predictions (Figure 1.2; IPCC, 2007; IPCC, 2013).

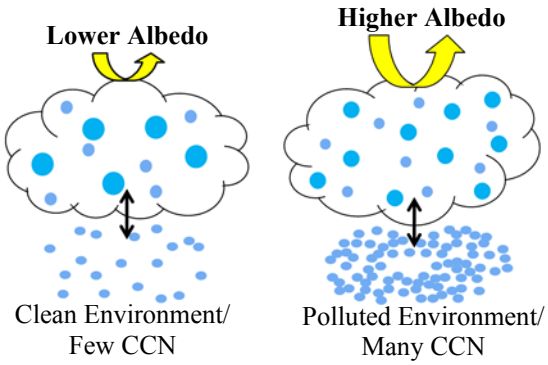

Figure 1.1: Illustration of the aerosol indirect effect and the impact of CCN concentration on cloud albedo. Small circles represent aerosol particles acting as CCN while larger blue circles represent cloud droplets.

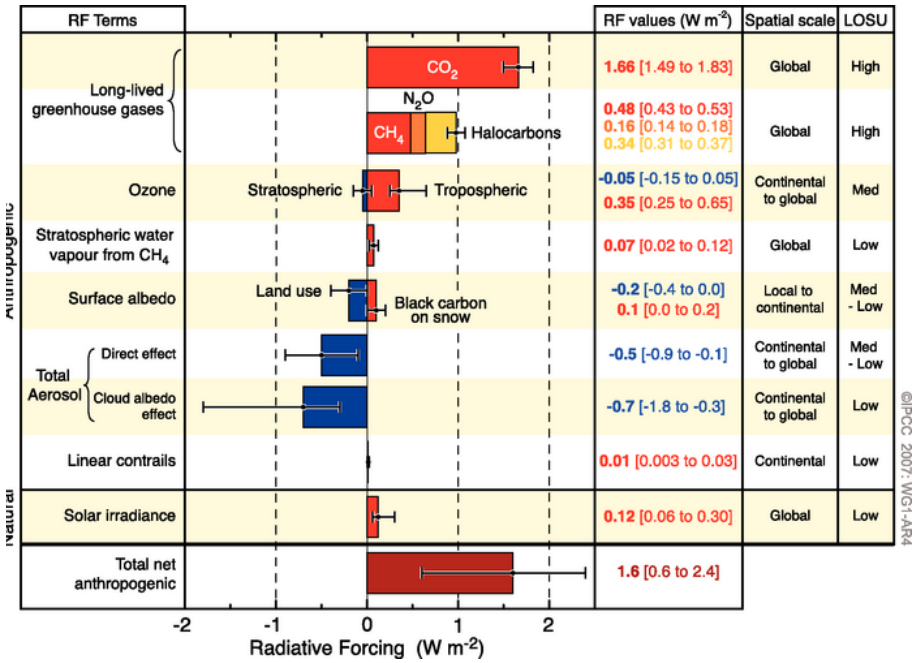

Figure 1.2: Key components of global radiative forcing (IPCC, 2007) and the corresponding level of scientific understanding (LOSU) of each component.

1.2 HOW AEROSOL ACT AS CLOUD CONDENSATION NUCLEI

1.2.1 Köhler Theory

Prediction of CCN activity for inorganic compounds, based on particle size and composition, was developed by Köhler in the late 1930s (Köhler, 1936). Köhler theory uses thermodynamic arguments to describe how changes in droplet curvature, known as the Kelvin effect, and the amount of solute, known as the Raoult effect, impact the equilibrium vapor pressure of a droplet,

$$\ln \mathrm{S} = \ln\left(\frac{P_w}{P_w^o}\right) = \frac{A}{D_p} - \frac{B}{D_p^3} \tag{1.1}$$

$$A = \frac{4M_w\sigma_w}{RT\rho_w}, \mathrm{B} = \frac{6n_sM_w}{\pi\rho_w}$$

where A and B are the Kelvin and Raoult terms, respectively. S is the equilibrium saturation ratio, P_w is the water vapor pressure over the droplet, P_w^o is the saturated water

vapor pressure over a flat surface, M_w is the molecular weight of water, σ_w is the surface tension of water, R is the universal gas constant, T is the temperature of the droplet, ρ_w is the density of water, D_p is the droplet diameter, and n_s is the moles of solute in the droplet, for a particle of a certain dry diameter (Seinfeld and Pandis, 2006). An example of Kelvin and Raoult effects and the equilibrium Köhler curve for a 50 nm ammonium sulfate particle is shown in Figure 1.3.

At the maxima of the Köhler curve, particles reach a critical saturation, S_c, where they become "activated" and grow into a cloud droplet, corresponding to a critical wet diameter, D_{pc}. As an extension of Equation (1.1), the critical saturation can be expressed in terms of dry aerosol particle diameter, also known as the critical diameter, $d_{p,c}$, as

$$\ln S_c = \left(\frac{4A^3}{27B}\right)^{\frac{1}{2}} = \left(\frac{4A^3\rho_w M_s}{27\nu\rho_s M_w d_s^3}\right)^{\frac{1}{2}} \tag{1.2}$$

where ρ_s is the density of the particle, M_s is the molecular weight of the particle, and d_s is the solute dry particle diameter. ν is the van't Hoff parameter, describing the number of ions resulting from the dissociation of one molecule of solute (Seinfeld and Pandis, 2006).

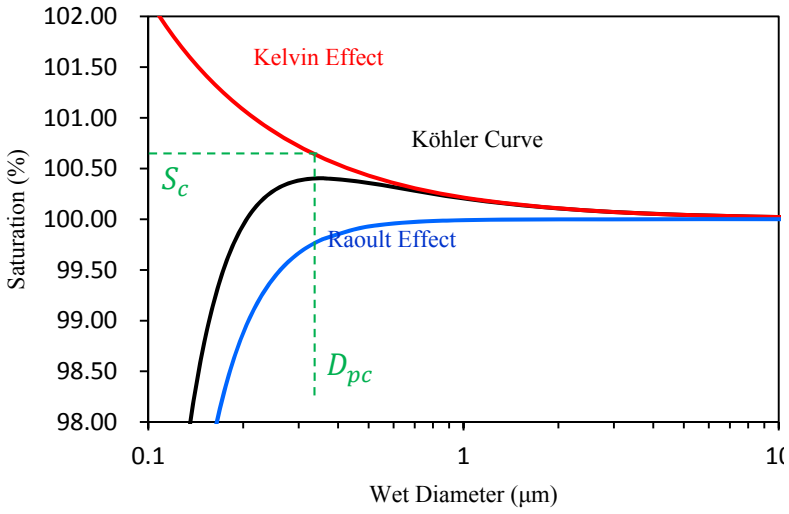

Figure 1.3: Köhler curve for a 50 nm ammonium sulfate particle at 293 K.

1.2.2 κ-Köhler Theory

While aerosol particles composed of inorganic salts (e.g. NaCl and $(NH_4)_2SO_4$) are considered to be the most effective at forming CCN and are well described by Köhler Theory, it is well known that aerosol can contain significant amounts of organic matter carbonaceous aerosol and are also efficient CCN. With estimates of 10,000 to 100,000 different organic species having been measured in the atmosphere (Goldstein and Galbally, 2007; Hallquist et al., 2009) and the effects they have on surface tension depression of droplets (e.g., Shulman et al., 1996; Li et al., 1998; Raymond and Pandis, 2002; Padró et al., 2010), it is extremely difficult to know the exact physical properties of a typical aerosol in the atmosphere. Petters and Kreidenweis (2007) proposed the use of a single hygroscopicity parameter, κ, which represents a scaled water-soluble volume fraction of a given aerosol or aerosol population and can be expressed by

$$\kappa = \frac{M_w \rho_s}{\rho_w M_s} \nu \varepsilon_s, \tag{1.3}$$

allowing Equation (1.2) to be rewritten as

$$\ln S_c = \left(\frac{4A^3}{27 \kappa d_p^3} \right)^{\frac{1}{2}}. \tag{1.4}$$

Pure salts, then, have high relative κ values (e.g., κ=0.6 for $(NH_4)_2SO_4$ and κ=1.2 for NaCl) while organic compounds typically have κ values between 0.1 and 0.3 (Petters and Kreidenweis, 2007).

As ambient aerosol are composed of many different compounds, it is often useful to investigate contributions from key aerosol components to the total aerosol hygroscopicity. This can be done by describing the hygroscopicity parameter κ by a volumetric mixing rule

$$\kappa = \sum_i \varepsilon_i \kappa_i \quad (1.5)$$

where ε_i and κ_i are the volume fraction and hygroscopicity of species i, respectively (Petters and Kreidenweis, 2007). Organic aerosol hygroscopicity, κ_{org}, for example, can be investigated by dividing the aerosol into its contribution from organic, *org*, and inorganic, *inorg*, compounds.

$$\kappa = \varepsilon_{org}\kappa_{org} + \varepsilon_{inorg}\kappa_{inorg}. \quad (1.6)$$

1.3 ORGANIC AEROSOL VOLATILITY

1.3.1 Secondary Organic Aerosol

Adding to the complexity of the contributions of organic species to aerosol composition, a large fraction of atmospheric organic species are secondary organic aerosol (SOA) (e.g., Goldstein and Galbally, 2007; Jimenez et al., 2009; Hallquist et al., 2009; Donahue et al., 2009), which are semi-volatile compounds formed from oxidation of gas-phase organic precursors emitted from biogenic and anthropogenic sources. These semi-volatile species partition between the gas and particle phase; thus, they can largely impact aerosol mass and composition and contribute to CCN activity (e.g., Novakov and Penner, 2003; Sun and Ariya, 2006; Kanakidou et al., 2005; Petters and Kreidenweis, 2007; Ervens et al., 2011). Much of this material, through atmospheric processing, is transformed into hygroscopic compounds that increase the CCN activity of particles, such as monocarboxylic and dicarboxylic acids (e.g., Yu, 2000; Seinfeld and Pandis, 2006; Sun and Ariya, 2006). It has also been found that SOA can be formed via the aqueous particle phase (e.g., Ervens et al., 2011). Recent estimates of SOA production range from 140 to 540 Tg C/yr up to 510 to 910 Tg C/yr (Goldstein and Galbally, 2007), illustrating the

large range of uncertainty and the need for better understanding of SOA and its impact on aerosol properties.

1.3.2 Aerosol Volatility Framework

Aerosol partitioning between the aerosol and gas phase can be described by

$$\xi_i = \left(1 + \frac{c_i^*}{c_{OA}}\right)^{-1} \tag{1.7}$$

where the partitioning coefficient, ξ_i, represents the mass fraction of a particular compound i found in the condensed (aerosol) phase, c_i^* is the effective saturation concentration (proportional to the saturation vapor pressure), and c_{OA} is the total mass concentration of organic aerosol (Donahue et al., 2006). This partitioning can be used to describe aerosol at a number of saturation concentrations as part of the volatility basis set approach proposed by Donahue et al. (2006) (Figure 1.4). Typically, c_i^* values are members of a prescribed vector of saturation concentrations with decadal spacing where

$$c_{OA} = \sum_i c_i \xi_i. \tag{1.8}$$

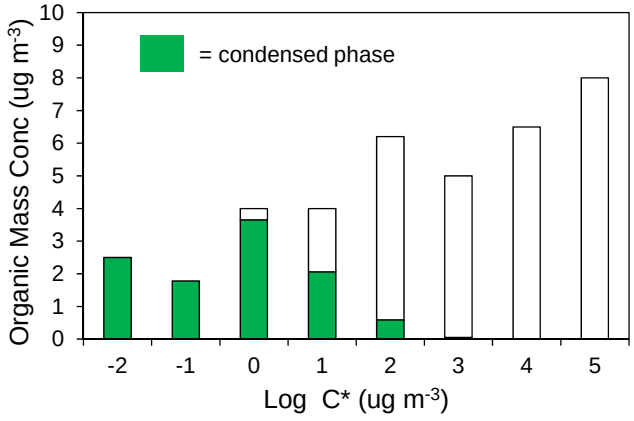

Figure 1.4: Example distribution of organic mass and partitioning for a series of saturation concentrations using the volatility basis set framework of Donahue et al. (2006).

1.4 AEROSOL OXIDATION

Aerosol oxidation measurements are used to represent the ageing of aerosol in Earth's oxidizing atmosphere. Typically, aerosol oxidation is represented by the ratio of oxygen to carbon, or O:C, of the aerosol (e.g., Jimenez et al., 2009). Aerosol oxidation is also commonly represented by f_{44}, the fraction of the m/z 44 peak to the total signal measured by aerosol mass spectrometry, where the m/z 44 peak represents the CO_2^+ fragment of the aerosol (e.g., Aiken et al., 2008; Ng et al., 2010). O:C and f_{44} have been shown to correlate linearly (Aiken et al., 2008). Recently, however, it has been shown that the average carbon oxidation state, $\overline{OS}_C$, calculated as 2*O:C-H:C where H:C is the hydrogen to carbon ratio of the aerosol, may be a better indicator of oxidative processes (Kroll et al., 2011; Xu et al., *in review*). This is illustrated by the comparison of oxidation state and O:C during methane oxidation in Figure 1.5 (modified from Kroll et al., 2009b) where oxidation state continuously increases, the O:C ratio remains constant across three oxidation steps.

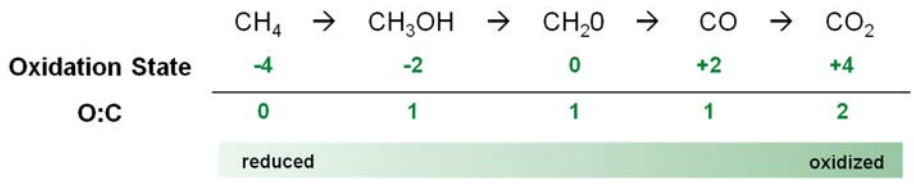

Figure 1.5: Aerosol oxidation state versus O:C during methane oxidation.

1.5 PROPOSED RELATIONSHIPS BETWEEN AEROSOL HYGROSCOPICITY, OXIDATION, AND VOLATILITY

The link between organic aerosol hygroscopicity and oxidation was proposed by Jimenez et al. (2009), where results from a number of laboratory and ambient studies showed that organic aerosol hygroscopicity increases with O:C (Figure 1.6) based on the idea that as

compounds are more oxidized, they become more functionalized and more polar, resulting in an increased affinity for water. While this is true in many cases (e.g., Jimenez et al., 2009; Chang et al., 2010; Lambe et al., 2011) the proposed relationship is not always clear as illustrated by a number of studies of both laboratory and ambient studies (e.g., Massoli et al., 2010; Frosch et al., 2011; Tang et al., 2012; Alfarra et al., 2013; Lathem et al., 2013).

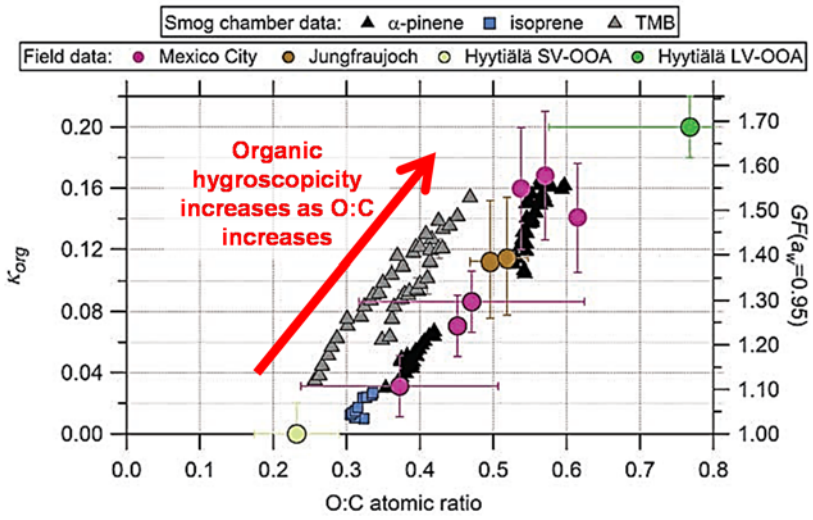

Figure 1.6: Proposed relationship from Jimenez et al. (2009) between organic aerosol hygroscopicity (κ_{org}), (from CCN measurements or growth factor, GF) and oxidation (O:C).

It has been further proposed that organic aerosol hygroscopicity and O:C may be also be linked with aerosol volatility (Jimenez et al., 2009), though very few studies have investigated the relationship between all three of these properties or found conclusive evidence of a relationship between volatility and oxidation (Poulain et al., 2010; Tritscher et al., 2011; Hong et al., 2013). The proposed relationship is based on the concept that as compounds become more oxidized and increase their affinity for water, their saturation vapor pressure (i.e., volatility) is also decreased. Figure 1.7 illustrates the proposed

linkages of Jimenez et al. (2009) in the form of a 2-dimensional volatility basis set framework.

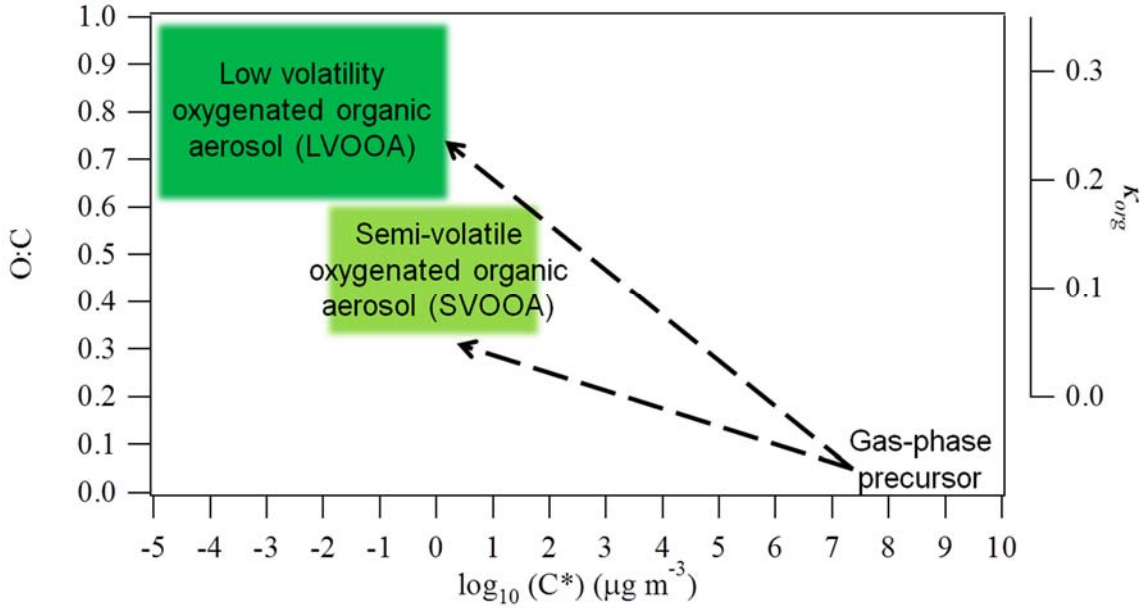

Figure 1.7: Proposed relationship between organic aerosol hygroscopicity (κ_{org}), oxidation (O:C), and volatility (C*). Figure modified from Jimenez et al. (2009).

CHAPTER 2

CCN MEASUREMENT METHODS

2.1 CFSTGC INSTRUMENT OPERATION

Cloud condensation nuclei (CCN) activity is measured using a Continuous-Flow Streamwise Thermal Gradient Chamber (CFSTGC), often referred to as a CCN counter or CCNc (Roberts and Nenes, 2005; Lance et al., 2006). The instrument was developed by Roberts and Nenes (2005) and is available commercially from Droplet Measurement Technologies (DMT). The CCNc consists of a cylindrical, ceramic column saturated with water. A temperature gradient, referred to as ΔT, is applied along the column walls, from cold to hot, and uses the principle that water vapor diffuses faster than heat in air in order to create a supersaturation, *s*, at the centerline of the column (Figure 2.1). Aerosol particles activate in the instrument if their critical supersaturation is greater than the supersaturation in the instruments (see Section 1.2). A condensation particle counter (CPC; TSI, Inc.) placed before the CFSTGC is typically used to measure the concentration of particles or condensation nuclei (CN) entering the CFSTGC, while an optical particle counter (OPC) at the exit of the column measures the concentration of particles that have activated into droplets with diameter > 1 μm, which are classified as CCN. The supersaturation profile in the instrument is mainly dependent on the temperature gradient along the wall, the flow rate in the chamber, and the instrument pressure, each of which can be controlled to allow for a dynamic range of operating conditions (Lance et al., 2006; Moore and Nenes, 2009). The typical methods of operation are “constant supersaturation mode” (Lance et al., 2006), “Scanning Mobility

CCN Analysis (SMCA) mode" (Moore et al., 2010), and "Scanning Flow CCN Analysis (SFCA) mode" (Moore and Nenes, 2009). As only constant supersaturation and SFCA modes are used in this thesis, the following will focus on only those two methods.

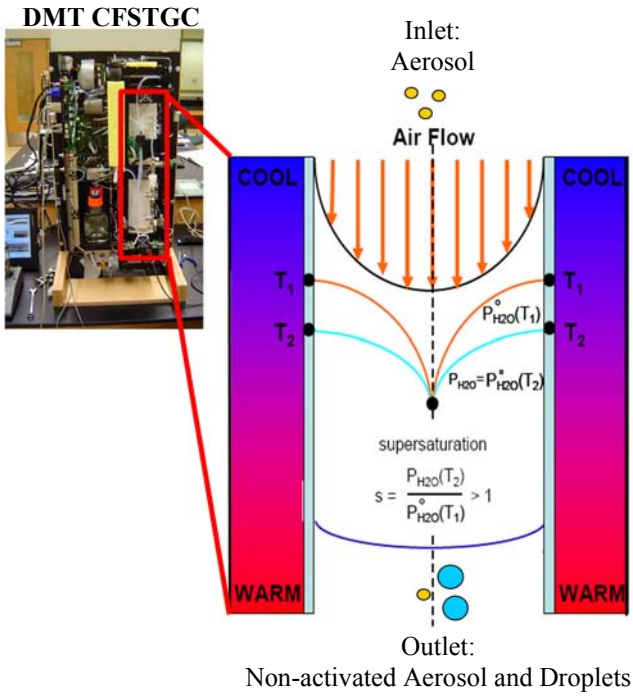

Figure 2.1: Commercial CFSTGC by DMT (left; Roberts and Nenes, 2005) and illustration of the operating principles of the cylindrical ceramic column in the instrument (right).

Using the most commonly used method of operation, constant supersaturation mode, supersaturation in the instrument is held constant for a period of time and is then stepped to a new supersaturation (e.g., Petters and Kreidenweis, 2007; Bougiatioti et al., 2009; Gunthe et al., 2009; Petters et al., 2009a; Rose et al., 2010; Cerully et al., 2011; Lack et al., 2011; Lathem and Nenes, 2011; Moore et al., 2011; 2012b; Chapter 3). Constant supersaturation is achieved by holding the flow rate, ΔT, and pressure constant in the instrument; supersaturation is typically then stepped by stepping ΔT. The relationship between the selected flow rate, ΔT, and pressure, and supersaturation is determined through instrument calibration (see Section 2.3). Particles are typically size-selected

upstream by a differential mobility analyzer (DMA; TSI, Inc.) and counted using a CPC. SMCA mode similarly employs constant supersaturation in the instrument, but additionally operates the DMA and CPC upstream as a Scanning Mobility Particle Sizer (SMPS) which, rather than selecting a single size of particle, scans through the polydisperse aerosol distribution over approximately 1 to 2 minutes (e.g., Padró et al., 2007, 2010; Asa-Awuku et al., 2009; 2010; Engelhart et al., 2008; Lathem et al., 2011; Lathem and Nenes, 2011; Moore et al., 2008; 2011; Schwier et al, 2011; Chapter 3 for calibration only). Alternatively, SFCA mode scans the supersaturation in the instrument by scanning the flow rate in the instrument, where the relationship between supersaturation and flow rate are determined by instrument calibration (Section 2.3), allowing for fast measurements of CCN activity across a range of supersaturations; SFCA measures CCN spectra over timescales of approximately 10 to 60 seconds while constant supersaturation mode and SMCA typically require about 3 to 5 minutes or more per supersaturation (Moore and Nenes, 2009). SFCA can be used to measure both size-selected (e.g., Cerully et al., 2013; Chapter 4, Chapter 5) and polydisperse aerosol (e.g., Moore et al, 2012a; Chapter 6).

2.2 ANALYSIS OF CCN ACTIVATION SPECTRA

The key parameter determined from CCN analysis in the following studies is the hygroscopicity parameter, κ (Petters and Kreidenweis, 2007). In order to determine κ, the dry diameter, d_p, and critical supersaturation, s_c, must be determined by CCN measurements (see Section 1.2). How these parameters are determined depends on the instrument operation mode used. In constant supersaturation mode, aerosol entering the CFSTGC are size-resolved, thus d_p is set. As s is stepped in the instrument, this allows for

finding an activated fraction, or the concentration of CCN divided by the total possible CN for a number of supersaturations, known as a "CCN spectrum" (Figure 2.2). This CCN spectrum can be fit with a sigmoidal function in order to determine s_c, the supersaturation corresponding to the inflection point of the sigmoid where half of the total CN act as CCN.

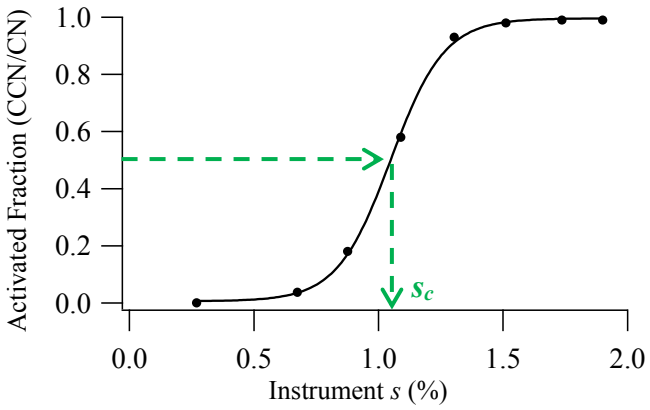

Figure 2.2: Example of a CCN spectrum obtained using constant supersaturation mode operation of the CFSTGC for a given particle size.

SMCA mode analysis employs the principle that for a given s_c, there also exists a single $d_{p,c}$ (see Equations (1.2) and (1.4)). Rather than changing supersaturation in the instrument, supersaturation is held constant while particle size is varied. As a result, a CCN spectrum can be achieved in terms of the dry diameter (Figure 2.3) rather than the instrument supersaturation (Figure 2.2). Again, the CCN spectrum can be fit with a sigmoidal function, in this case to determine $d_{p,c}$ at the inflection point of the fitted sigmoid.

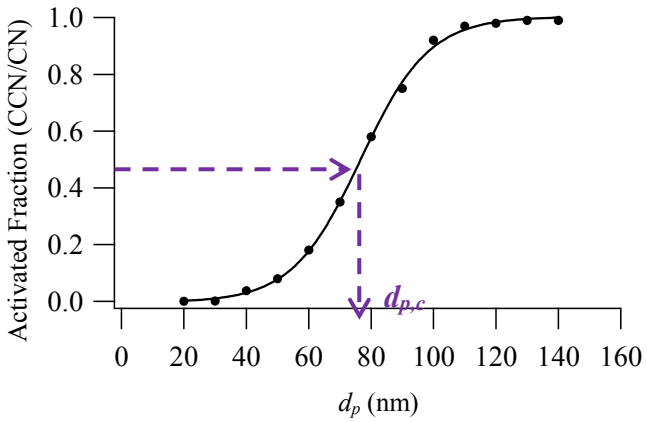

Figure 2.3: Example of a CCN spectrum obtained using SMCA mode operation of the CFSTGC for a given instrument supersaturation.

In SFCA mode, when using size-resolved aerosol, the method of determining s_c is nearly identical to that used for constant supersaturation mode, though in this case, rather than stepping through individual supersaturation, flow (and therefore supersaturation) is scanned in the instrument. As flow rate is related to supersaturation based on instrument calibration (described in the following section), the activation ratio can be plotted against instrument flow rate (Figure 2.4) or against supersaturation (e.g., Figure 2.2). In either case, CCN spectra can be fit with a sigmoidal function to obtain the critical flow rate, Q_c, or critical supersaturation.

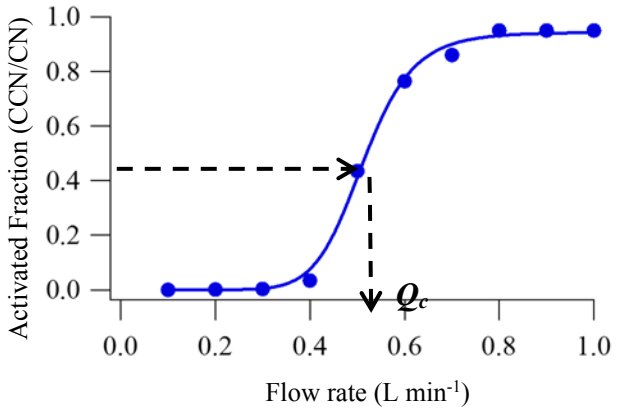

Figure 2.4: Example of a CCN spectrum obtained using size-resolved SFCA mode operation of the CFSTGC.

When using polydisperse aerosol measurements, however, the methodology for determining is determined quite differently as neither d_p or s are held constant. In polydisperse SFCA mode operation, aerosol again activate when their critical supersaturation is greater than s in the CFSTGC. In the case of polydisperse aerosol, though, different size particles will have a different s_c, a greater number of the total aerosol population will continually activate as the instrument s is increased (Technically, if a high enough s is reached in the instrument, all particles would potentially activate a sigmoidal function could be achieved for the entire aerosol population, though this is not the case for supersaturations measured for this method in Chapter 6). Thus, it is assumed that the s in the instrument is equal to the s_c of the activated particles. Since particles activate based on their size and chemical composition where size is the dominant indicator of activation (Dusek et al., 2006), the critical diameter, $d_{p,c}$, of the activated particle can be obtained by matching the concentration of CCN at a given s or s_c with the backwards integrated SMPS number distribution by (thus, the corresponding size bin and $d_{p,c}$; Figure 2.5) (described in further detail in Moore et al., 2011). This method operates under the assumption that aerosol with diameters larger than $d_{p,c}$ are internally-mixed.

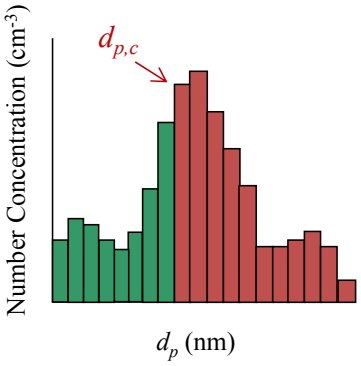

Figure 2.5: Illustration of the backwards integration of the total aerosol size distribution to obtain $d_{p,c}$ for polydisperse SFCA analysis. Dark red bars represent particles that are assumed to act as CCN.

2.3 CFSTGC CALIBRATION

Supersaturation in the CFSTGC, a function of flow rate, pressure, and ΔT, is determined by calibration with pure salt aerosol (e.g., $(NH_4)_2SO_4$ or NaCl), typically prior to and throughout each laboratory or field measurement campaign. Salt aerosol are atomized, dried using silica gel diffusion dryers, charge-neutralized, and then sampled depending on the desired CFSTGC operation mode (i.e., constant supersaturation, SMCA, or SFCA); for simplicity, calibrations for constant supersaturation and SFCA modes are typically performed using size-resolved aerosol, regardless of whether the aerosol being used for general measurements are size-resolved or polydisperse. Size-resolved constant supersaturation mode and SMCA mode calibration differ only in the fact that particle diameter is stepped in size-resolve constant supersaturation mode calibration but scanned in SMCA mode calibration. In each case, instrument conditions (i.e., flow rate, ΔT, and pressure) are held constant. The determined critical diameter (e.g., Figure 2.3) is related to the supersaturation in the instrument by Köhler Theory (Section 1.2.1); thus, the critical supersaturation, equivalent to the instrument supersaturation in the case of calibrations, can be determined by Equation (1.2) using the critical diameter and known calibration aerosol properties. This calibration method is repeated at unique ΔTs which correspond to unique supersaturations in order to determine and parameterize the relationship between ΔT and supersaturation in the instrument. For size-resolved SFCA mode calibrations, aerosol of a given size will activate at the flow rate equivalent to the aerosol critical supersaturation (Figure 2.4). Using Köhler Theory (Section 1.2.1), the critical supersaturation can again be determined by Equation (1.2) using the selected diameter and known calibration aerosol properties. As ΔT and pressure are held constant

in the instrument while flow rate continuously varies, the calibration method is repeated for a range of particle sizes in order to capture the flow rate-supersaturation relationship for the designated flow rate range.

2.4 CFSTGC INCLUSION IN A VARIETY OF EXPERIMENTAL SETUPS

CFSTGC measurements are able to useful and important information of aerosol properties in addition to hygroscopicity such as the chemical heterogeneity of the aerosol (Chapter 3), the mixing state of the aerosol population (Chapter 3), the potential impact of kinetic inhibitions on droplet growth (Chapter 3), and the presence of size-resolved chemical composition in the total aerosol (Chapters 3 and 6). The instrument can also be combined with other instruments in a variety of experimental setups (e.g., Figures 4.3, 5.1, and 6.1) to obtain a comprehensive view of aerosol behavior and composition. Throughout the following chapters, the CFSGTC is combined with Aerosol Mass Spectrometer (AMS; e.g., Jayne et al., 2000) measurements of aerosol composition to infer the hygroscopicity of only the organic portion of the aerosol (Chapters 3, 5, and 6) and the level of aerosol oxidation (Chapters 3, 5, and 6); with a thermodenuder (TD; e.g., Cerully et al., 2013) to measure the dependence of volatility on CCN properties (Chapters 4, 5, and 6); with Hygroscopicity Tandem Differential Mobility Analyzer (HTDMA; e.g., Liu et al., 1978) measurements of subsaturated hygroscopicity to investigate the effects of and differences between subsaturated versus supersaturated hygroscopicity measurements (Chapter 3); with environmental chamber measurements of atmospherically-relevant compounds to examine the hygroscopicity of secondary organic aerosol (SOA) ageing (Chapter 5); and with Particle-Into-Liquid Sampler (PILS; e.g., Weber et al., 2001; Orsini

et al., 2003) measurements to study the hygroscopic contributions of only the water-soluble fraction of the aerosol (Chapter 6).

CHAPTER 3

AEROSOL HYGROSCOPICITY AND CCN ACTIVATION KINETICS IN A BOREAL FOREST ENVIRONMENT DURING THE 2007 EUCAARI CAMPAIGN[1]

3.1 INTRODUCTION

Atmospheric aerosol are known to have a direct effect on climate through scattering and absorbing incoming solar radiation (IPCC, 2007). They also indirectly affect climate by acting as cloud condensation nuclei (CCN), and modifying cloud forcing and the hydrological cycle (Twomey, 1974, 1977). While it is generally thought that aerosol produce an overall cooling effect, the indirect effect remains a large source of uncertainty in predictions of anthropogenic climate change (e.g., IPCC, 2007). For this reason, the study of aerosol and their CCN properties is necessary for an improved understanding of aerosol-cloud-climate interactions.

The ability of an aerosol particle to act as CCN depends on both its size and composition (Köhler, 1936; Seinfeld and Pandis, 2006). Köhler theory uses thermodynamic arguments to describe how changes in curvature (known as the Kelvin effect) and the amount of solute (known as the Raoult effect) impact the equilibrium vapor pressure of a droplet. Using this theory, the critical supersaturation, above which an aerosol particle "activates" spontaneously into a cloud droplet, can be predicted. While originally developed for inorganic salts, Köhler theory can be extended to include effects of organics through their contribution of solute and surface tension depression (e.g.,

[1]This chapter published as: Cerully, K. M., Raatikainen, T., Lance, S., Tkacik, D., Tiitta, P., Petäjä, T., Ehn, M., Kulmala, M., Worsnop, D. R., Laaksonen, A., Smith, J. N., and Nenes, A.: Aerosol hygroscopicity and CCN activation kinetics in a boreal forest environment during the 2007 EUCAARI campaign, Atmos. Chem. Phys., 11, 12369-12386, doi:10.5194/acp-11-12369-2011, 2011. Republished under the Creative Commons Attribution 3.0 license.

Shulman et al., 1996; Li et al., 1998; Raymond and Pandis, 2002). κ-Köhler theory (Petters and Kreidenweis, 2007) parameterizes solute contribution in terms of a single hygroscopicity parameter, κ, and represents a "scaled" volume fraction of soluble material in the particle (Lance, 2007; Padró et al., 2010). Typical soluble salts found in the atmosphere such as ammonium sulfate or sodium chloride have values of $\kappa \approx 0.6$ and $\kappa \approx 1.2$, respectively (Petters and Kreidenweis, 2007), while $\kappa = 0$ corresponds to a completely insoluble particle. Lab and field studies show that κ of secondary organic aerosol (SOA) typically ranges between 0.1 and 0.2 (e.g., Prenni et al., 2007; Gunthe et al., 2009; Dusek et al., 2010; Engelhart et al., 2008, 2011; Asa-Awuku et al., 2009, Sihto et al., 2010), although the water-soluble fraction extracted from a range of SOA systems and biomass burning exhibits $\kappa \approx 0.3$ (Asa-Awuku et al., 2010; Padró et al., 2010; Engelhart et al., 2008, 2011). For many locations, on average, κ values for continental and marine aerosol have been typically found to be 0.3 ± 0.2 and 0.7 ± 0.2, respectively (e.g., Andreae and Rosenfeld, 2008; Pringle et al., 2010); however, assuming a constant κ can introduce a sizeable uncertainty in CCN number predictions (e.g., Chang et al., 2010; Pöschl, 2011).

Size-resolved CCN measurements offer unique insight on compositional dispersion and the processes that affect aerosol hygroscopicity (e.g., Lance, 2007; Padró et al., 2007, 2010; Gunthe et al., 2009; Petters et al., 2009a; Rose et al., 2010; Asa-Awuku et al., 2009, 2010; Mochida et al., 2010; Irwin et al., 2011; Bougiatioti et al., 2011). Petters et al. (2009a) found that κ from emissions of fresh biomass burning generally decreased with particle size, although varying κ distributions and several hygroscopic modes may occur. During the AMAZE-08 Campaign at a remote site in Brazil, Aitken mode particles

(~50 nm) had κ of 0.1, characteristic of the hygroscopicity of biogenic SOA, while accumulation mode (~200 nm) particles had an increased κ of 0.2, correlating with a 10% increase in sulfate (Gunthe et al, 2009; Pöschl et al., 2010). In Finokalia, Crete, however, Bougiatioti et al. (2011) found that smaller particles (40 nm) generally had κ about 0.1 units greater than that of larger particles (100 nm). While the previous studies showed strongly size-dependent hygroscopicity, Mochida et al. (2010) found that, for 34 particle sizes ranging from 24.1 to 359 nm sampled in Cape Hedo, Okinawa, Japan, the particles typically showed unimodal, high hygroscopicity likely due to internally mixed particles rich in ammonium sulfate.

Bulk and size-resolved measurements of aerosol composition are important for further deconvolving the effects of composition on CCN properties and behavior. In a study of CCN closure, Lance et al. (2009) showed that average CCN overprediction bias during the GoMACCS field mission in Houston, Texas, was reduced from 36% to 3% when bulk aerosol chemical composition from an Aerosol Mass Spectrometer (AMS) was included. Bougiatioti et al. (2009, 2011) obtained underprediction bias as low as 0.6±9% when including bulk composition measurements from analysis of PTFE and quartz filter samples in the eastern Mediterranean during the FAME07 campaign. While certain conditions or environments allow for a reasonable comparison of bulk composition data with smaller aerosol particles, this may not always be the case. Medina et al. (2007) overpredicted CCN by 35.8±28.5% in a CCN closure study when using AMS size-averaged chemical composition, but only 17.4±27.0% when using size-dependent composition during the ICARTT 2004 campaign at a rural site in New Hampshire. Gunthe et al. (2009) also found for a pristine tropical rainforest environment

that the high bias in predicted CCN to measured CCN was a result of using bulk rather than size-resolved AMS data. Beyond CCN closure, composition measurements are able to elucidate the physicochemical processes occurring in the atmosphere. For AMS measurements, in particular, while it is not possible to identify individual organic aerosol (OA) compounds from the measured mass spectra, a rough estimate of oxidation state can be derived from the mass fraction of the *m/z* 44 peak (CO_2^+) in the organic aerosol signal, f_{44}, originating mainly from decomposition of carboxyl groups during the ionization step in the AMS. f_{44} has been shown to correlate with *O/C* ratio in aerosol particles (Aiken et al., 2008) and the hygroscopicity of SOA-dominated aerosol (e.g., Jimenez et al., 2009; Raatikainen et al., 2010; Massoli et al., 2010). One can attribute the correlation between f_{44} and hygroscopicity to an increase of the water-soluble fraction of organic aerosol (Bougiatioti et al., 2009; Padró et al., 2010; Asa-Awuku et al., 2011).

Another uncertain aspect of cloud droplet formation is the impact of slowly-dissolving compounds, droplet surface films, and aerosol amorphous states on the activation kinetics of CCN. If present, kinetic inhibitions (beyond that expected from gas-to-particle mass transfer alone) could have an important impact on cloud droplet number and size distribution (e.g., Jensen and Charlson, 1984; Kulmala et al., 1993; Chuang et al., 1997; Nenes et al., 2001, 2002; Lance et al., 2004). Studies often detect the presence of CCN experiencing kinetic limitations by comparing the size of activated droplets against a standard of rapid activation (e.g., calibration salt CCN). Many studies have found little evidence of kinetic limitations (e.g., Chuang, 2003; Engelhart et al., 2008, 2011; Lance et al., 2009; Bougiatioti et al, 2009, 2011; Asa-Awuku et al., 2010; Padró et al., 2010), although others detected kinetic limitations when the aerosol originated from

above the boundary layer or contained a large fraction of hydrophobic organics (e.g., Sorooshian et al., 2008; Ruehl et al., 2008, 2009; Asa-Awuku et al., 2009, 2011). Padró et al. (2010) showed that the water-soluble organics in Mexico City during the MILAGRO campaign did not affect droplet growth rates. Asa-Awuku et al. (2009) showed that droplet growth kinetics were strongly anti-correlated with the water-soluble organic carbon fraction for β-caryophyllene SOA. Murphy et al. (2009) detected some kinetic limitations for organic-rich aerosol freshly emitted from a cargo ship. Lance et al. (2009) found that activation kinetics in the boundary layer were not greatly depressed over Houston, Texas, during the GoMACCS campaign, while Ruehl et al. (2008) and Asa-Awuku et al. (2011) found during the same campaign (but different location and time periods) that up to 30% of the CCN may exhibit some degree of delayed condensational growth. Bougiatioti et al. (2009, 2011) found that aged carbonaceous aerosol sampled at a remote marine site in the eastern Mediterranean during the 2007 Finokalia Aerosol Measurement Experiment (FAME07) did not exhibit kinetically limited droplet growth rates. Ruehl et al. (2009) found strong kinetic limitations above the marine boundary layer near the California coast. These studies encompass a large range of environments and conditions; however the prevalence of kinetic limitations varies even for similar environments, suggesting the need for further investigation.

Boreal forests, such as the one considered in this study, offer a unique and climatically-important environment for study as they cover 8% of the earth's surface (Sihto et al., 2010). Remote forests allow for looking at clean, "background" air masses with a strong dominance of biogenic SOA (Boy et al., 2004; Kulmala et al., 2004), illustrating the importance of interactions between the soil, ecosystem, and atmosphere

(Hari and Kulmala, 2005; Barth et al., 2005; Kanakidou et al., 2005). The frequent occurrence of nucleation events in boreal forests influences the aerosol properties of different size modes (Hämeri et al., 2001). CCN studies for this type of environment have investigated the diurnal variation of critical activation diameter, hygroscopicity, solubility, and the properties of characteristic particle sizes and modes (e.g., Aalto and Kulmala, 2000; Hämeri et al., 2001; Sihto et al., 2010). It is expected that the influence of particle formation events and secondary organic aerosol (SOA) production give rise to CCN rich in carbonaceous material, but with a small fraction of inorganic salts that further augments their hygroscopicity (Sihto et al., 2010).

Size-resolved CCN concentrations, subsaturated hygroscopic growth, size distribution, and chemical composition were measured at Hyytiälä, Finland, during March through May, 2007, as part of the EUCAARI campaign (see Kulmala et al., 2009). The current study utilizes these measurements in order to investigate size-dependent hygroscopicity and CCN activation kinetics of aerosol in a boreal forest environment. An emphasis is placed on the diurnal variation of aerosol mixing state and composition and their effects on aerosol hygroscopicity.

3.2 DATA COLLECTION

3.2.1 Measurement Site

Data were collected from a comprehensive suite of aerosol instrumentation at the SMEAR II station (61°51′ N, 24°17′ E) located in a boreal forest in Hyytiälä, Finland, from 25 March through 15 May 2007. This site is described in detail in Kulmala et al. (2001) and Hari and Kulmala (2005). In addition to size-resolved CCN, subsaturated hygroscopic growth, size distribution, and chemical composition, measurements of

temperature, wind direction, gas phase species concentrations, and particle size distributions were also collected. Hyytiälä receives air masses from a variety of sources and locations. The SMEAR II station sees both "clean" and "polluted" air masses which are often, but not always, characterized by low particle concentrations transported from the Arctic Ocean and northern Scandinavia and high particle concentrations transported from central and eastern Europe, respectively. An example of NOAA HYSPLIT backtrajectories (http://ready.arl.noaa.gov/HYSPLIT.php) characterizing clean and polluted air masses is shown in Figure 3.1.

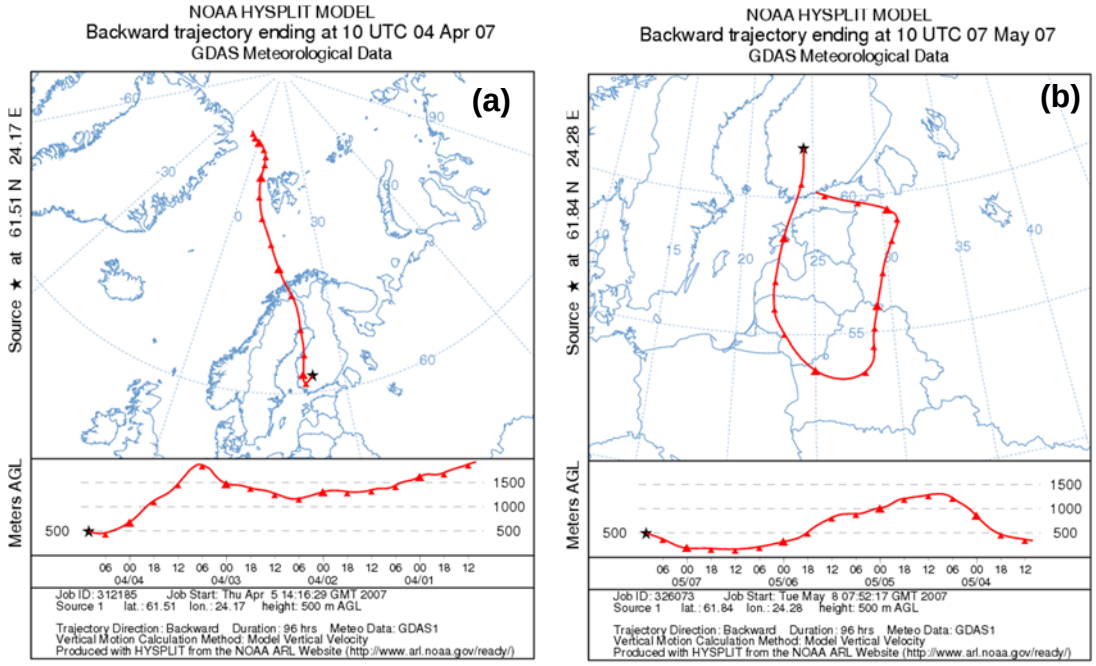

Figure 3.1: HYSPLIT backtrajectories for (a) clean and (b) polluted air masses.

3.2.2 Instrument Setup

A "stepping mode" setup for supersaturation and size (Lance, 2007; Moore et al., 2010) is used to obtain size-resolved CCN activity data. First, an ambient sample is introduced into a Differential Mobility Analyzer (DMA, TSI 3085). Dilution flow is then added to the classified aerosol stream before being split to a Condensation Particle Counter (CPC,

TSI 3760A), giving the total number of particles or condensation nuclei (CN) and to a Continuous Flow-Streamwise Thermal Gradient CCN Chamber (CFSTGC) (Roberts and Nenes, 2005; Lance et al., 2006) manufactured by Droplet Measurement Technologies, Inc. While supersaturation is held constant in the CFSTGC, the mobility diameter in the DMA is stepped to obtain measurements of CCN and CN concentration at several particle sizes. For each particle size, the ratio of CCN to CN concentration, known as the "activation ratio," is computed. This procedure is then repeated for several other supersaturations to characterize the size-dependent CCN activity of particles.

During this study, the supersaturation, *s*, in the CFSTGC is held constant over a period of 3 min, during which particles sizes of 20, 40, 60, 80, and 100 nm were selected by the DMA (e.g., Figure 3.2). Data collected up to 20 seconds after a change in DMA-selected particle size is discarded and the activation ratio is measured over a period of 16 s. The 20 nm and 100 nm data were discarded, because activation spectra were not fully detected at the selected instrument supersaturation range and also as the instrument transients had an effect on the 20 nm data. Instrument supersaturation was stepped in increments of ~0.2% ranging from ~0.1% to 1.8% for each particle size. An additional 3 min were allowed after switching from the highest to lowest supersaturation and data collected at the lowest supersaturation were discarded in order to allow sufficient time for the instrument supersaturation to reach the set point (e.g. Rose et al., 2008; Moore et al., 2010). This setup allowed for obtaining a cycle of size and supersaturation resolved CCN activity about every 30 min. The DMA was operated with a nominal aerosol flow rate of about 1 L min^{-1} and a sheath-to-aerosol flow rate ratio of ~4.5:1. Dilution flow of 1 L min^{-1} was introduced directly following the DMA. The CPC required a flow rate of 1 L

min^{-1}. The CFSTGC was operated at a total flow rate of 1 L min^{-1} with a sheath-to-aerosol flow rate ratio of ~10:1. Supersaturation in the instrument was calibrated with laboratory-generated ammonium sulfate particles using the Scanning Mobility CCN Analysis (SMCA) method described by Moore et al. (2010).

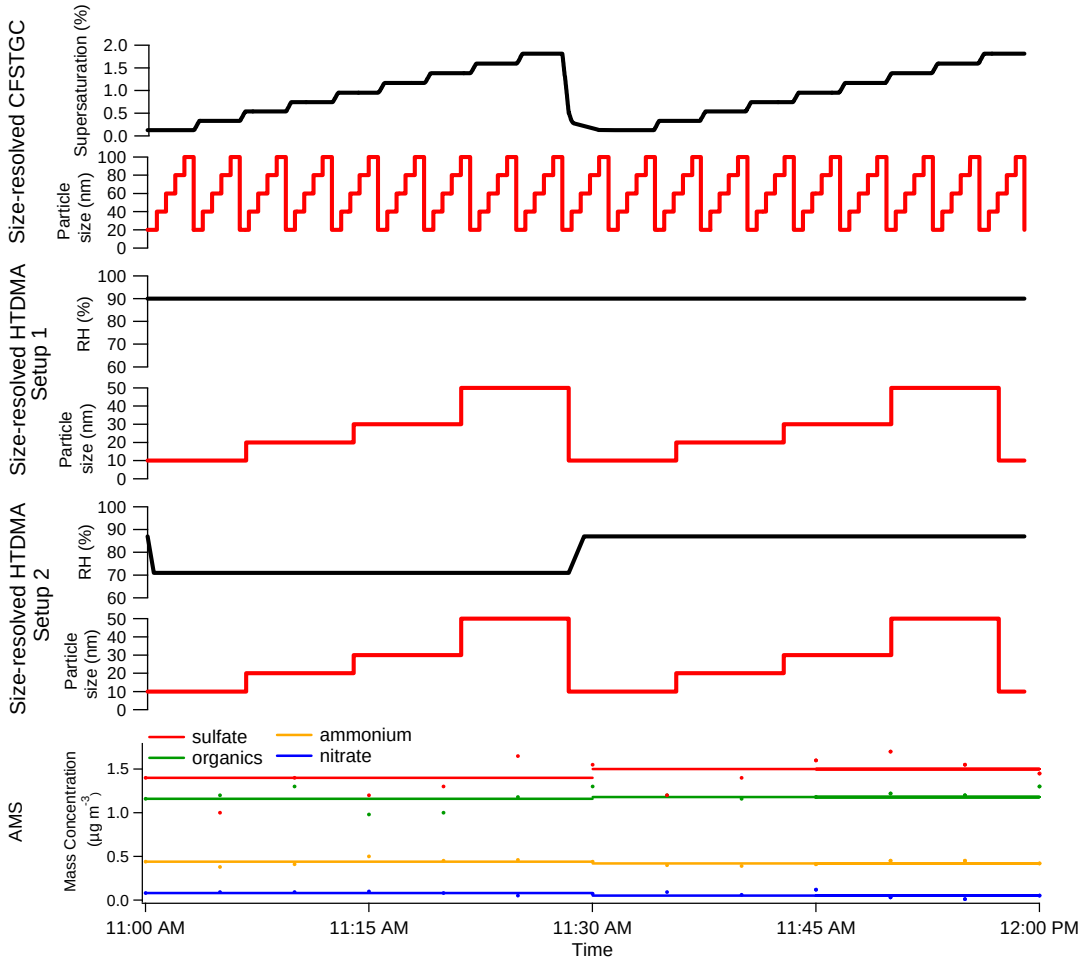

Figure 3.2: Example of the operation schedule for CFSTGC, HTDMA, and AMS measurements. A schematic of the HTDMA measurement schedules for data collected up to May 1 and after May 3 are indicated as Setup 1 and Setup 2, respectively. An example of actual data collected by AMS is represented by circles, while lines represent 30 minute averages used for this study.

The Hygroscopicity Tandem Differential Mobility Analyzer (HTDMA) measures the hygroscopic growth of size-classified particles exposed to a selected relative humidity (RH) below 100% (e.g., Liu et al., 1978; Rader and McMurry, 1986; Swietlicki et al.,

2008). The HTDMA used in the current study is fully described in Ehn et al. (2007), so only a brief description is given here. A first DMA unit is used to select a narrow size range from dried ambient particles. Then, the selected particles are exposed to a selected RH and the average growth of the humidified particles is measured by the second DMA unit and a CPC. A mean value representing average humid aerosol size is calculated from the humidified size distributions and is divided by the corresponding dry size to yield the hygroscopic growth factor (GF). The dry particle sizes of 10, 20, 30, and 50 nm, were selected by the first DMA in the HTDMA. These four particle sizes were stepped through over the course of approximately 30 min giving a single GF for each size every 30 min. Only the 30 and 50 nm data are shown for this study as they fall within the measured CCN data size range. For measurements collected up to 1 May, aerosol hygroscopic growth was measured at 90% RH. From 3 May through the end of the study, the RH was cycled between 71% and 87% each half hour (e.g., Figure 3.2).

Aerosol chemical composition was measured by an Aerodyne AMS (e.g., Jayne et al., 2000; Allan et al., 2003, 2004; Jimenez et al., 2003; Alfarra et al., 2004; Canagaratna et al., 2007). Briefly, the instrument is capable of detecting mass concentrations of non-refractory species from sub-micron aerosol with a time resolution of about 10 min (Jimenez et al., 2003; Canagaratna et al., 2007). “Non-refractory” refers to species that volatilize rapidly at 600°C, which means that crustal material, sea-salt, or black carbon aerosol cannot be detected. In practice, the AMS measures mass concentrations of non-sea-salt chloride, sulfate, nitrate, ammonium and organics (μg m−3). Initially, the AMS was operated by altering between particle time of flight (pTOF) and mass spectrum (MS) modes (e.g., Jimenez et al., 2003), saving data every 10 min. On 4 April, the AMS was

turned off and prepared for flux measurements (e.g., Nemitz et al., 2008). Starting from 6 April, the first 30 min of every hour was used for the flux measurements, and during the second 30 min period the AMS was alternating between pTOF, MS, and jump mass spectrum (JMS) modes (e.g., Crosier et al., 2007). In addition, averaging time was decreased to 5 minutes from the original value of 10 min. Mass concentrations were very noisy due to the short averaging time, so the AMS mass concentration (MS mode) data was averaged for each 30 min CCN measurement period (e.g., Figure 3.2). The data coverage for the 30 min time base is 47%. Most of the missing data points (42% of all data points) are due to the flux measurements, but some data points (11% of all data points) are missing due to routine maintenance and hardware failures.

3.3 METHODOLOGY

The CFSTGC and HTDMA provide hygroscopicity measurements under supersaturated and subsaturated conditions, respectively; each dataset can independently be used to derive κ distributions. Petters and Kreidenweis (2007) found that agreement between CCN-derived κ and HTDMA-derived κ is within 30% for most compounds considered in their study. Slight differences may occur between subsaturated and supersaturated κ values, as droplet solutions of activated particles in the CFSTGC are typically more dilute than if measured at subsaturated conditions (e.g., Petters and Kreidenweis, 2007; Asa-Awuku et al., 2010). For κ obtained at subsaturated conditions, solution non-ideality, phase separation, and partial solubility of constituents may be more pronounced and affect (mostly decrease) the observed κ. Therefore, the HTDMA and CFSTGC provide two independent measures of hygroscopicity under very different water activity conditions; together, these measurements are often used to test and confirm the validity of

experimental methods (e.g., Aalto and Kulmala, 2000; Good et al., 2010; Petters et al., 2009a; Sihto et al., 2010; Irwin et al., 2011).

From subsaturated HTDMA GF data for particles of dry diameter dp, κ values were predicted using

$$\kappa = (GF^3 - 1)\left(\frac{\exp\left(\frac{A}{GF\, d_p}\right)}{\frac{RH}{100\,\%}} - 1\right) \quad (3.1)$$

where $A=(4M_w\sigma_w)/(RT\rho_w)$, Mw is the molar mass of water, σ_w is the surface tension of water, R is the universal gas constant, T is temperature, and ρ_w is the density of water (Petters and Kreidenweis, 2007). Some GF values were removed from the analysis due to limited counting statistics at low particle concentrations based on an approximated background noise. The total percentage of GFs filtered from the analysis for the 30 and 50 nm datasets are ~14% and 10%, respectively. From the CCN data, the supersaturation-resolved activation ratio function, $R_a(s)$, for a given size particle is fit to a sigmoid with the form

$$R_a(s) = \frac{E}{1+\left(\frac{s}{s^*}\right)^C} \quad (3.2)$$

where E is the maximum fraction of particles that activate at high supersaturations, s is the instrument supersaturation, s^* is the characteristic critical supersaturation of the CCN population, the supersaturation at which half of the ambient CCN activate (i.e. $R_a(s)=0.5E$). C is a coefficient that is a measure of the slope of $R_a(s)$ and is affected by the chemical heterogeneity of the activated particles (Figure 3.3).

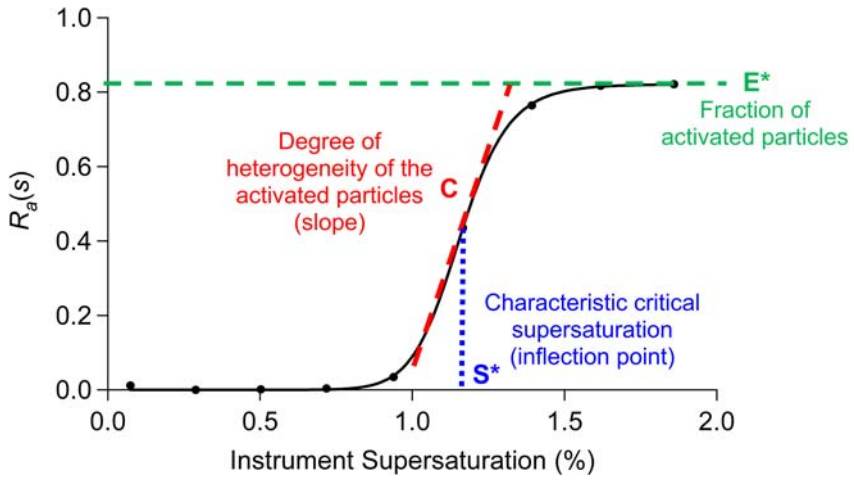

Figure 3.3: Example of an activation spectra and fitted parameters.

Before fitting to Equation (3.2), data were filtered for low CCN concentrations to avoid biases from insufficient counting statistics. This is done by applying Poisson statistics to describe the relative counting uncertainty as the inverse square root of the number concentration. Using the flow through the instrument during each 16 s measurement period, this number can be converted to a minimum acceptable concentration value. For the instrument setup used in this campaign, a relative uncertainty of 15% resulted in a minimum detection limit of ~4 particles cm^{-3}, below which data were discarded. Equation (3.2) was then fit to a spectra of activated ratios at a number of supersaturations (e.g., Figure 3.3) to determine E, C, and s^* for each particle size during a supersaturation cycle. Resulting fits were then filtered to assure reasonable fit values with the criteria that $0.2<E<1.2$ and $-15<C<-2$; values of $C>-2$ no longer provide a physically realistic sigmoid (Appendix A) and values of $C<-15$ are limited by instrument resolution (Lance, 2007; Appendix A). χ^2 values, a measure of the goodness of the fit, are obtained, and the highest 5% are filtered to remove the outliers. Using these filter criteria, the percentage of discarded fits for 40, 60, and 80 nm data are ~14%, 10%, and 16%, respectively.

$R_a(s)$ represents a cumulative distribution of critical supersaturation for particles with dry diameter d_p. Assuming that this variability is driven solely by variance in chemical composition, we can transform $R_a(s)$ into a cumulative distribution of hygroscopicity, $R_a(\kappa)$, using the definition of κ (if κ>0.1),

$$\kappa = \frac{4A^3}{27 d_p^3 s^2} \tag{3.3}$$

where d_p is the dry diameter of the particle (Petters and Kreidenweis, 2007).

For every s^* there is a corresponding characteristic hygroscopicity parameter, κ^*, so that (s/s^*) can be expressed as $(\kappa/\kappa^*)^{-1/2}$. From this and Equation (3.2), the complement of $R_a(s)$ can be written as

$$R_a(\kappa) = E - \frac{E}{1+\left(\frac{\kappa}{\kappa^*}\right)^{-\frac{C}{2}}} = \frac{E}{1+\left(\frac{\kappa}{\kappa^*}\right)^{\frac{C}{2}}} \tag{3.4}$$

The probability distribution function (PDF) for κ, $p^s(\kappa)$ can be found by differentiating Equation (3.4) with respect to κ and normalizing over the integral of possible κ values.

$$p^s(\kappa) = \frac{1}{E}\frac{dR_a(\kappa)}{d\kappa} = -\frac{\frac{C}{\kappa^* 2}\left(\frac{\kappa}{\kappa^*}\right)^{\frac{C}{2}-1}}{\left(1+\left(\frac{\kappa}{\kappa^*}\right)^{\frac{C}{2}}\right)^2} \tag{3.5}$$

Analysis of $p^s(\kappa)$ can provide the chemical dispersion, which describes the degree of chemical heterogeneity of the CCN population. As described in Lance (2007), the chemical dispersion, $\sigma(\kappa)$, of particles of size d_p can be found by computing the square root of variance about κ^* (assuming a Gaussian distribution where the average κ is equal to κ^*)

$$\sigma^2(\kappa) = \frac{\int_0^\infty (\kappa-\kappa^*)^2\, p^s(\kappa) d\kappa}{\int_0^1 p^s(\kappa) d\kappa} \tag{3.6}$$

so that the chemical heterogeneity of the CCN population can be approximated by $\kappa^{*}\pm\sigma(\kappa)$. Thus, the chemical dispersion is described by the spread in the distribution of measured κ values, illustrating the degree of heterogeneity in particle chemistry. Further explanation of this method, including a discussion on the chosen integration limits of 0 to 1 used in Equation (3.6) and the contribution of instrument operation on $\sigma(\kappa)$ are discussed in Appendix A.

3.4 RESULTS

Temporal variation of HTDMA-derived and CFSTGC-derived κ values, total particle concentration, and AMS mass concentrations throughout the campaign are shown in Figure 3.4. Error bars (see Appendix A) are not shown, because these are usually small and difficult to discern in the figure. Average uncertainties for κ values are 0.009, 0.012, and 0.021 for 40, 60, and 80 nm particles, respectively. CN concentrations are typically below 200 particles cm^{-3} for 40, 60, and 80 nm particles, and AMS total mass ranges from 0 to 10 $\mu g\ m^{-3}$. While during some periods these quantities show similar trends (e.g., 4/9/2007 to 4/11/2207 and 5/1/2007 to 5/11/2007), correlation of these parameters with κ variability is weak. The trend in κ values derived from HTDMA and CFSTGC measurements correlate well (as discussed in the following). General trends of κ values for different size particles are very similar, although specific differences between sizes will be presented in the following analysis. Average CFSTGC-derived κ values for 40, 60, and 80 nm particles are 0.20±0.06, 0.19±0.06, and 0.22±0.06, respectively, while average HTDMA-derived κ values for 30 and 50 nm particles are 0.15±0.06 and 0.14±0.05, respectively. As aerosol aqueous-phase solutions in the HTDMA are more concentrated than those in the CFSTGC and calculations of κ may be more greatly

impacted by solution non-ideality, phase separation, and partial solubility of constituents, it is not surprising that HTDMA-derived κ averages are generally lower. Also, the CCN counter detects only those particles that are activated (as indicated by the E parameter) which means that non-hygroscopic particles do not impact the slope of the sigmoid used to calculate s^*. When the HTDMA detects non-hygroscopic particles, it results in a GF=1 which invariably decreases the inferred value of κ. However, as E is almost always >0.9, the contribution of non-hygroscopic particles to the HTDMA-derived κ is small. A likely reason for the differences seen is that a larger fraction of the commonly less soluble organic material is dissolved in the dilute droplets present in the CFSTGC. HTDMA-derived κ values from this study are in agreement with the HTDMA-derived average κ=0.18 for 35, 50, 75, and 110 nm particles reported for this region by Sihto et al. (2010) for July 2008 to June 2009. The slight discrepancy between our results and those reported by Sihto et al. (2010) may result from the fact that particle hygroscopicity in this region is dependent on particle size (e.g., Birmili et al., 2009) and larger particles typically show increased hygroscopicity (also shown by the higher average CFSTGC-derived κ for 80 nm particles compared to that of 60 and 40 nm particles discussed in Section 4.2).

Comparison of κ values from 60 nm CCN data against 50 nm HTDMA data for the entire campaign is presented in Figure 3.5. The higher magnitude of CFSTGC-derived over HTDMA-derived κ values is again seen in this comparison with most of the values consistent within ±30 %. As discussed above, these differences are well within the range of possible uncertainties often seen between HTDMA and CFSTGC-derived κ values (e.g., Petters and Kreidenweis, 2007; Prenni et al., 2007, 2009; Massoli et al., 2010).

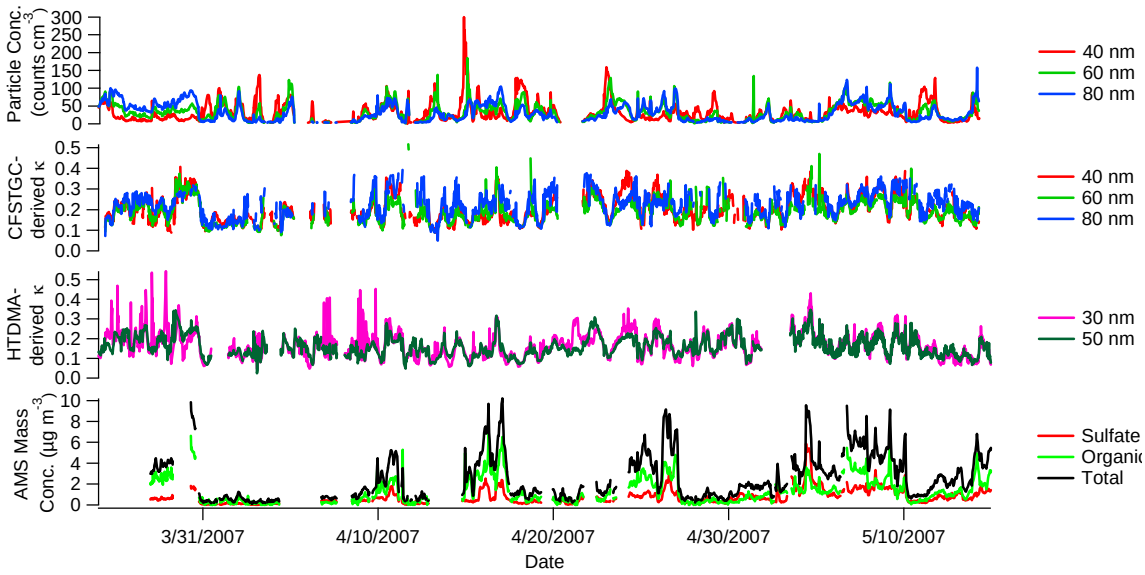

Figure 3.4: Temporal variation of HTDMA-derived and CCN-derived κ values, total particle concentration, and AMS mass concentration throughout the campaign.

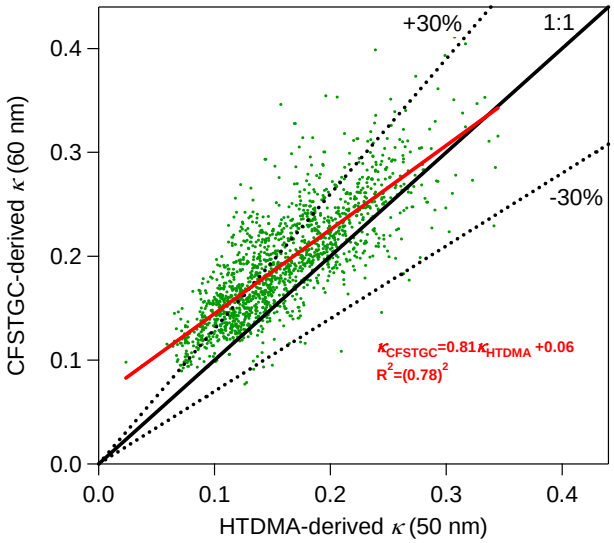

Figure 3.5: CFSTGC-derived κ values for 60 nm diameter particles against HTDMA-derived κ values for 50 nm diameter particles. Shown is a best fit line (red), 1:1 line (black, solid), and lines of ±30% deviation (black, dotted).

3.4.1 Diurnal Variability of CCN Properties

Diurnal variation in CCN maximum activated fraction (E) and characteristic critical supersaturation (s^*) are shown for 40, 60, and 80 nm particles (Figures 3.6a and 3.6b).

The error bars represent day-to-day variations, which are greater than the average fitting uncertainties (see Appendix A). For exam example, the average fitting uncertainties for the maximum activated fraction are 0.04, 0.02, and 0.02 for 40, 60, and 80 nm particles, respectively, and those for the characteristic critical supersaturation are all 0.02%. While the 60 and 80 nm particles show rather constant values of E, 40 nm data seem to display a decrease in E the from late morning through evening (Figure 3.6a). This daytime decrease in maximum activated fraction, however, is the result of not reaching the asymptote for 40 nm spectra at the highest supersaturation measured (s_{max}). If calculations are repeated using $R_a(s_{max})$ instead of the asymptote $E=R_a(\infty)$, this diurnal cycle is no longer apparent. Thus, it is expected that the true diurnal variation of E for 40 nm particles is analogous to that of the 60 and 80 nm particles. Not reaching the asymptote, however, has negligible effects, if any, on the C and s^* fit parameters. As expected, 40 nm particles have the highest characteristic critical supersaturations of the particle sizes sampled in this study and reach their critical supersaturation well below the highest instrument supersaturation (~1.8%) (Figure 3.6b). Diurnal trends in total particle concentration, corrected to account for dilution air added to the sample flow, are similar for all measured sizes (Figure 3.6c).

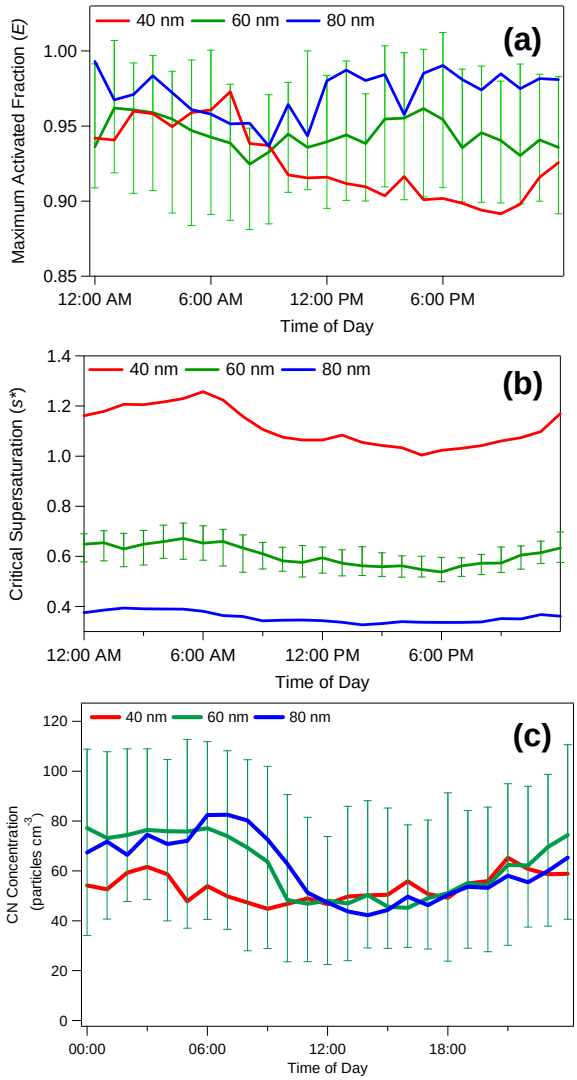

Figure 3.6: Diurnal variation of the (a) CCN maximum activated fraction, (b) critical supersaturation, and (c) CN concentration for 40, 60, and 80 nm particles. Solid lines represent median values. Bars representing the 25th and 75th percentile values are shown for 60 nm data.

3.4.2 Diurnal Variability of κ

Diurnal trends in CFSTGC-derived and HTDMA-derived κ values are seen for all particle sizes sampled with minimum κ values occurring in the early morning (near sunrise) and maximum κ values occurring in the afternoon (Figures 3.7a and 3.7c). This diurnal trend corresponds well with those found by previous studies at the Hyytiälä site

(e.g., Hämeri et al., 2001; Väkevä et al., 2002; Boy et al., 2004; Ehn et al., 2007). CFSTGC-derived κ values covary with AMS-derived inorganic volume fraction, daily temperature trends, and AMS f_{44} data. As f_{44} increases linearly with *O/C* ratio (Aiken et al., 2008) and organics in the atmosphere typically become more oxidized as they age; this suggests that aerosol hygroscopicity is also determined by the aging of those organics. This is consistent with the view of oxidation state correlating with hygroscopicity presented by Jimenez et al. (2009) and Massoli et al. (2010).

As reported by Boy et al. (2004), GF (related to κ by Equation (3.1)) is more variable during the daytime than the early morning period. This is also observed in our study as there is typically a clear peak in normalized κ frequency in the early morning while there is a wide spread of κ values with no clear peak in the afternoon (Figure 3.7b). The clear size-dependence shown by Boy et al. (2004) is also seen in our diurnal κ trend, as larger particles display larger κ values than the smaller particles (Figure 3.7c). Our observations confirm the different hygroscopic modes reported by Hämeri et al. (2001) where Aitken mode particles (35, 50, and 73 nm) show distinctly different hygroscopic behavior than the larger accumulation mode particles (about 80 nm or larger).

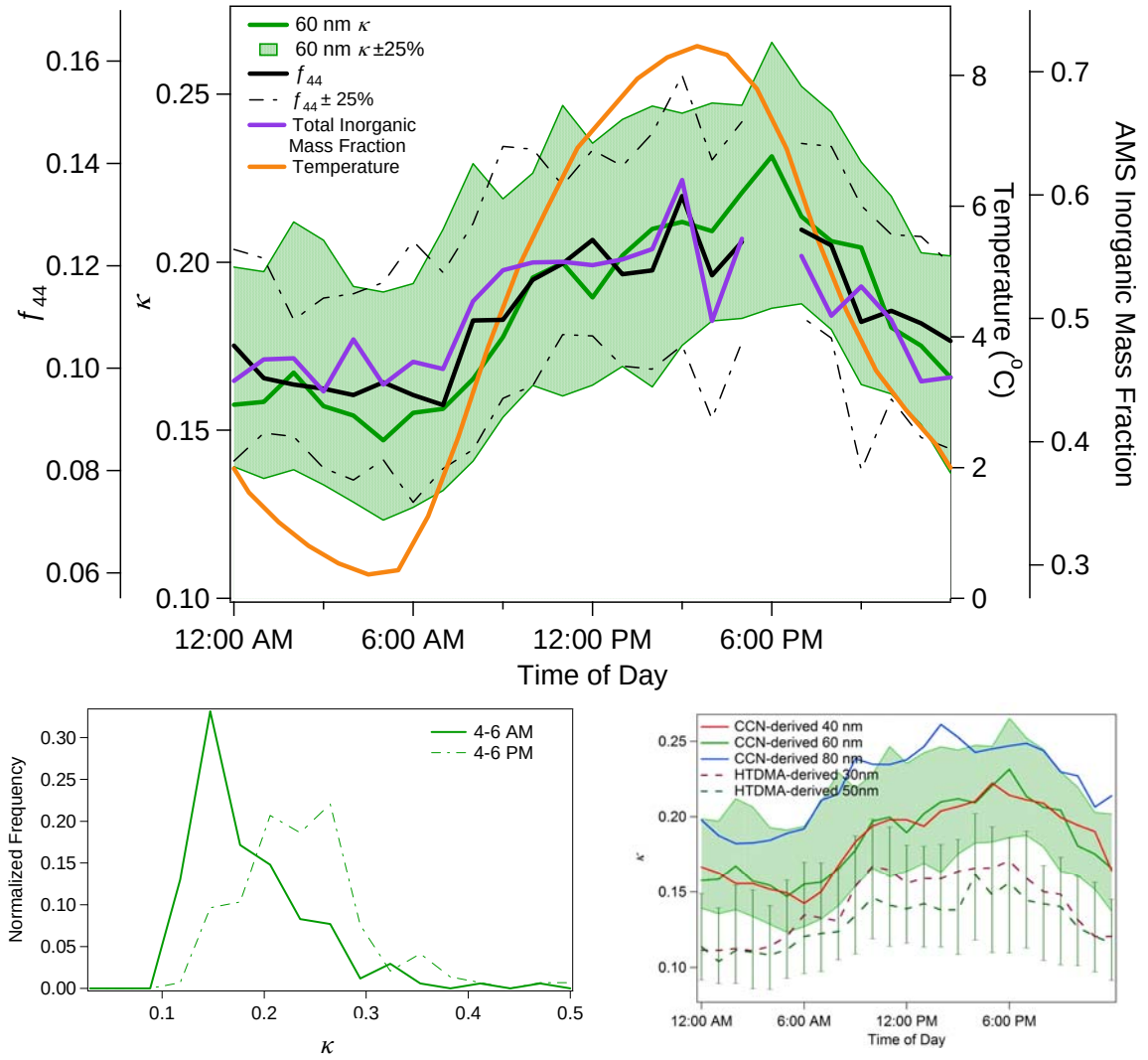

Figure 3.7: (a) Diurnal trend of 60 nm CFSTGC-derived median κ (green line) with 25th and 75th percentiles shaded in green. Also shown are average temperature (orange line), median f_{44} given by AMS (black line) with 25th and 75th percentiles shown by dotted black lines, and median inorganic mass fraction (purple line). (b) Frequency distributions of 60 nm CFSTGC-derived κ values for times of minimum (solid line) and maximum (dotted line) κ values. (c) Diurnal CFSTGC-derived κ distributions for 40, 60, and 80 nm particles and HTDMA-derived distributions for 30 and 50 nm particles. Bars representing the 25th and 75th percentile values are shown for 60 nm and 50 nm data.

The chemical dispersion, $\sigma(\kappa)$, describing the degree of heterogeneity in particle chemistry, for 40, 60, and 80 nm particles is shown in Figure 3.8. 60 and 80 nm particles show a potential diurnal trend in chemical dispersion, similar to that of diurnal κ. Chemical dispersion of 40 nm particles, however, remains rather steady and does not show the same increase just before noon as observed for the other sizes. The composition of nucleation and Aitken mode particles are influenced by nucleation events (Hämeri et al., 2001); it is therefore possible that 40 nm particles do not experience the afternoon increased chemical dispersion since new particle formation events often occur around noon (Nieminen et al., 2009). This means that while the chemical dispersion of larger particles changes, these 40 nm particles still reflect the composition of newly formed particles originating in the boreal forest. As 60 nm particles exhibit a similar diurnal κ trend (Figure 3.7c), one might initially expect similar chemical dispersion. However, 60 nm particles (and larger) would have had more time to be affected by SOA condensation, coagulation, and long range transport; thus, they may exhibit a larger degree of chemical heterogeneity than 40 nm particles.

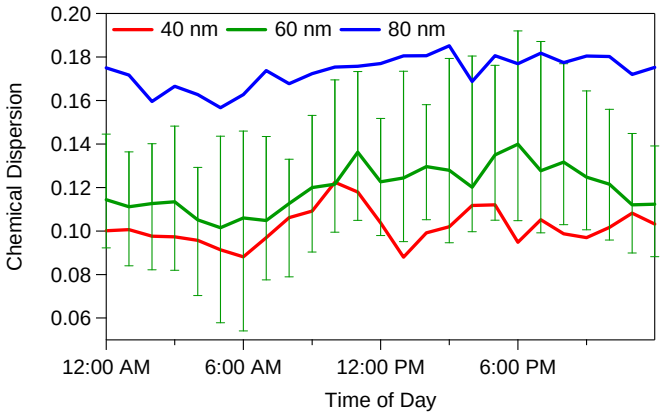

Figure 3.8: Diurnal variation of $\sigma(\kappa)$ for 40, 60, and 80 nm particles.

This is in agreement with Petäjä et al. (2005) who showed remarkable variability in the Aitken mode hygroscopicity which was linked to air mass transport and indirectly possibly to aging while, on the other hand, showed that the nucleation mode hygroscopicity was quite constant due to relatively homogeneous surroundings. This is also consistent with Hämeri et al. (2001) whom also saw that external mixing increases with increasing particle size in Hyytiälä.

Current values of relative chemical dispersion are similar to those from a megacity environment (Su et al., 2011). The magnitude of chemical dispersion depends somewhat on hygroscopicity, so relative values, $\sigma(\kappa)/\kappa$, are used for comparison. Further details regarding the comparison are given in Appendix A, and the chemical dispersion values are given in Table A.2. Based on the average $\sigma(\kappa)$ and κ, current relative chemical dispersion values for the 40, 60, and 80 nm dry size are 0.55, 0.63, and 0.77, respectively, and those from Su et al. (2011) for 39, 55, and 75 nm dry size are 0.60, 0.50, and 0.54, respectively. Deviations are seen at larger particle sizes, but considering the uncertainties related to the interpretation of chemical variability (e.g., DMA transfer function effects, etc. as described in Appendix A and Lance et al., 2007) firm conclusions cannot be made.

3.4.3 On κ Closure with AMS Data

κ, which represents the overall aerosol hygroscopicity, is the sum of contributions from each aerosol constituent

$$\kappa = \sum_j \kappa_j \varepsilon_j \tag{3.7}$$

where ε_j and κ_j are the volume fraction and hygroscopicity parameter, respectively, of aerosol component j (Petters and Kreidenweis, 2007). Based on AMS data, the components can include organic and inorganic salts calculated from the measured ion

concentrations (e.g., Raatikainen et al., 2010). When there are no significant variations in the composition of the organic and inorganic fractions (as seems to be the case in this data set) only the inorganic and organic fraction are needed for a reasonably good prediction

$$\kappa = \varepsilon_i \kappa_i + \varepsilon_o \kappa_o \quad (3.8)$$

where ε_i and ε_o, and κ_i and κ_o, are the volume fraction and hygroscopicity parameters of inorganics and organics, respectively. Fits were also tested for a three component model that includes inorganic ions as one group as well as the more and less oxidized organic groups. This model was shown to be superior during a previous campaign in 2005 (Raatikainen et al., 2010), but in the current campaign the average organic mass fractions are lower and there are much less variations in organic oxidation state. As a result, predictions for the three component approach provided similar results to the two component model, which will be used in this study. The relevant inorganic ions detected by the AMS include ammonium, nitrate, and sulfate. In order to find volume fraction, their mass concentrations were combined and, as ammonium sulfate dominated the inorganic mass, the density of ammonium sulfate, 1.77 g cm^{-3}, was assumed (Lance et al., 2009). Organic volume was calculated using a density of 1.4 g cm^{-3} and measured mass concentrations (Lance et al., 2009). 60 nm CFSTGC-derived κ values and a linear fit based on the 50 nm HTDMA-derived κ values as a function of AMS measured organic volume fraction are shown in Figure 3.9. Typical expected κ values for a pure inorganic compound (i.e., ammonium sulfate) as well as pure SOA are shown by the sulfate-SOA mixing line.

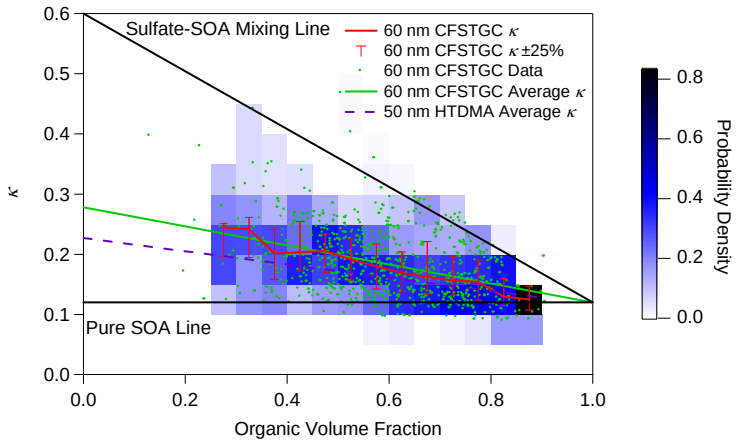

Figure 3.9: 60 nm CFSTGC-derived κ median values (red line) with bars showing 25th and 75th percentiles. Actual 60 nm CFSTGC-derived κ values shown by green circles. Probability density for 60 nm data is indicated by the blue shading. The black dashed line indicates the sulfate-SOA mixing line. The solid green line shows the average value of 60 nm CFSTGC-derived κ as predicted by AMS closure while the dashed purple line shows the 50 nm HTDMA-derived κ as predicted by AMS closure.

Fitted κ_i and κ_o for 40, 60, and 80 nm particles are shown in Table 1. The higher magnitude of both of these values for 80 nm data is expected as the general magnitude of hygroscopicity is greater for this size than for 40 and 60 nm particles (Figure 3.7c). Still, while these values correspond well with the κ_o value of 0.1 used in Sihto et al. (2010) and proposed by Gunthe et al. (2009), κ_i values are too low for typical inorganic compounds as the hygroscopicity of ammonium sulfate is ~0.6 (Petters and Kreidenweis, 2007). Bulk mass concentrations measured by the AMS during the campaign were dominated by particles with volume diameter typically ranging from about 300–400 nm (mean volume diameter ~380 nm), much greater than those sampled by the CFSTGC. Since large particles have been shown to differ in hygroscopicity and chemical dispersion from smaller particles and the organic mass fraction in Aitken particles has been shown to be significantly higher than in larger particles (Allan et al., 2006), bulk composition measurements (in this case from AMS) may overestimate the inorganic mass fraction

used to describe the 40, 60, and 80 nm particles in this study. These results illustrate that bulk composition measurements should be used with caution as they may sometimes be inadequate when applied to the study of particles of CCN-relevant sizes.

Table 3.1. κ_o and κ_i values for 40, 60, and 80 nm particles.

Particle Size (nm)	κ_o	κ_i
40	0.12	0.30
60	0.12	0.30
80	0.14	0.35

3.4.4 CCN Activation Kinetics

The droplet diameter of a given particle exposed to a constant supersaturation in the CFSTGC is described by (Lance et al., 2006; Lathem and Nenes, 2011),

$$D_p{}^2 = D_o{}^{*2} + 2G \int_{t_{act}}^{t_{out}} s dt \tag{3.9}$$

where D_p is the droplet diameter exiting the CFSTGC, $D_o{}^*$ is the diameter of the CCN when exposed to its critical supersaturation, s_c, t_{act} is the time (after entrance in the growth chamber) when the supersaturation in the instrument becomes equal to s_c, and, t_{out} is the time when droplets exit the growth column. G is a coefficient that encompasses mass and heat transfer properties of the particle (Roberts and Nenes, 2005; Lance et al., 2006). From Equation (3.9), D_p tends to increase with increasing s. This is shown by the range of 80 nm particle D_p throughout the study in Figure 3.10a, where D_p is color-coded by instrument s. The second term in Equation (3.9) dominates over the first term for particles of low s_c, so that the droplet size at the exit of the instrument is insensitive to its s_c. This effect is shown in Figure 3.10b for all size-selected particle sizes, each with a respective s^*, where D_p become increasing similar at the highest s values. This also means that droplet size distributions narrow at increasing supersaturation (as illustrated by the

vertical error bars in Figure 3.10b and the narrowed droplet size distribution at high s values in Figure 3.10b). However, the asymptotic size reached by the particles at high s (Figure 3.10b) is a result of the compensating effects between a higher s and a larger entry length required for its development (i.e., t_{act} approaches tout as instrument s increases; Lance et al., 2006).

Threshold Droplet Growth Analysis (TDGA) is a method used to investigate shifts in droplet growth kinetics for ambient (Bougiatioti et al, 2009, 2011; Lance et al., 2009; Padró et al., 2010) and laboratory (Engelhart et al., 2008; Asa-Awuku et al., 2009, 2010, 2011) aerosol. The average droplet diameter of particles exiting the CFSTGC is measured and compared to droplet size from calibration aerosol (typically ammonium sulfate or sodium chloride) with s_c equal to the instrument supersaturation. Calibration aerosol represents an upper limit of rapid activation kinetics, as the material is deliquesced before it activates and the water vapor accommodation coefficient is large. Therefore, if ambient aerosol experience rapid activation kinetics, the droplet sizes of ambient and calibration particles should be similar. Provisions should be taken to avoid high CCN concentrations in the instrument that would deplete s and affect D_p, with implications on droplet size (Lathem and Nenes, 2011).

The calibration of the CFSTGC in this study was carried out with SMCA (Moore et al., 2010). In addition to a highly accurate calibration curve, the method also provides D_p for a wide range of particle sizes and s^*. Figure 3.10c shows D_p for 40, 60, and 80 nm particles at $s=s^*$ and lines based on average D_p of calibration aerosol. As the instrument did not sample particles directly at their s^* but rather for set steps on instrument supersaturation, the two supersaturation values and wet diameters closest to s^* were used

in interpolating the droplet diameter at s^*. Average droplet sizes from ambient aerosol grow to sizes comparable to calibration aerosol. This means that the organics present at Hyytiälä are not associated (on average) with retarded activation kinetics. A small fraction (<10% of the total CCN) did exhibit significantly smaller droplet sizes than the calibration aerosol.

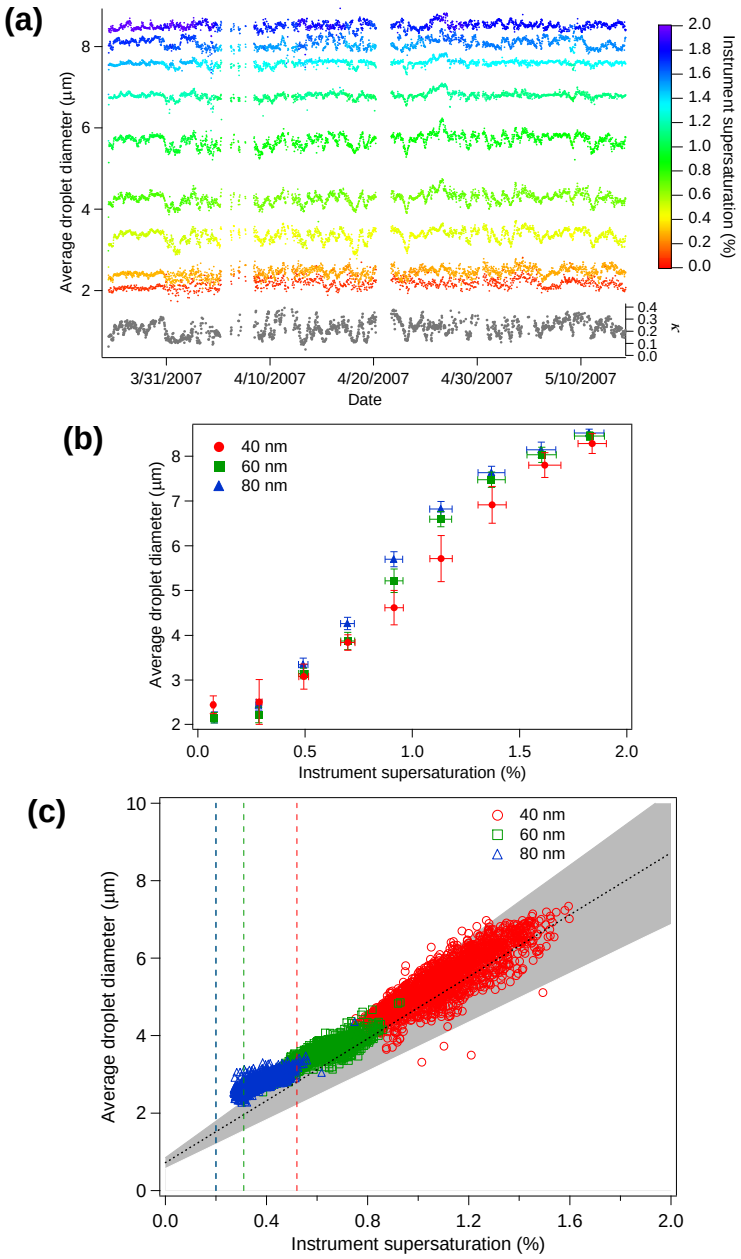

Figure 3.10: (a) Temporal variation of droplet size for ambient 80 nm particles color-coded by instrument supersaturation. κ values are shown in grey (right-hand scale). (b) Average droplet diameters for 40 (red circles), 60 (green squares), and 80 nm (blue triangles). Vertical and horizontal error bars represent the standard deviation of measured droplet sizes and supersaturation, respectively. (c) Activated droplet sizes for 40 (red circles), 60 (green squares), and 80 nm (blue triangles) ambient particles measured at supersaturations closest to the critical supersaturation of ammonium sulfate particles of the same respective size. The calibration curve is shown by a black dotted line while the grey area indicates the sizing uncertainty for the ammonium sulfate particles. Critical supersaturations for 40, 60, and 80 nm ammonium sulfate particles are given by red, green, and blue dashed lines, respectively. Inset are histograms for each size particle indicating the occurrence of ratios of ambient wet droplet size to calibration wet droplet size.

3.5 CONCLUSIONS

The size-resolved hygroscopicity and activation kinetics were investigated for particles sampled at the SMEAR II boreal forest station in Hyytiälä, Finland, from March to May 2007. CCN maximum activated fraction show similar values for 60 and 80 nm aerosol and remain close to unity. Although results of maximum activated fraction of 40 nm particles were impacted by the range of supersaturations measured in this study, these particles are expected to show variation similar to that of 60 and 80 nm particles.

Overall, κ values are mainly found between 0.10 and 0.40 for all sizes with an average of 0.20±0.06, 0.19±0.06, and 0.22±0.06 for 40, 60, and 80 nm particles, respectively. These low values reflect the dominant role of organics on CCN activity. The diurnal trend of κ with inorganic volume fraction and f_{44} suggests that κ variability may be partly explained by the diurnal variability of organics in the atmosphere and particle aging. This suggests that the trend in organic composition and oxidation state of both small CCN-relevant size particles and larger particles sampled in bulk measurements is the same and also that more aged (oxidized) particles have higher hygroscopicities than less oxidized organics.

The diurnal trend in κ displays maximum values in the afternoon and minimum values in the early morning as has been seen in previous studies by Hämeri et al. (2001), Väkevä et al. (2002), Boy et al. (2004), and Ehn et al. (2007). The high variability of afternoon κ values and the general increase in κ observed for larger particles confirm the results of these earlier studies. 60 and 80 nm particles show a slight diurnal trend in chemical dispersion while 40 nm dispersion remains rather stable. This could be

representative of the effect of new particle formation on the chemical composition of 40 nm particles and also the effect of increased external mixing with size.

Hygroscopicities of the aerosol organic and inorganic fractions were predicted from bulk composition (using an AMS) and CCN-derived aerosol hygroscopicity. Hygroscopicity of the inorganic fraction was considerably lower than expected, which indicates that bulk measurements should be used with caution for representing characteristics of small mode particles. Due to the high number of nucleation events at the SMEAR II station, the composition of small particles (which contribute significantly to CCN concentrations) differs from that of large particles (which are more closely represented by measurements of bulk composition).

Analysis of droplet growth kinetics shows that ambient particles activate and grow as rapidly as calibration aerosol, adding to an emerging body of evidence that highly oxidized organics (even if they constitute the majority of the aerosol volume) do not inhibit the rate of water accommodation. If this is representative of other locations and seasons, it will substantially simplify the description of CCN activation kinetics in atmospheric models of aerosol-cloud-climate interactions.

CHAPTER 4

TOWARDS THE DETERMINATION OF JOINT VOLATILITY-HYGROSCOPICITY DISTRIBUTIONS: DEVELOPMENT AND RESPONSE CHARACTERIZATION FOR SINGLE-COMPONENT AEROSOL[1]

4.1 INTRODUCTION

Organic aerosol (OA) constitutes a large fraction of the atmospheric aerosol burden, with global production estimates ranging from 50 to 100 Tg yr^{-1} (e.g., Pye and Seinfeld, 2010; Hallquist et al., 2009; Jimenez et al., 2009; Kanakidou et al., 2005). Secondary organic aerosol (SOA) is the result of gas-to-particle conversion of oxidized gas-phase precursors and constitutes a large fraction of OA. Understanding the gas-particle partitioning of atmospheric aerosol is necessary for effective OA modeling and prediction of the aerosol budget (e.g., Donahue et al., 2009). Furthermore, understanding the contribution of SOA to aerosol number and hygroscopicity is important for prediction of cloud condensation nuclei (CCN) (e.g., Gantt et al., 2012; Riipinen et al., 2011; Lambe et al., 2011; Engelhart et al., 2011; Chang et al., 2010; Massoli et al., 2010; Asa-Awuku et al., 2009; Roelofs, 2008; Kanakidou et al., 2005).

The volatility of SOA has been a subject of intense study for years in both chamber and environmental field studies. For example, Cappa and Jimenez (2010) found that a large portion of the ambient OA mass in Mexico City was non-volatile, while Lee et al. (2010) discovered that most OA in a remote region near Finokalia in Crete, Greece, was semi-volatile. In chamber studies, Salo et al. (2011) found that aerosol ageing took place

[1]This chapter published as: Cerully, K. M., Hite, Jr., J. R. Jr., McLaughlin, M., and Nenes, A.: Towards the determination of joint volatility-hygroscopicity distributions: Development and response characterization for single-component aerosol, Aeros. Sci. Tech., 48, 295-311, doi: 10.1080/02786826.2013.870326, 2014.

in the gas phase due to OH oxidation of semi-volatile organic compounds (SVOCs) and intermediate-volatility organic compounds (IVOCs) rather than by bulk or surface reactions. Furthermore, the effects of particle volatility on CCN number and activity have also been investigated. Riipinen et al. (2011) showed that neglecting ultrafine aerosol growth by organic condensation can result in large underpredictions of CCN concentrations. Asa-Awuku et al. (2009) showed that volatilization of organic aerosol in CCN chambers can bias observed CCN activity, hence raising the need for considering volatility effects in these measurements. These studies all involved the use of a thermodenuder, a heated laminar flow reactor that volatilizes particles and is typically followed by a cooling section containing adsorbing materials that prohibit re-condensation of volatilized vapors onto the aerosol. These measurements help constrain the volatility distributions of organic aerosol (Donahue et al., 2006) for a quantitative description of semi-volatile aerosol partitioning.

Several thermodenuder designs have been presented and analyzed in the literature (Faulhaber et al., 2009; Huffman et al., 2008; Fierz et al., 2007; An et al. 2007; Wehner et al., 2002; Burtscher et al. 2001). Design parameters involve the residence time in the heating section (e.g., Saleh et al., 2011; Fierz et al., 2007; An et al., 2007), the temperature profile in the heating section (e.g., Faulhaber et al., 2009; Huffman et al., 2008), the effectiveness of the cooling section (e.g., Fuentes and McFiggans, 2012; Saleh et al., 2011; Fierz et al., 2007), and the modeling approach used to interpret the data (e.g., Saleh et al., 2011; Cappa et al., 2010; Riipenen et al., 2010; Saleh and Shihadeh, 2007). Generally, the thermodenuder geometry and instrument flow rate are selected to give a desired residence time in the heating section of the thermodenuder. Attention has also

been given to characterizing temperature profiles that develop in the heating section through, for example, the use of sand as insulating material (Wehner et al., 2002) and multiple heating zones (e.g., Faulhaber et al., 2009; Huffman et al., 2008). Studies by Saleh et al. (2011) and Fuentes and McFiggans (2012) have investigated the level of importance of the cooling section and the influence of mass loading on the re-condensation fraction of volatilized material.

Models have been developed to interpret thermodenuder data and usually invoke assumptions and approximations regarding the temperature and flow profiles in the heating section. Together with the aerosol concentration flowing through the instrument and the degree to which gas-particle equilibrium is satisfied in the thermodenuder influences how approximations affect the inferred volatility distributions. Cappa et al. (2010) and Lee et al. (2010) approximate the thermodenuder temperature with a piecewise profile with constant radial temperature based on the experimental temperature profile of Huffman et al. (2008). Riipinen et al. (2010) assume a constant temperature throughout the thermodenuder. Both studies assume a developed parabolic velocity profile for laminar flow from the entrance of the thermodenuder. Fuentes and McFiggans (2012) use a plug flow approximation, though Cappa et al. (2010) shows that this leads to an overestimation of vapor pressure and underestimation of the enthalpy of vaporization as compared to assuming a parabolic radial velocity. The above suggests that simplifications in temperature, concentration and flow profiles may under certain conditions introduce important uncertainties in inferred vapor pressure. A need therefore remains for an operational model that fully resolves pressure, temperature, concentration

and velocity flow fields within the thermodenuder, alongside a comprehensive treatment of volatilization kinetics with minimal simplifications.

Here we present a newly-developed thermodenuder system with a fully coupled simulation model framework. The thermodenuder is carefully designed to provide as stable and constant temperature profiles as possible. Size-resolved aerosol are used to characterize instrument response function (i.e., the change in aerosol size at several thermodenuder temperature set points). The instrument model is formulated to consider the temperature, volatilized vapor, flow variations and the size distribution of the volatilized aerosol at every point in the instrument. The model is then embedded within an optimization framework to determine optimal estimates of vapor pressures and enthalpy of phase change from volatility data. Thermodenuder measurements are combined with a Continuous-Flow Streamwise Thermal Gradient CCN Counter (CFSTGC) to provide a composition proxy for interpreting the instrument response function and help deconvolute the influence of particle impurities on instrument response.

4.2 INSTRUMENTATION

4.2.1 Thermodenuder Design

A thermodenuder was constructed based on the original design of Wehner et al. (2002) and modifications of Huffman et al. (2008) (Figure 4.1). The instrument consists of a heating section, which allows semi-volatile components in the aerosol to volatilize, followed by a cooling section where the volatilized gas components are adsorbed onto activated carbon before exiting the instrument. The heating section consists of a stainless steel tube (0.68 inch ID, 0.75 inch OD) wrapped with 3 sections of heating tape (HTS/Amptek). The section is further wrapped with 1 inch high-temperature fiberglass

insulation to prevent heat loss from the tube. Flow continues through the cooling section, a wire mesh tube (0.75 inch ID) surrounded by activated carbon (Calgon Carbon Corporation, AP4-60) and enclosed by a large stainless steel pipe, allowing volatilized components to pass through the mesh and adsorb onto the carbon. At either end of the casing are two stainless steel discs which are held together by threaded screws and sealed using a silicon O-ring (3.25 inch ID, 3.75 inch OD). The heating and cooling section are connected by a short section of Swagelok unions. Thermodenuder geometry allows for centerline residence times in the heating section of 35.7, 17.9, and 10.7 s for flow rates of 0.3, 0.6, and 1 L min^{-1}, respectively.

Temperature within the heating section is measured at the outer surface of the stainless steel tube using three thermistors (Panasonic, type NTC). The first thermistor is placed at the end of the first heating tape section; the other two thermistors are placed at the center of the second and third heating tape sections, respectively. Centerline temperatures were measured by disconnecting the cooling section and inserting a thin steel rod with a point thermocouple protruding 1 inch from the end of the rod at different points throughout the centerline of the heating tube. This method was also used to measure the inner wall temperature across the tube and is used as a boundary condition for the instrument model. A fourth thermistor is placed before the entrance of the thermodenuder to record the entering flow temperature. All thermistors are tightly fastened onto the tube using polyimide Kapton® tape (maximum temperature rating of 200°C).

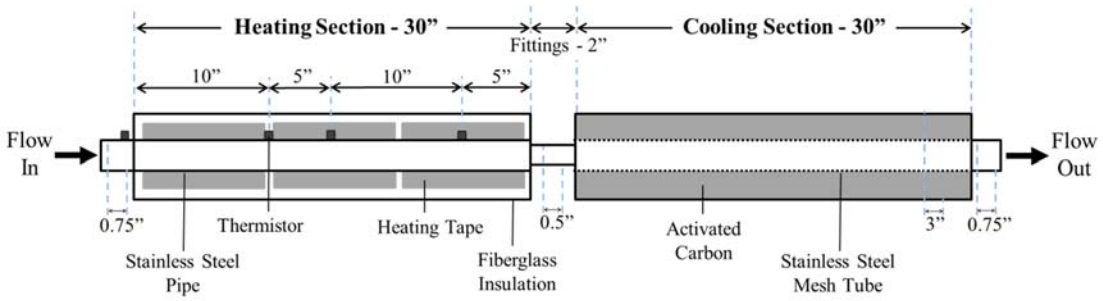

Figure 4.1: Cross-sectional schematic of the thermodenuder constructed and used for this study

Feedback control is used to maintain the temperature profile in the heating section. The three thermistors along the heating tube wall are connected to a data acquisition device (LabJack, model U12) in conjunction with an electronic A/D converter and a LabVIEW program developed for this purpose. This system controls each heating tape section by comparing thermistor outputs to a desired set point temperature (usually within 0.5°C) and continuously records all desired parameters throughout the entirety of the experiment. The duration and frequency of current sent to the electrical heating tape can be varied to change the speed of heating and minimize set point overshoot. To prevent a fire hazard from uncontrolled overheating (e.g., due to a LabVIEW or computer failure), thermal fuses rated for 125°C were installed in line with each heating tape power supply.

4.2.2 Thermodenuder Characterization

Set point temperatures and resulting centerline temperatures in the heating section confirm reliable and well-controlled behavior (Figure 4.2a). The measured profiles reach the set points with less overshoot than in existing thermodenuder designs (e.g., Wehner et al., 2002; Huffman et al., 2008; Faulhaber et al., 2009). This overshoot was mainly avoided by moving the thermistor to the end rather than the center of the first heating tape

section as the impact of entrance effects is accompanied by a lower wall temperature than in the developed region.

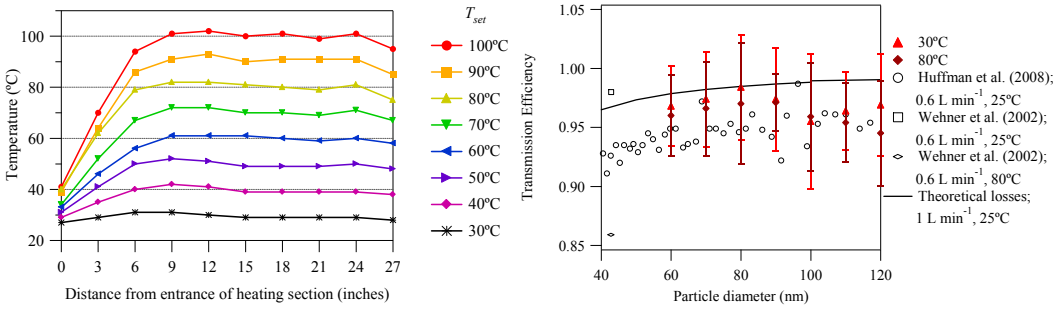

Figure 4.2: (a) Thermodenuder centerline temperature profiles at unique temperature set points (T_{set}) and a flow rate of 1 L min^{-1}. Offline thermal probe measurement precision is 0.5°C. (b) Particle transmission efficiency through the thermodenuder compared to previously published values. Measurements correspond to 1 L min^{-1} flow through the instrument. The solid black line represents theoretical losses from Brownian diffusion.

Particle transmission efficiency, a measure of the particles that are lost in the instrument mainly from Brownian diffusion and thermophoresis in the cooling section (Orsini et al., 1998; Wehner et al., 2002; Huffman et al., 2008), was measured using ammonium sulfate aerosol, which is nonvolatile at up to as low as 75°C (Clarke, 1991; Burtscher et al., 2001; An et al., 2007). As diffusional and thermophoretic effects are dependent on particle size, aerosol were size-selected using a differential mobility analyzer (DMA; Model 3081, TSI) then split to a concentration particle counter (CPC; Model 3010, TSI) and the thermodenuder. An additional CPC (Model 3010, TSI) located downstream of the thermodenuder measured the exiting particle concentration. Figure 4.2b shows particle transmission efficiency for particles ranging from 50 to 100 nm incurred at 30°C and 80°C in the thermodenuder. Measurements conducted at a flow rate of 1 L min^{-1} range between the predicted diffusional losses (at 30°C) determined for a cylindrical tube (Hinds, 2009) at 1 L min^{-1} and results from both Huffman et al. (2008)

and Wehner et al. (2002) measured at 0.6 L min^{-1}. This meets expectations and ensures that there are no unanticipated particle losses from secondary flows or non-uniform temperature distributions in the instrument.

4.3 METHODOLOGY

4.3.1 Experimental Setup

CCN activity and hygroscopicity of denuded and non-denuded aerosol are obtained using a DMT CFSTGC (Figure 4.3) (Roberts and Nenes, 2005; Lance et al., 2006). Particles with a critical supersaturation less than the water vapor supersaturation, *s*, in the CFSTGC will activate into cloud droplets and be counted as CCN. We use the Scanning Flow CCN Analysis (SFCA) method of operation (Moore and Nenes, 2009) that allows high-resolution measurements of CCN concentration as a function of *s* over short periods of time. CCN measurements in this study are used to provide a proxy for chemical composition; although particles generated here are theoretically composed of one compound, impurities in the chemicals and water used during the particle generation process may affect particle volatility (especially when considerable volatilization is seen) and should be reflected in the CCN activity (Sections 4.4.1 and 4.4.3).

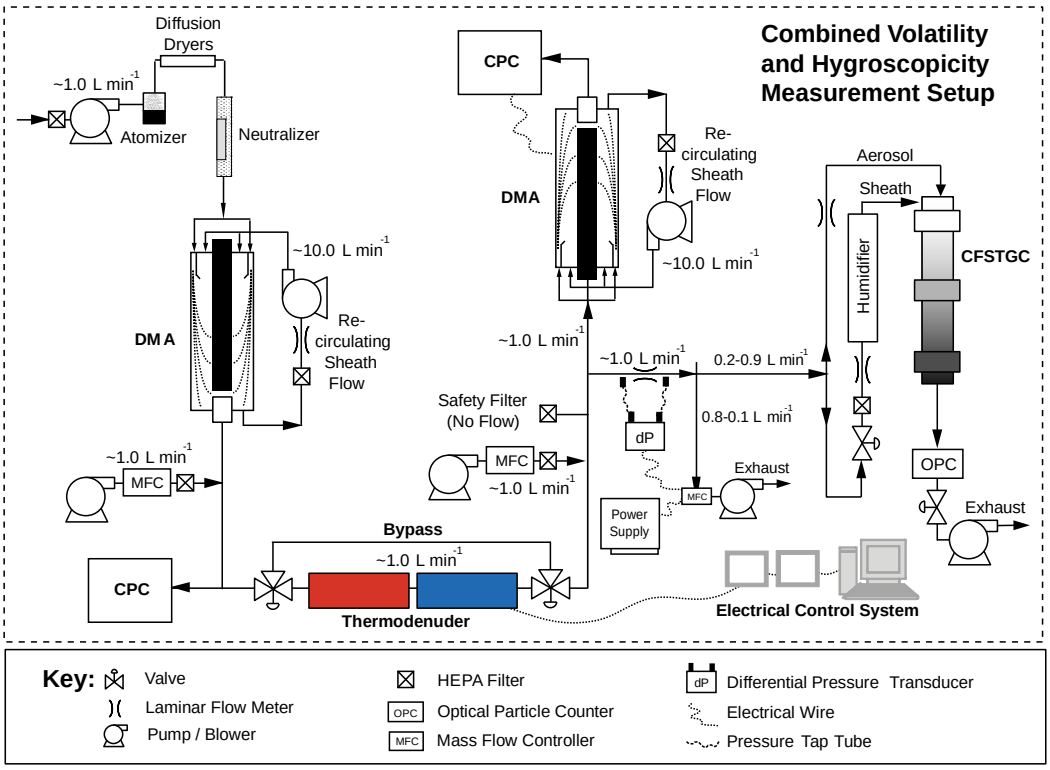

Figure 4.3: Experimental setup for combined volatility and hygroscopicity measurements.

In the instrument setup used, compounds in solution with deionized water are atomized. The droplet stream passes through two silica gel diffusion dryers, and the resulting dried particles are charge-neutralized by a Kr-85 (TSI, Model 3077A) or Po-210 bipolar charger source before entering a DMA. Filtered dilution air is introduced to the size-resolved aerosol stream before splitting to a CPC and computer-controlled three way valve that allows the stream to flow through the thermodenuder or a bypass line. This configuration enables us to operate as a combined Volatility Tandem DMA (Orsini et al., 1998; Rader and McMurry, 1986) and size-resolved CCN activity spectrometer. Additional dilution air is introduced before the flow is split to a scanning mobility particle sizer (SMPS; consisting of a DMA and CPC) which measures the aerosol size distribution exiting the thermodenuder system, and to a laminar flow box and the

CFSTGC, which gives the total number of activated particles (i.e., CCN). The laminar flow box is used to maintain a constant flow (1 L min^{-1}) which is introduced into the CFSTGC as needed, because the sample flow in CFSTGC column is constantly changing during SFCA operation. Accurate balancing of flows throughout the system is critical; the addition of an extra filter and valve open directly to room air after the thermodenuder and before the SMPS and SFCA systems ensures that there is no over- or under-pressurization of the flow lines during operation. All DMAs are operated with a sheath flow rate of 10 L min^{-1} and aerosol flow rate of 1 L min^{-1}. The top-to-bottom temperature difference in the CCN instrument is maintained at 12°C. Flow in the SFCA was linearly ramped from 0.2 to 0.9 L min^{-1} then back down to 0.2 L min^{-1} over 60 seconds, resulting in a CCN spectrum between ~0.30 to 0.80% *s*.

4.3.1.1 Thermodenuder Measurements

Polydisperse particles composed of pure organic acids that span almost 7 orders of magnitude in vapor pressure (Table C.1), including straight chain dicarboxylic acids (adipic acid, Fisher Scientific, 99% purity; azelaic acid, City Chemical LLC, 98% purity; malonic acid, Fisher Scientific, reagent grade; pimelic acid, Acros Organics, 99% purity; suberic acid, Acros Organic, 99% purity; succinic acid, Acros Organics, 99% purity) are first classified by a DMA. Particle concentration is then measured by a CPC before entering the thermodenuder (Figure 4.3). A SMPS measures the size distribution at the exit of the thermodenuder and concentration is given by the integrated concentration of the entire measured size distribution. Analysis of the entire distribution of the denuded aerosol is used to characterize the instrument response function (Section 4.2), from which

a characteristic mode diameter given by the SMPS size distribution is used to represent the exiting aerosol size for volatility and hygroscopicity interpretation.

The aerosol sampling schedule is outlined in Figure 4.4. Aerosol flow is automatically switched between the non-denuded bypass line (By) and thermodenuder line (TD) every 9 minutes. Aerosol sizes of approximately 70 to 150 nm are selected and allowed to flow through the system for 18 minutes each (9 minutes each from the bypass and thermodenuder). Three SMPS scans lasting for 135 s each (120 s for each upward voltage scan and 15 s for the downscan) are run consecutively 3 times for the bypass line and thermodenuder, respectively. The first SMPS scan begins 2 minutes into each 9 minute cycle, allowing time for the desired classified aerosol sample to flush through the instrumentation. Temperature in the thermodenuder is held constant until all sizes have been measured from both the bypass and thermodenuder; the temperature set point is then changed and requires 4 to 5 minutes to re-equilibrate (within 0.5°C) before the aerosol measurement cycle is repeated.

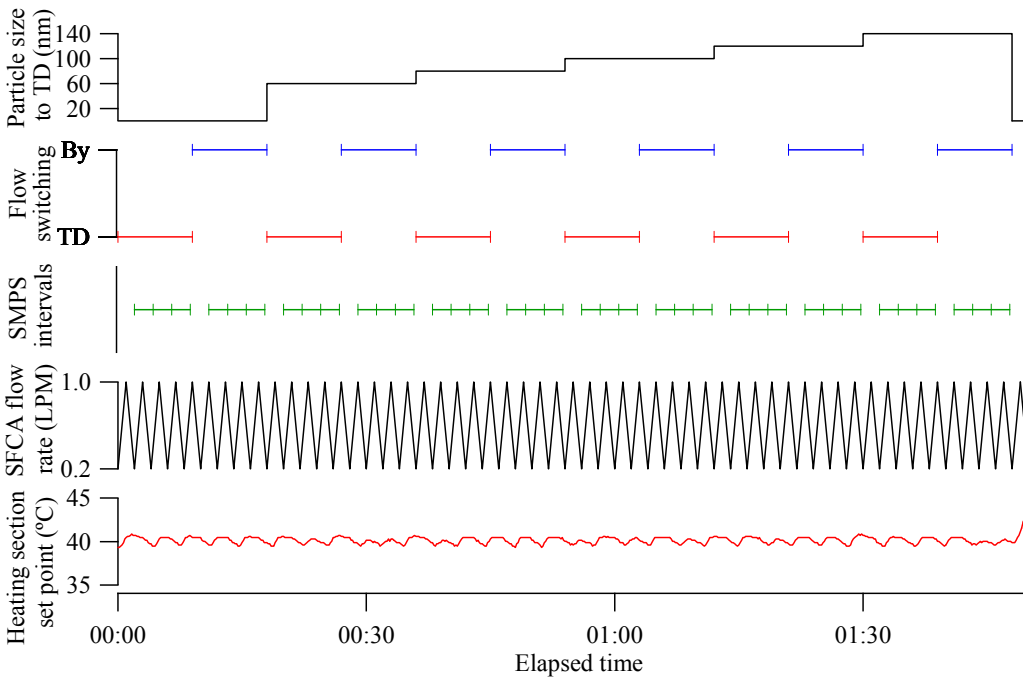

Figure 4.4: Sampling schedule for bypass (By) and thermodenuder (TD) aerosol samples during a single heating section set point temperature.

4.3.1.2 Obtaining Size-resolved Hygroscopicity

The ratio of CCN to CN concentration, termed the activation ratio, is expressed against instantaneous flow rate at each second during a SFCA upscan (downscans were not used in this study), to yield a curve that is fit to a sigmoidal activation ratio function (Moore and Nenes, 2009). The resulting critical flow rate, Q^*, where half of the CN are activated, is then determined. Flow rate, Q, is related to a characteristic supersaturation, s^*, using the calibration method described in Moore and Nenes (2009). s^* is then used to characterize the denuded aerosol hygroscopicity parameter, κ (Petters and Kreidenweis, 2007)

$$\kappa = \frac{4A^3}{27 d_p^3 s^{*2}} \tag{4.1}$$

where $A=(4M_w\sigma_w)/(RT\rho_w)$, and M_w, σ_w, and ρ_w are the molar mass, surface tension, and density, respectively, of water at the average mid-column temperature, T, in the CFSTGC

(~306 K). R is the universal gas constant, and d_p is the characteristic diameter of the denuded aerosol.

4.3.2 Modeling of Thermodenuder and Aerosol Response

The thermodenuder model consists of one module that determines the flow, temperature and volatilized organic vapor distribution inside the heating section for a given temperature and flow rate set point and another that simulates the semi-volatile partitioning of aerosol during its residence in the instrument. The modules can be separately executed, providing the advantage of resolving the flow and temperature fields once for a given set point for multiple inputs into the aerosol module.

The instrument model considers the full geometry of the flow, including the heating section, fittings, and cooling section. The axisymmetric gridding system, example fluid streamlines and aerosol sizes along them are presented in Figure 4.5. The influence of particle loading and proximity to the heating section walls is evident. Particles closest to the walls experience the most volatilization, owing to their relatively longer residence time in the heating section (Appendix D and Figure D.1). As expected, higher particle mass loadings lead to accumulation of volatilized vapors in the thermodenuder, which depresses the driving force for aerosol volatilization.

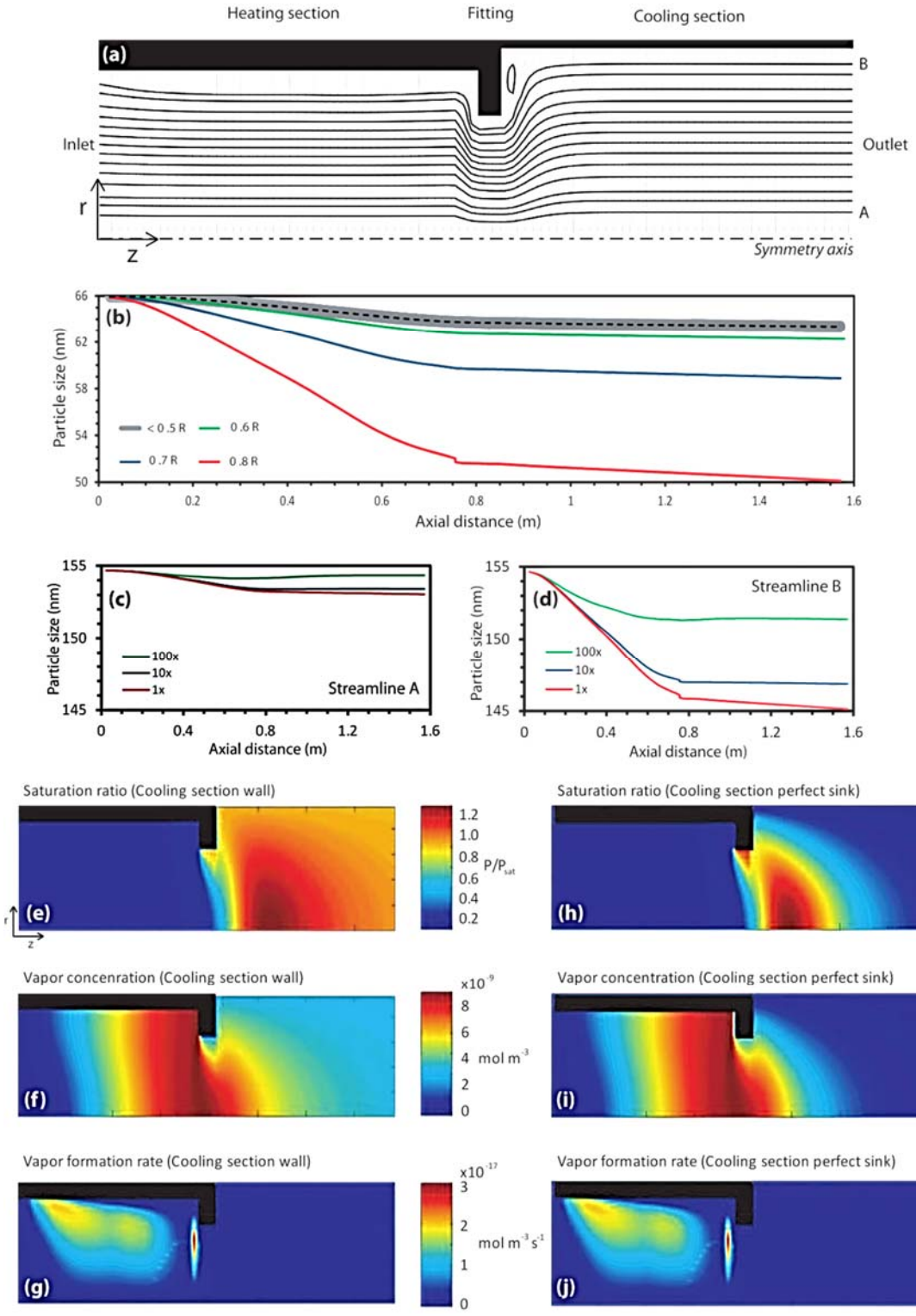
Heating section
Fitting
Cooling section
(a)
B
Inlet
Outlet
r
z
A
Symmetry axis
(b)
Particle size (nm)
< 0.5 R
0.6 R
0.7 R
0.8 R
Axial distance (m)
(c)
100x
10x
1x
Streamline A
Axial distance (m)
(d)
Streamline B
100x
10x
1x
Axial distance (m)
Saturation ratio (Cooling section wall)
(e)
P/P_sat
Saturation ratio (Cooling section perfect sink)
(h)
Vapor concenration (Cooling section wall)
(f)
x10^-9
mol m^-3
Vapor concentration (Cooling section perfect sink)
(i)
Vapor formation rate (Cooling section wall)
(g)
x10^-17
mol m^-3 s^-1
Vapor formation rate (Cooling section perfect sink)
(j)

Figure 4.5: Simulated thermodenuder geometry and fields for inlet monodisperse adipic acid aerosol with 1000 cm^{-3} concentration, 1 L min^{-1} flow rate and 60°C set point in the heating section. (a) Thermodenuder geometry with sample streamlines and gridding system. (b) Simulated sizes for a 66 nm inlet diameter aerosol as a function of distance from the centerline. (c) Simulated size for 155 nm inlet aerosol flowing at streamline A at 1, 10, and 100 times the nominal inlet concentration. (d) is similar to (c), but for streamline B. Contour plots of simulated organic vapor (e) saturation ratio, (f) concentration, and (g) formation rate, assuming the cooling section is an impermeable wall. (h), (i), and (j) are similar to (e), (f), (g), respectively, but assuming the cooling section is an impermeable wall. (h), (i), and (j) are similar to (e), (f), (g), respectively, but assuming the cooling section is a perfect sink of organic vapor. Cross-sectional schematic of the thermodenuder constructed and used for this study.

4.3.2.1 The Flow Field Module

The flow and temperature fields in the instrument are determined by numerically solving the Navier-Stokes, energy and volatilized species conservation equations at steady state (Appendix B). The equations are solved using a finite-volume formulation that uses a hybrid upwind-central differencing scheme to compute the convective/diffusive fluxes over each finite volume. The velocity grids are staggered with respect to the scalar field grids to ensure consistency in the pressure fields obtained during the solution. Solution of the hydrodynamic cycle (velocity and pressure fields) is obtained using the Semi-Implicit Method for Pressure Linked Equations (Patankar, 1980). A uniform grid was used for each variable, with 100 grid cells for each spatial coordinate, which ensures a solution that agrees to within a few percent of the asymptotic (with respect to grid density) limit (Figure 4.5). The boundary conditions to the flow problem are the inlet flow rate and the wall temperature profile obtained from the normalized, measured thermodenuder axial centerline temperature profiles, scaled to the set point temperature (Figure 4.2a). Fully solving the velocity and pressure fields requires considerable computational time which is acceptable as the resulting flow field is calculated once and then stored for repeated use

by the aerosol module. Examples of velocity, concentration and saturation fields are presented in Figure 4.5.

4.3.2.2 The Aerosol Module

The aerosol module treats the dynamic semi-volatile partitioning between the vapor and condensed (aerosol) phase. Aerosol volatilization is considered by Lagrangian tracking of particles along each streamline in the thermodenuder flow field; local conditions of temperature and gas-phase concentration of organic compounds are then used in the solution of the particle-to-gas mass transfer equations presented below. The aerosol distribution for each streamline is discretized into a number of aerosol size bins, each with a characteristic diameter and number concentration; each bin is then separately treated in terms of mass transfer through the gas phase. Coupling of the locally volatilized/condensed mass from/to the aerosol is accomplished through an iterative procedure with the gas-phase equations (Appendix B). The chemical composition for each aerosol section may be treated independently; one set of values is used in this study for all sections, leaving the treatment for chemically complex aerosol for a future study.

Gas-to-particle mass transfer is described with the following equation (Seinfeld and Pandis, 2006):

$$d_p \frac{d(d_p)}{dt} = \frac{\frac{P_\infty}{P^o} - \exp\left(\frac{4M\sigma}{R\rho D_p T_\infty}\right)}{\frac{\rho R T_\infty}{4\mathcal{D}_{AB} M P^o \Phi} + \frac{\Delta H \rho}{4kT_\infty}\left(\frac{\Delta H M}{RT_\infty} - 1\right)} \tag{4.2}$$

where T_∞ is the local air temperature inside the thermodenuder, P^o is the saturation vapor pressure of the volatilizing species at T_∞, P_∞ is the local vapor pressure of the volatilizing species, ΔH is its specific enthalpy of phase change, and R is the ideal gas constant. ΔH could represent either the enthalpy of vaporization or sublimation, depending on the

phase of the volatilizing aerosol. ρ, d_p, M, and σ are the density, diameter, molar mass, and interfacial energy of the aerosol, respectively. The thermal conductivity of air is represented by k. D_{AB} is the diffusivity of the volatilizing species (B) in air (A). Φ is the value of the Fuchs-Sutugin correction factor for non-continuum effects (presented below).

The saturation vapor pressure for the aerosol is assumed to follow the Clausius-Clapeyron relationship:

$$P^o(T_\infty) = P^o(T_o)\exp\left[\frac{\mathrm{M}\Delta H}{R}\left(\frac{1}{T_o} - \frac{1}{T_\infty}\right)\right] \quad (4.3)$$

where T_o = 298K. ΔH is assumed to be constant over the temperature range considered and is treated as a fitting parameter for the model optimization. Including the temperature dependence of ΔH would potentially introduce a large uncertainty in the retrieved heat capacity unless a wide range of temperature is considered, so it is not considered here.

The thermal conductivity, k, of air corrected for non-continuum effects is given by

$$k = \frac{k_a}{1+\frac{2k_a}{\alpha_T d_p \rho c_p}\left(\frac{2\pi M_a}{RT_\infty}\right)^{1/2}} \quad (4.4)$$

where k_a is the thermal conductivity of air in the continuum regime, $k_a = 10^{-3}(4.39 + 0.071T_\infty)$ with units of J m^{-1} s^{-1} K^{-1}, c_p is the specific heat capacity of air (1006.1 J kg^{-1} K^{-1}), and α_T is the thermal accommodation coefficient, here considered to be unity (Seinfeld and Pandis, 2006). M_a is the molar mass of air (0.029 kg mol^{-1}).

Existing studies that employ a kinetic model for evaporation in a thermodenuder make various assumptions regarding the diffusion coefficient, D_{AB}. For aerosol of known composition, the Hirschfelder, Bird, and Spotz formula (Bird, 2002) is often employed using available Lennard-Jones parameters (e.g., Bilde et al., 2003). A constant diffusion

coefficient may be prescribed in the investigation of more complex mixtures or to generalize instrument conditions (e.g., Fuentes and McFiggans, 2012; Cappa and Jimenez, 2010). In this study, the method of Fuller et al. (1966) is used to compute D_{AB} ($cm^2\ s^{-1}$) for a binary mixture of air (A) and the evaporating component (B):

$$D_{AB} = \frac{10^{-3}T^{1.75}\left(\frac{1}{M_A}+\frac{1}{M_B}\right)^{1/2}}{P\left(v_A^{1/3}+v_B^{1/3}\right)^2} \tag{4.5}$$

where v_A and v_B are the empirically-defined "diffusion volumes" for species A and B, respectively. For a particular molecule, Fuller et al. (1966) provide correlations for computing the diffusion volume as the sum of contributions from individual atoms along with modifications for certain structural features (e.g., rings). A study considering diffusivities of low volatility compounds in various background gases (Ravindran, 1979), found that it was a comparably accurate estimation technique for diffusion in low molecular weight carrier gases, being outperformed only by one other empirical fit to diffusional data. The calculated diffusion volumes for each compound in this study are provided in Table 4.1 along with corresponding densities and molecular weights.

The Fuchs-Sutugin non-continuum correction factor, Φ, in Equation (4.2) is given by (Seinfeld and Pandis, 2006; Fuchs and Sutugin, 1971):

$$\phi = \frac{0.75\alpha(1+\mathrm{Kn})}{\mathrm{Kn}^2+\mathrm{Kn}+0.283\mathrm{Kn}\alpha+0.75\alpha} \tag{4.6}$$

where $\mathrm{Kn} = \frac{2\lambda_{AB}}{d_p}$ is the Knudsen number, and the mean free path, λ_{AB}, of the volatilizing compound in air is $\lambda_{AB} = \frac{3D_{AB}}{\bar{c}_B}$, where $\bar{c}_B$ is the thermal speed of the gas phase component, $\bar{c}_B = \left(\frac{8RT}{\pi M_B}\right)^{1/2}$, and α is the accommodation (evaporation) coefficient.

Table 4.1: Thermodynamic and transport properties for investigated compounds

Organic Acid	Molar Mass (kg mol^{-1})	Density (kg m^{-3})	Diffusion Volume (cm^{-3})	Interfacial Energy (J m^{-2})*	Accommodation/Evaporation Coefficient**
Adipic Acid	0.14614	1362	140.72	0.06 (0.06)[A] 0.17 (0.12)[B] 0.032[C] 0.028[D]	0.10 (0.02)[B]
Azelaic Acid	0.18822	1251	202.1	0.18 (0.18)[A] 0.039[D]	-
Malonic Acid	0.10406	1616	79.34	0.02 (0.02)[A] 0.045[E]	-
Pimelic Acid	0.16017	1281	161.18	0.08 (0.08)[A] 0.23 (0.08)[B]	0.32 (0.05)[B]
Suberic Acid	0.17419	1272	181.64	0.1 (0.1)[A]	-
Succinic Acid	0.11809	1566	99.8	0.125 (0.125)[A] 0.15 (0.07)[B] 0.075[D] 0.045[E]	0.09 (0.02)[B]

*Absolute uncertainty in values is provided in brackets where available. Values obtained from temperature-dependent expressions at 50°C.
**$\alpha = 1$ used in base model calculations
[A]Bilde et al. (2003)
[B]Saleh et al. (2009), adjusted up by 30% per Saleh et al. (2012)
[C]Riipinen et al. (2007), from temperature-dependent equation
[D]Yaws (2003), from temperature-dependent equation
[E]Hyvärinen et al. (2006), from temperature-dependent equation

Equation (4.2) is numerically integrated using the DVODE (Variable-coefficient Ordinary Differential Equation solver) (Brown, 1989) to determine the diameter of aerosol particles when they exit the instrument. This is done for each streamline, initializing the particle size to the DMA-observed inlet condition. Particles are then allowed to follow each streamline, based on the local value of velocity (in both axial and radial directions). During the integration of Equation (4.2), thermophysical parameters are allowed to vary based on the temperature variations experienced by the particles as they flow through the instrument. The volume-weighted average exit diameter from the thermodenuder is taken as the modeled outlet diameter, d_{pm},

$$d_{pm} = \bar{d}_{p,v} = \frac{\int_0^{R_{TD}} d_p u_z r \, dr}{\int_0^{R_{TD}} u_z r \, dr} \tag{4.7}$$

where u_z represents the axial velocity at the exit of the heating section, r is the radial distance from the centerline, R_{TD} is the inner radius of the heated section, and d_p is the particle diameter at the end of each streamline. These model output diameters, along with the observed final aerosol diameters, are utilized in the optimization routine to retrieve optimal estimates of volatility parameters. Examples of predicted aerosol size profiles with the fully-coupled model are provided in Figure 4.5. As aerosol loading increases, less of the particle volatilizes owing to the increasingly saturated state of the gas phase.

Aerosol were assumed to be spherical with physical diameter equal to their mobility diameter. Irregularly-shaped aerosol can be accounted for by the inclusion of a shape factor, χ. For instance, a previous study found χ for solid (crystalline) adipic and azelaic acid aerosol to range between 1.05 and 1.1 (Saleh et al., 2010). While this estimated shape factor is not representative of all OA, it provides a possible range of systematic correction to the DMA sizing required. Aerosol in this study is generated from atomization of an unsaturated solution at room temperature, and it is postulated that the dried aerosol are sufficiently amorphous considering the short drying time allowed, compared to experimental conditions in the study of Saleh et al. (2010). Salo et al. (2010) indicated that solvent inclusions are unlikely to be present in aerosol generated with a drying setup similar to Saleh et al. (2010), although the hysteresis of aerosol efflorescence and the formation of eutectics allows for the presence of both liquid and solid phase aerosol. Calculations of volatility parameters for separate measurements suggest that this occurred for pimelic acid in their experiments. With these results in

mind, the aerosol generated in this study can likely be considered an amorphous solid, although the vapor pressure retrievals may be sensitive to the aerosol phase state.

4.3.2.3 Optimal Estimation of Volatility Parameters and Uncertainty

Optimal estimation of the parameters used in the evaporation model is accomplished through the use of the Levenberg-Marquardt algorithm as implemented in the International Mathematical and Statistical Library subroutine ZXSSQ (International Mathematical and Statistical Library; Ver. 6/1/1982). The output diameter from the model is first calculated for an initial guess of volatility parameters. An objective function expressing the deviation between predicted and observed diameter is then minimized to yield optimal values of volatility parameters, as determined below.

Laboratory data was collected for each single component aerosol consisting of the inlet diameters ($d_{p,in}$) and associated outlet mode diameters ($d_{p,out}$) from the SMPS after the thermodenuder at three different temperature settings, T_{set}, with consistent flow rate settings, Q_{set}. Not all values of $d_{p,out}$, however, could be used owing primarily to the effects of impurities and multiple charging. The determination of the appropriate $d_{p,out}$ to be used in the model fitting is discussed in Section 4.4.2. If M independent observations (i.e. unique combinations of $d_{p,in}$, T_{set}, and Q_{set} for a particular aerosol) are available, N independent parameters (represented by the aerosol property vector, $\vec{x}^N$) can be optimally fit to the data, provided that N < M (for parameter robustness). Volatility parameters and uncertainty ranges for each organic acid investigated were obtained through the use of the ZXSSQ optimization routine coupled with the instrument model. The optimization routine minimizes the returned residuals of the aerosol module where the cost function is defined as

$$Q = \sum_{i=1}^{\mathrm{M}} \left(d_{p,out,i} - d_{pm,i}\right)^2 \quad (4.8)$$

where i = 1, … , M are the data points available for fitting with $d_{p,out}$ representing the observed diameter and d_{pm} is the diameter computed by the aerosol module.

In this study, optimal values for $P^o(T_o)$ and ΔH are obtained for the single component aerosol (N = 2), while other variables (i.e. density, molecular weight, diffusivity, and the accommodation coefficient) are constrained from literature values or estimated. The initial guesses used in the iterative optimization procedure were obtained from a more typical approach to TDMA data inversion (e.g., Salo et al. 2010, Rader & McMurry 1986).While it is possible to increase N provided a large enough value of M, doing so decreases the confidence of the fit and increases sensitivity to the initial guess of the parameter used in the iterative scheme. Thus, the more observations fit to the least number of parameters provides the most robust parameter estimates. The optimization method, described in the following, additionally provides an estimate of parameter uncertainty. It should be noted that both $P^o(T_o)$ and ΔH are simultaneously fitted to the all experimental data at various $d_{p,in}$, and T_{set} and for particular, fixed, values of the accommodation coefficient and surface free energy in the optimization algorithm, so no assumptions regarding the fitted parameter values are made *a priori*.

The Levenberg-Marquardt algorithm is an unconstrained optimization method which necessitated the use of a transformation for $\vec{x}^N$ to avoid it returning unphysical (i.e., negative) optimal values. In this study, the optimal physical volatility parameters ($\vec{x}^N$) are related to the optimal values obtained by ZXSSQ ($\vec{P}^N$) as $x_i = (P_i)^2$. To facilitate the optimization, ΔH was made to be the same magnitude as the saturation vapor pressure

within the optimization space using the initial guesses of both parameters to obtain a scaling factor:

$$P^o(T_o) = (P_1)^2;\ \Delta H = \frac{(P_2)^2}{s} \tag{4.9}$$

with $s = \frac{P^o_{initial}}{\Delta H_{initial}}$ and P_1, P_2 the optimal parameters determined by ZXSSQ. This variable transformation is taken into consideration in the uncertainty analysis.

ZXSSQ calculates the finite-difference Jacobian matrix ($\underline{J}$) through execution of the aerosol module at different settings of the optimization-space parameters, $\vec{P}^N$, during the minimization of the cost function. Each element of $\underline{J}$ is defined as the partial derivative of the residual terms with respect to perturbations in each parameter in the optimization space:

$$J_{ij} = \frac{\partial}{\partial P_j}\left(d_{p,out,i} - d_{pm,i}\right) = \frac{\partial d_{p,out,i}}{\partial P_j} - \frac{\partial d_{pm,i}}{\partial P_j} \cong \frac{\Delta d_{p,out,i}}{\Delta P_j} - \frac{\Delta d_{pm,i}}{\Delta P_j} \tag{4.10}$$

During the parameter optimization, $\Delta d_{p,out,i} = 0$ since $d_{p,out}$ is unaffected by changes in P_j; thus $\underline{J}_{ij}$ can be interpreted as the $d_{pm,i}$ sensitivity to variations in P_j (with a sign change). The volatility parameter uncertainty ranges are determined by first applying $\underline{J}$ to calculate ΔP_{ij} for a given variation in inlet diameter, $\Delta d_{p,out,i}$, which is taken to represent the uncertainty in the measured outlet diameters (i.e., the width of the DMA transfer function). In this case, $\Delta d_{pm,i} = 0$ and the relationship to $\underline{J}$ is defined as

$$\Delta P_{ij} = \frac{\Delta d_{p,out,i}}{J_{ij}} \tag{4.11}$$

Propagating the relative uncertainty in P_j through to x_j we get

$$\frac{\Delta x_{ij}}{x_j} = 2\left(\frac{\Delta P_{ij}}{P_j}\right) = \frac{2\Delta d_{p,out,i}}{P_j J_{ij}} \tag{4.12}$$

This provides an estimate of the uncertainty in each parameter, x_j, at every observed

outlet diameter, $d_{p,out}$. These estimates of uncertainty in the same parameter do not have much meaning when expressed individually, as all observations were combined in the model fitting. They may also vary considerably from measurements to measurement. Therefore, a weighted average of the uncertainty across all measurements is taken as

$$\Delta x_j = \frac{\sum_i^M w_i \Delta x_{ij}}{\sum_i^M w_i} \tag{4.13}$$

with weights, w_i, defined as the observed diameter change experienced by the aerosol

$$w_i = \left(d_{p,in,i} - d_{p,out,i}\right). \tag{4.14}$$

4.4 RESULTS

Particles composed of single organic compounds with known properties were generated and introduced into the thermodenuder and SFCA to characterize the instrument response functions, or volatilization profiles, of input versus final particle size at several different temperatures in the thermodenuder. The instrument model is then used to interpret the profiles and retrieve volatility parameters which were then compared against published literature values.

4.4.1 Volatility Measurements

An example of size distribution evolution for a given classified organic component at three different thermodenuder temperatures is shown in Figure 4.6. As temperature becomes greater, increased volatilization results in the size distribution exiting the thermodenuder shifting to smaller sizes. Inlet and exit sizes for each compound studied at all temperatures considered are presented in Figure 4.7. As expected, the thermodenuded particle size mode is a monotonic function of initial size; outlet particle size decreases as temperature is increased. In cases where particles are highly volatilized, final particle size

reaches a lower limit of approximately 10 to 30 nm where further volatilization ceases (Figure 4.7). This size limit is the result of impurities in the organic compounds and water used for atomization and is described in detail in Section 4.4.2.

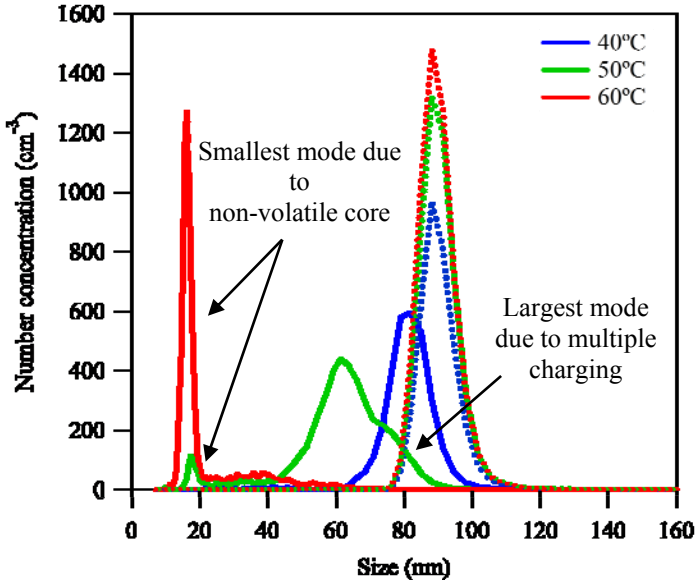

Figure 4.6: Example size distributions measured from the thermodenuder (solid lines) and bypass (dotted lines) at 40 (blue), 50 (green) and 60°C (red) for azelaic acid with initial size of approximately 85 nm. Note that particles loadings vary between experiments.

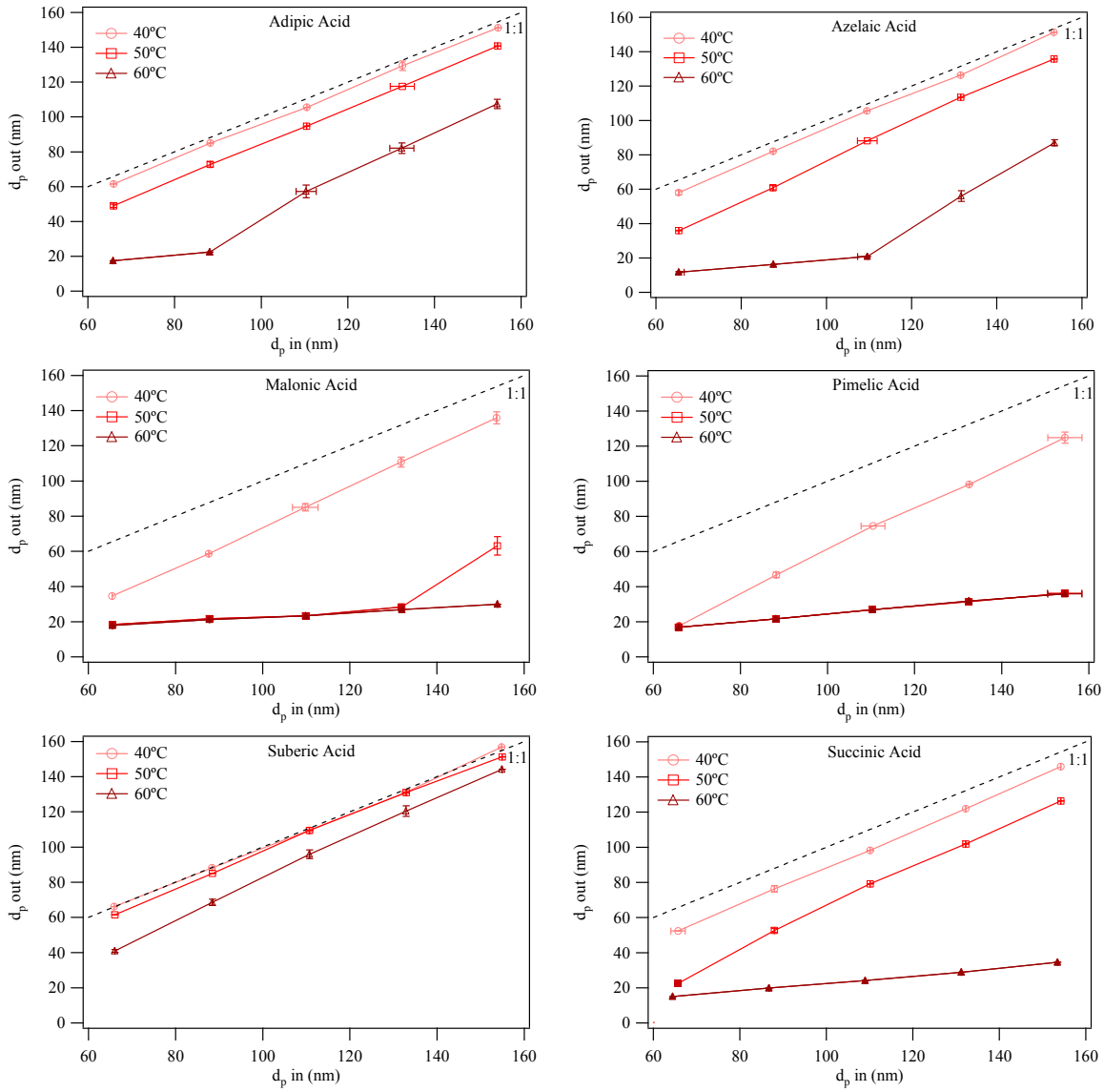

Figure 4.7: Change in diameter for several pure organic acids after passing through the thermodenuder at 40, 50, and 60°C. Solid symbols represent points resulting from non-volatile cores and discarded from model fitting. Vertical and horizontal error bars represent the standard deviation in the mode measured during three SMPS scans collected from the thermodenuder and bypass, respectively.

4.4.2 Interpreting the Presence of Multiple Modes in Thermodenuded Size Distributions

Investigation of measured size distributions exiting the thermodenuder suggest that as particles are heated, up to three different modes may emerge. This is concerning, as one particular outlet diameter should result from any given inlet diameter and thermodenuder temperature; deviations from this behavior, if due to instrument artifacts (e.g., a result of non-ideal flow or nucleation of supersaturated organic vapors in the cooling section) can bias retrieved volatility parameters. Understanding these modes requires a full understanding of the thermodenuder instrument response.

The smallest size mode is only observed when aerosol are highly volatilized and does not appear at relatively lower temperatures (Figure 4.6). Non-volatile components in the particle would leave behind a detectable residual particle when the organic fraction has completely volatilized. This explains the presence of bimodal distributions (Figure 4.6), as the organic aerosol flowing along streamlines close to the thermodenuder wall volatilizes completely, leaving behind the non-volatile mode while those nearest the centerline are not heated for enough time, consistent with the vapor source rates shown in Figure 4.5. The lower size mode diameter does not appear to vary with temperature set point, indicating that it indeed reflects remnant low-volatility material, as otherwise the particles would further shrink or disappear as temperature is increased. Analysis of the size of the aerosol obtained through the reported compound impurity yields particles consistent with the measured size (Appendix E and Salo et al., 2010). Nucleation of supersaturated vapor at the exit of the heating section also is also an unlikely source of the small particles, as suggested by the analysis of the experimental data (Appendix E).

The largest mode present can consistently be attributed to the presence of doubly-charged particles. Indeed, the simulations yield output diameters consistent with the largest mode for all species considered, even when the doubly-charged size is used as the initial condition (Appendix E).

Based on the above discussion, the mode diameter used for volatility calculations was the middle mode when a tri-modal distribution was present. Additionally, unimodal data within the range of the non-volatile core were discarded; bimodal data with an observable mode larger than that of the non-volatile core utilized the large mode size.

4.4.3 Fitted Volatility Parameters, Uncertainties, and Literature Comparison

Volatility parameters and associated uncertainties were obtained from the model fitting procedure (Section 4.3.2.3). The optimal parameters for each compound that presented the least residuals against the laboratory data out of the various initial conditions were taken as the model fits and are presented in Table 4.2. For each compound considered, the observed inlet and outlet diameters are plotted alongside the fitted model response in Figure 4.8. Here, solid curves represent the model evaluated at one set of the optimized parameters from Table 4.2. The dashed curves are model evaluations made at the upper and lower bounds of the uncertainty ranges in the retrieved parameters. Open circles are the raw data – the maximum mode diameter – initially obtained from the SMPS size distributions. Starred points are the data that was actually used in the model fitting, adjusted according to discussion of Section 4.4.2. The inclusion of the unfitted data illustrates the consistency of the thermodenuder model, as the model outlet diameter is either lower than or equal to the observed non-volatile diameters within the uncertainty of the volatility parameter estimate.

Table 4.2: Reference saturation vapor pressure (at 298 K) and ΔH. C^* is calculated using properties from Table 4.1. Results of different model runs are identified by the surface tension (σ) source value and are also numbered consistently with Figure 4.9.

Organic Acid	**σ (N m^{-1})**	**P^o(298K) (Pa×10^{-5})**			**ΔH (J mol^{-1}×10^{5})**			**C^*(298K) (µg m^{-3})**	**Uncert. (%)**
		Max	Min	Avg	Max	Min	Avg		
Adipic Acid									
1: Bilde et al. (2003)	0.06	1.13	0.34	0.73	1.42	0.99	1.20	0.43	54
2: Riipinen et al. (2007)	0.032	1.21	0.36	0.78	1.41	0.99	1.20	0.46	54
3: Saleh et al. (2009)	0.17	0.82	0.23	0.52	1.47	1.01	1.24	0.31	57
4: Saleh et al. (2009)*	0.17	7.47	2.15	4.81	1.46	0.98	1.22	2.8	55
5: Yaws (2003)	0.028	1.20	0.35	0.78	1.41	0.99	1.20	0.46	55
Azelaic Acid									
6: Bilde et al. (2003)	0.18	0.63	0.26	0.44	1.47	1.14	1.31	0.34	41
7: Yaws (2003)	0.039	1.12	0.51	0.81	1.39	1.09	1.24	0.62	38
Malonic Acid									
8: Bilde et al. (2003)	0.02	10.13	6.57	8.35	1.38	1.16	1.27	3.5	21
9: Hyvärinen et al. (2006)	0.045	9.03	5.86	7.45	1.42	1.19	1.31	3.1	21
Suberic Acid									
10: Bilde et al. (2003)	0.1	0.19	-0.09	0.05	2.12	0.77	1.44	0.036	271
Succinic Acid									
11: Bilde et al. (2003)	0.125	5.90	1.97	3.93	1.21	0.74	0.98	1.9	50
12: Hyvärinen et al. (2006)	0.045	7.29	2.64	4.97	1.15	0.71	0.93	2.4	47
13: Saleh et al. (2009)	0.15	6.42	2.20	4.31	1.15	0.70	0.93	2.1	49
14: Saleh et al. (2009)*	0.15	68.40	25.20	46.80	1.12	0.68	0.90	22	46
15: Yaws (2003)	0.075	7.13	2.42	4.77	1.17	0.70	0.93	2.3	49

*Accommodation/evaporation coefficient changed from unity to available literature value

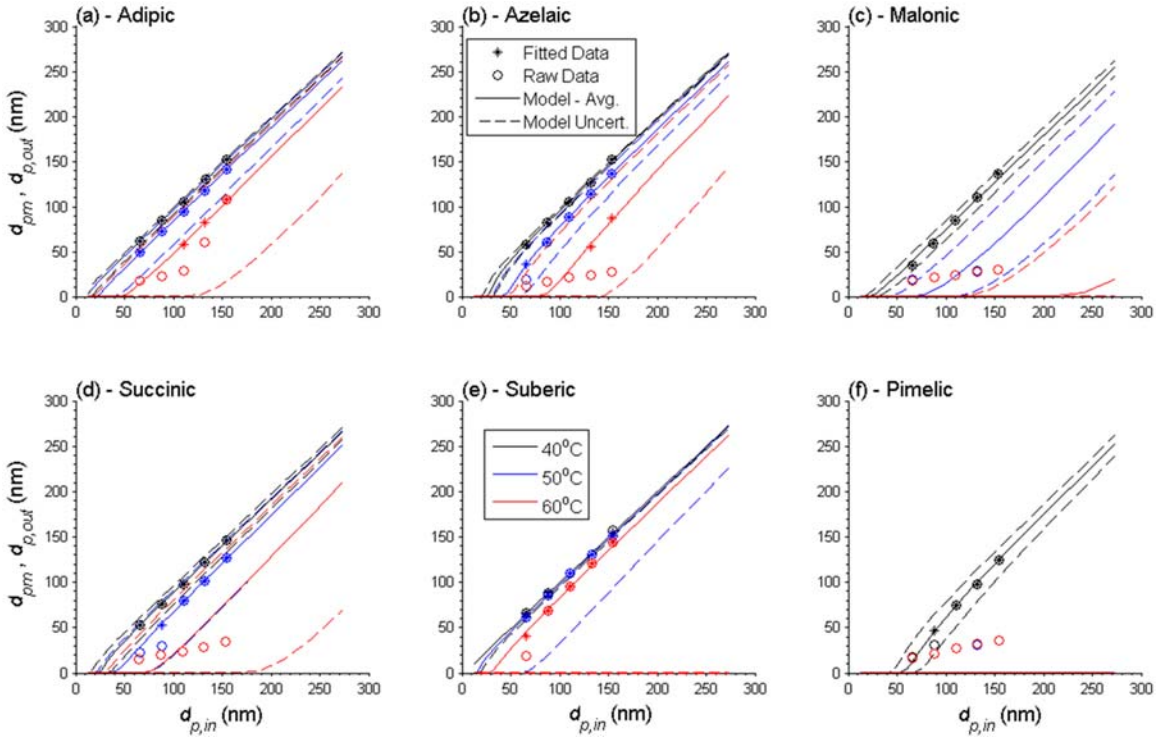

Figure 4.8: Thermodenuder model response overlaid with laboratory observations for each volatility measurement considered. Solid curves represent the model evaluated at one set of the optimized parameters from Table 4.1. The dashed curves are model evaluations made at the upper and lower bounds of the uncertainty ranges in the retrieved parameters. The points plotted indicate corresponding inlet and outlet mode diameter values. Starred points represented data that was fitted to the model. Open circles separate from the starred points are data affected by non-volatile cores (and were not considered in the fitting procedure). Each colored set of curves and points represents measurements made at a particular temperature (indicated by the legend). Dashed curves indicate the uncertainty range of the model response.

In the model optimizations, the literature value used for the interfacial energy was varied to assess the sensitivity of the retrieved parameters. The accommodation/evaporation coefficient was assumed to be unity by default but was also varied to literature values in Table 4.1 when available. Figure 4.9 presents the results of the uncertainty analysis and compares the fitted parameters with published data. Blue points with red numbers in each plot represent the results of the model runs indicated in Table 4.2 where the values for interfacial energy and (in two cases) accommodation

coefficient were varied. Additional simulations were carried out to assess the sensitivity of these results to the model geometry (inclusion of the cooling section), impact of varying the accommodation coefficient for all data, and oscillations in the wall temperature profile and inlet temperature on the order of experimental observations. For all compounds, changes in interfacial energy vary the retrieved values of P^o and ΔH to within uncertainty. This is consistent with a low impact of the Kelvin effect on equilibrium vapor pressure for sizes larger than those corresponding to non-volatile cores in the data. Put together, these results indicate that for our experimental conditions, only the sensitivity to choice of accommodation coefficient had a significant impact (outside of estimated error ranges) on the retrieved $P^o(T_o)$, corresponding to a direct proportionality between the two parameters (see Figure D.1).

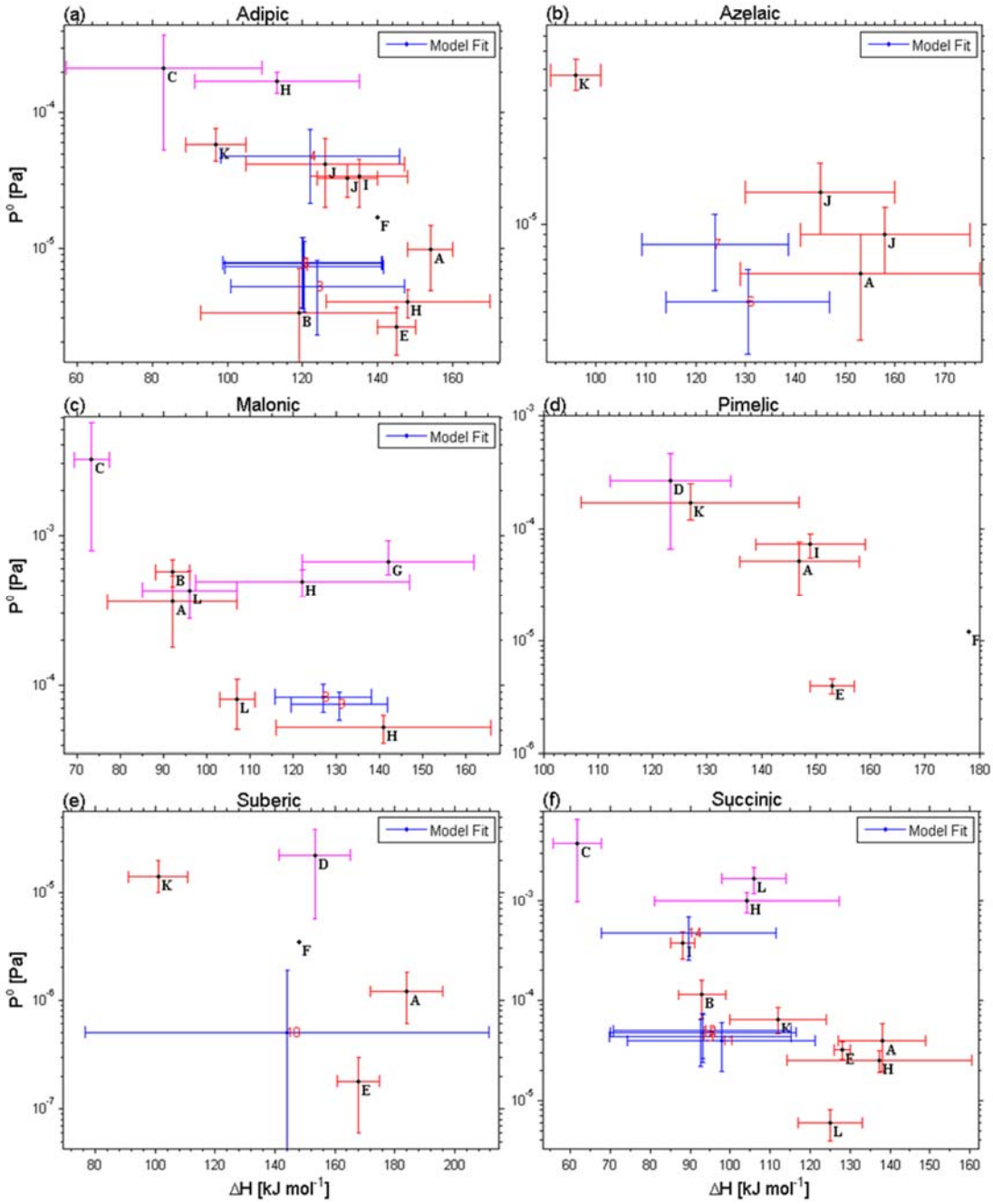

Figure 4.9: Volatility parameters and sensitivity tests for select compounds compared against literature data. Blue bars/points indicate values obtained from measurements with each one corresponding to different numbered rows of Table 4.2. Red (magenta) bars refer to literature values reported for solid (liquid) phase data. Note that (b) excludes the outlier value from Cappa et al. (2007). Plotted literature data (letters) correspond to sources as follows: A (Bilde et al., 2003), B (Booth et al., 2009), C (Booth et al., 2010), D (Booth et al., 2011), E (Cappa et al., 2007), F (Chattopadhyay et al., 2001), G (Pope et al., 2010), H (Riipinen et al., 2007), I (Saleh et al., 2009), J (Saleh et al., 2010), K (Salo et al., 2010), L (Soonsin et al., 2010).

In general, retrieved parameters for adipic acid are within the literature spread of volatility parameters. The optimal parameters for azelaic acid appear to be in the appropriate range for P^o but with slightly lower ΔH than the available literature. Optimal parameters for malonic acid (Figure 4.9c) agree to within uncertainty with Riipinen et al. (2007). Results for succinic acid (Figure 4.9f) appear consistent with estimates of solid P^o from various literature sources. Adjusting the accommodation/evaporation coefficient resulted in a significant change in the fitted parameters, placing it in agreement with the results of Saleh et al. (2009). The model fitting for pimelic acid is not possible, since only points at one temperature set point were uninfluenced by insoluble cores and available for fitting (Figure 4.9f). Thus, the numeric results for the fitted volatility parameters are not included in Table 4.2 or Figure 4.9. Suberic acid results are subject to large uncertainty (Table 4.2, Figure 4.9e) owing to the limited volatilization observed. This occurred because the observed size change of the aerosol was smaller than the uncertainty range obtained from the DMA transfer function for the inlet diameters for all but three of the data points. Thus the optimal parameter uncertainties calculated by propagating the measurement uncertainty through the Jacobian returned by the optimization routine (see Section 4.3.2.3) yielded very large values because the perturbation used ($\Delta d_{p,in}$) was greater than the observed size change used to fit the model. However, the estimate still provides an upper limit on suberic acid volatility which is in agreement with the Bilde et al. (2003) P^o and ΔH values.

An interesting aspect of the analysis is in the effect of particle phase on vapor pressure. Given the potentially large difference between vapor pressure between a solid and supercooled liquid substance (at the same temperature), comparison of the fitted

model volatility parameters to the available literature data for solid and liquid phases of the components can potentially be used to follow the phase transitions through an experiment. The resulting phase change (vaporization if liquid, or sublimation if solid) could be concluded based on the literature comparison since either follow the Clausius-Clapeyron relationship, and the use of the Kelvin effect as formulated in Equation (4.2) would be valid for either a liquid or amorphous solid aerosol (Tao and McMurray, 1989). For example, the succinic acid aerosol generated in this study behaved most consistently with being a solid. If vapor pressure inferences are accompanied with a more accurate and direct method to determine particle phase (e.g., Virtanen et al., 2010), then one could confirm the above and also provide an important affirmation of the modeling framework and instrument data analysis.

4.4.4 Aerosol Hygroscopicity

As only pure components are sampled and temperature does not vary considerably, κ should remain effectively constant through each experiment regardless of size and sampling from the bypass line or thermodenuder. κ values are calculated for each compound and averaged for all particle size and temperature measurements from the bypass, κ_{By}, thermodenuder, κ_{TD}, and bypass and thermodenuder combined, κ_{Tot} (Table 4.3). When a significant fraction of multiply charged particles are present in the CFSTGC, activation will begin at a lower critical supersaturation in the instrument, impacting the calculation of κ using Equation (4.1). This can be avoided by correcting the sigmoidal fitting curve for multiply charged particles (e.g., Moore et al., 2010; Moore and Nenes, 2009). Impurities in the chemical compounds or water used for atomization may potentially impact the κ of highly volatilized particles when the volume fraction of the

impurity becomes large enough. The consistent values of κ, indicated by both the averages and standard deviations in κ measured for a given compound in the bypass and thermodenuder, confirm the non-volatile residuals do not impact total κ measurements as they are not present in sufficient amounts or exhibit similar κ to the pure compound. In the case of the non-volatile residual particles, Equation (4.1) shows that at the highest supersaturations in the instrument (~0.80%), even a highly hygroscopic, pure salt particle such as NaCl ($\kappa \approx 1.2$; Petters and Kreidenweis, 2007) would need to have a diameter of at least 25 nm to activate. Though residual particle sizes larger than 25 nm could theoretically activate based on the previous calculations if they had a high value of κ, no thermodenuded particles less than approximately 70 nm in diameter are shown to activate into CCN, indicating that the non-volatile residuals exhibit low hygroscopicity.

All experimental values of κ agree to uncertainty with reported literature values. There is no clear shift to higher or lower κ values between the measured values and the range of literature values, further demonstrating that the potentially increased presence of impurities during the volatilization of particles does not appear to cause a particular shift in hygroscopic behavior of the measured compounds.

Table 4.3: Hygroscopicity values of pure organic compounds from this and published studies. Values in parentheses represent standard deviations unless indicated otherwise.

Organic Acid	κ_{By}	κ_{TD}	κ_{Tot}
Adipic Acid			
This work	0.022 (0.002)	0.024 (0.002)	0.023 (0.002)
Kuwata et al. (2012)			0.002 (±0.001)[a]
Rissman et al. (2007)			0.059 (+0.021; -0.014)[b]
Huff Hartz et al. (2006)			0.003 (+0.002; -0.001)[b]
Broekhuizen et al. (2004)			0.096 (n/a)[c]
Raymond and Pandis (2002)			0.020 (+0.018; -0.008)[b, d]
Prenni et al. (2001)			0.014 (n/a)[b]
Corrigan and Novakov (1999)			0.030 (n/a)[b,d]
Cruz and Pandis (1997)			0.099 (+0.048; -0.029)[b, d]
Azelaic Acid			
This work	0.061 (0.007)	0.057 (0.005)	0.060 (0.006)
Kuwata et al. (2012)			0.03 (±0.01)[a]
Huff Hartz et al. (2006)			0.022 (+0.018; -0.009)[b]
Malonic Acid			
This work	0.281 (0.034)	0.259 (0.052)	0.277 (0.037)
Kumar et al. (2003)			0.227 (±0.028)
Prenni et al. (2001)			0.237 (n/a)[b]
Pimelic Acid			
This work	0.213 (0.016)	0.189 (0.014)	0.210 (0.017)
Kuwata et al. (2012)			0.15 (±0.01)[a]
Frosch et al. (2010)			0.15 (±0.04)
Huff Hartz et al. (2006)			0.140 (+0.109; -0.054)[b]
Suberic Acid			
This work	0.007 (0.000)	n/a	0.007 (0.000)
Kuwata et al. (2012)			0.001 (n/a)[a]
Succinic Acid			
This work	0.285 (0.029)	0.239 (0.030)	0.273 (0.035)
Rissman et al. (2007)			0.480 (+0.174; -0.117)[b]
Huff Hartz et al. (2006)			0.140 (+0.109; -0.054)[b]
Hori et al. (2003)			0.231 (±0.065)[e]
Prenni et al. (2001)			0.310 (n/a)[b]
Corrigan and Novakov (1999)			0.225 (n/a)[b,d]

[a]average and standard deviation calculated using supplementary raw data corrected with ρ_{eff} when available
[b]uncertainty evaluated from spread in critical d_p using T=298 K and σ_w=0.072 J m^{-2}
[c]calculated for the pure metastable adipic acid data point; Petters and Kreidenweis (2007)
[d]averaged of data reported at multiple supersaturations
[e]standard deviation calculated from spread in the data; Petters and Kreidenweis (2007)

4.5 CONCLUSIONS

A thermodenuder with active temperature control has been constructed and characterized for steady temperature profiles and particle transmission efficiency. The system is characterized by the measured response of pure component organic aerosol with volatility spanning roughly 7 orders of magnitude in vapor pressure and is integrated with a comprehensive model that combines a computational fluid, mass, and heat transfer module integrated with a gas-phase module, within an optimization framework to infer thermo-kinetic parameters of the denuded aerosol. For each volatile compound, particle size decreases as temperature increases. Measured aerosol hygroscopicity, as expected, is consistent for each pure compound at different sizes and temperatures.

The presence of three potential size modes exiting the thermodenuder due to non-volatile material in the aerosol, the dominant size-selected aerosol, and the presence of multiply charged particles, respectively, is carefully considered in the analysis. Non-volatile material in the aerosol sample impact volatilization profiles for highly volatilized particles, leaving a small residual particle of ~10 to 30 nm. This can be explained by the level of impurities found in chemical compounds and water used to atomize the aerosol particles. These residuals are shown to have no impact on the measured hygroscopicity, though caution should be taken to investigate the impacts of impurities on measured properties in all relevant laboratory studies involving atomization of “pure” compounds. Size modes due to non-volatile material and multiply charged particles are deconvolved and not considered in the analysis.

In general, the volatility parameters retrieved in this study compare well with the literature. Adjusting the accommodation coefficient to reported values for succinic and

adipic acids results in the retrieval of volatility parameters that are in agreement with literature values. This suggests that the same response of aerosol within the thermodenuder can result in estimates of thermodynamic parameters that vary over orders of magnitude depending on the assumptions regarding the evaporation kinetics.

Future work will focus on determining volatility-hygroscopicity distributions using multi-component laboratory measurements and further augmenting the model with a full implementation of the volatility basis set approach. An adaptive measurement technique based on a simplified kinetic model from one of several approaches in the literature that can check the extent of the size change in real time and adjust selected sizes and temperature set points according to the anticipated volatility would further reduce biases in the retrieved volatility parameters. Avoiding the re-equilibration of the charge distribution at the second DMA would allow for a simpler analysis of the measured SMPS distributions (Rader and McMurry, 1986), since changes in the mobility distribution would be constrained to changes in their physical size alone. Finally, an important affirmation of the modeling framework and instrument data analysis would be to relate vapor pressure changes with a particle phase changes measured with another technique (e.g., Virtanen et al., 2010). This would require the kinetic parameter to be constrained independently and may be challenged by the effects of chemical impurities, but it is possible, provided ample control of experimental conditions and complimentary modeling of the physical system.

The use of low thermodenuder temperatures and small aerosol sizes are strong advantages as it ensures sensitivity to small amounts of volatilized aerosol and avoids excessive chemical transformation of the sample from heating. Together with the

comprehensive model and its demonstrated performance, the work presented here is a powerful tool for volatility/hygroscopicity studies at atmospherically-relevant mass loadings.

CHAPTER 5

CHAMBER STUDY AGING OF SECONDARY ORGANIC AEROSOL FROM AROMATIC VOCS: A CASE STUDY ON AEROSOL HYGROSCOPICITY AND OXIDATION[1]

5.1 INTRODUCTION

It is well known that secondary organic aerosol (SOA), compounds formed from oxidation of gas-phase precursors that partition to the particle phase, greatly impact the organic aerosol budget. As SOA are estimated to account for approximately 70% of total aerosol organic carbon mass (Hallquist et al., 2009), the implications of this on aerosol composition and related aerosol properties are important and complex (e.g., Kanakidou et al, 2005; Kroll and Seinfeld, 2008; Donahue et al., 2009). In order to address some of these complexities, environmental chamber studies are often used to probe important atmospheric phenomena under a range of atmospherically relevant conditions by varying oxidation conditions and precursors as well as a number of other parameters. As a result, these chamber studies of secondary organic aerosol (SOA) from the oxidation of volatile organic compounds (VOCs) and from processing of primary organic aerosol (POA) have become important in better understanding aerosol processing and their resulting composition and properties (e.g., Kroll and Seinfeld, 2008).

The hygroscopicity parameter, κ, is commonly used to express the solute impacts of an aerosol on its equilibrium vapor pressure. The relationship between organic aerosol hygroscopicity and oxidation level, indicated by the ratio of oxygen to carbon (O:C), has been the focus of a number of lab and field studies (e.g., Jimenez et al., 2009; Massoli et

[1]This chapter was conducted as part of a larger study conducted at Carnegie Mellon University and will be submitted to Atmospheric Chemistry and Physics for publication as: Hildebrandt Ruiz, L., Paciga, A., Cerully, K., Nenes, A., Donahue, N. M., and Pandis, S. N.: Aging of secondary organic aerosol from small aromatic VOCs: Changes in chemical composition, mass yield, volatility, and hygroscopicity.

al., 2010; Chang et al., 2010; Frosch et al., 2011; Lambe et al., 2011; Lathem et al., 2013; Alfarra et al., 2013). The prevailing view is that organic aerosol hygroscopicity increases with O:C, although other studies have found weak or no correlation between the two properties (e.g., Massoli et al., 2010; Frosch et al., 2011; Lathem et al., 2013; Alfarra et al., 2013). Jimenez et al. (2009) presented the results of several studies, both ambient and laboratory, showing the correlation of increasing hygroscopicity with O:C. Chang et al. (2010) and Lambe et al. (2011) showed this positive correlation for ambient data from a rural site in Ontario, Canada, and for a number of atmospherically-relevant precursors in chamber experiments, respectively. Lathem et al. (2013) found invariant organic κ under varied O:C conditions for a biomass burning influenced air masses during ARCTAS and ARCPAC. κ was largely independent of O:C in chamber experiments with α-pinene by Frosch et al. (2011). Several studies have investigated possible explanations for why hygroscopicity changes may be seen regardless of changes in the measured bulk O:C. It has also been shown that average carbon oxidation state, $\overline{\mathrm{OS}}_{\mathrm{C}}$, is likely a better indicator of aerosol oxidation than O:C as O:C may not reflect oxidative changes due to the breaking and formation of bonds and can be impacted non-oxidative processes such as hydration and dehydration while $\overline{\mathrm{OS}}_{\mathrm{C}}$ increases continually with oxidation (Kroll et al., 2009a; 2011); thus, O:C may not be as well correlated with observed hygroscopicity. Part of the discrepancy may be related to the nature of hygroscopicity measurement itself; some studies use subsaturated measurements of HTDMA-derived hygroscopicity (e.g., Jimenez et al., 2009; Massoli et al., 2010; Alfarra et al., 2013), while others investigate supersaturated measurements of CCN-derived hygroscopicity (e.g., Chang et al., 2010; Massoli et al., 2010; Lambe et al., 2011; Frosch et al., 2011; Lathem et al., 2013; Alfarra

et al., 2013). The large difference of water volume per aerosol mass involved in each measurement (subsaturated versus supersaturated conditions) affects the species that can dissolve and the interactions of water, as reflected by the different values of hygroscopicity obtained by both techniques (e.g., Wex et al., 2009; Petters et al., 2009b). Another reason however is related to the presence of surfactants. Under supersaturated conditions, critical supersaturation (hence the hygroscopicity parameter) is affected by changes in surface tension considerably more than for subsaturated conditions (Ruehl et al., 2010). A large body of research (Shulman et al., 1996; Facchini et al., 1999, 2000; Topping et al., 2007; Padró et al., 2007, 2010; Asa-Awuku et al., 2008; Engelhart et al., 2008; King et al., 2009; Schwier et al., 2011; Li et al., 2011; Ruehl et al., 2012) suggests that surface tension from dissolved solute in the aerosol can vary by about 10% at the point of activation. These soluble compounds can either preexist in the dry aerosol or form from dissolution of compounds, like methylglyoxal, from the gas-phase (e.g., Sareen et al., 2010; Li et al., 2011; Lim et al., 2013). Recently, gas-phase compounds have also been suggested to adsorb directly on the droplet-air interface and affect surface tension, increasing the apparent hygroscopicity of inorganic seed aerosol (Sareen et al., 2013).

The relationship of increased aerosol hygroscopicity with increased oxidation has been proposed to be further linked with decreased aerosol volatility (Jimenez et al., 2009). While few chamber studies have investigated the link between all three properties combined (e.g., Poulain et al., 2010; Tritscher et al., 2011), several additional studies have shown that the relationship between volatility and hygroscopicity may not be as straightforward (Meyer et al., 2009; Asa-Awuku et al., 2009; Tang et al., 2012). These

studies encompass both subsaturated (Meyer et al., 2009; Tritscher et al., 2011) and supersaturated (Asa-Awuku et al., 2009; Poulain et al., 2010; Tang et al., 2012). Asa-Awuku et al. (2009) and Tang et al. (2012) saw that in chamber experiments of β-caryophyllene the most volatile fraction was also the most hygroscopic. In chamber studies of α-pinene SOA, Meyer et al. (2009) also measured a decrease in hygroscopicity with increased volatility. Poulain et al. (2010) found for α-pinene SOA that the most volatile components were the most hygroscopic, in agreement with Asa-Awuku et al. (2009), Tang et al. (20012), and Meyer et al. (2009), though contradictory to the conventional view that the most volatile components should be the least hygroscopic. Additionally, Poulain et al. (2009) found that the most oxygenated aerosol showed lower volatility than the less oxygenated aerosol, in agreement with the conventional view. Tritscher et al. (2011) found that hygroscopicity and O:C remained constant with decreased volatility for α-pinene SOA. The following study investigates the relationship between supersaturated hygroscopicity, volatility, and oxidation of SOA formed from a variety of toluene photo-oxidation conditions.

5.2 METHODOLOGY

5.2.1 Experimental Setup

Organic aerosol was formed from photo-oxidation of toluene and other small aromatic VOCs in the Carnegie Mellon Center for Atmospheric Particle Studies (CAPS) environmental chamber. The experimental approach was to fill the chamber with clean air, inject the VOC and nitrous acid (HONO), and turn on the UV lights to start formation of OH (from the photolysis of HONO), oxidation of the VOC and formation of SOA. The amount of SOA formed, the SOA oxidation state, its thermal volatility, and its

hygroscopicity were then measured, though this study will focus on the impacts of oxidative ageing on hygroscopicity. Details of each of the chamber experiment conditions are summarized in Table 5.1

Table 5.1: Summary of experimental conditions in the CAPS environmental chamber.

Expt. #	$(NH_4)_2SO_4$ Seeds	$[Toluene]_0$[a]	HONO injections	Lights (%)	[OH] exposure (cm^{-3} s)[b]	Additional compounds added
1	No	~ 200 ppb	2	100	--	
2	Yes	~ 100 ppb	2+1	100	--	
3	No	~ 100 ppb	2	100	--	o-xylene, trimethylbenzene, benzene (~ 100 ppb each[b])
4	Yes	~ 100 ppb	1	100	$10x10^{10}$	p-xylene, ethylbenzene (~100 ppb each [b])
5	Yes	~ 100 ppb	3+3	100	$24x10^{10}$	

[a] VOC concentration estimated based on volume of VOC injected
[b] Total [OH] exposure over the course of the experiment, estimated from exponential fits to the decay of toluene. Data not available for experiments 1-3 due to lack of PTR-MS data.

Nitrous acid was produced immediately before injection by drop-wise addition of 12 ml 0.10M sodium nitrite solution to 24 ml 0.05M sulfuric acid solution. Ammonium sulfate ($(NH_4)_2SO_4$, Sigma Aldrich, 99.99%)) seed particles were used in some experiments (Table 5.1) to provide surface area onto which semi-volatile organics would condense. In the unseeded experiments, nucleation of the organic vapors was observed. Concentrations of the VOCs were monitored using a proton-transfer reaction mass spectrometer (PTR-MS, Ionicon Analytik GmbH) when available. PTR-MS measurements of toluene were corrected for ion-source intensity and humidity as suggested by de Gouw et al. (2003), and the PTR-MS was calibrated before each experiment.

Figure 5.1 presents the experimental setup. Particle number and volume of the chamber aerosol were measured using a scanning mobility particle sizer (SMPS, TSI model 3080 classifier and TSI model 3772 condensation particle counter (CPC)). Particle mass and chemical composition was measured using a high-resolution time-of-flight aerosol mass spectrometer (HR-ToF-AMS, referred to hereafter as AMS, Aerodyne, Inc.; DeCarlo et al., 2006) which measures concentrations of all non-refractory species (i.e., species that volatilize rapidly at 600°C). The AMS was operated in both mass spectrum mode, with higher resolution but lower sensitivity, and particle time-of-flight mode which has higher sensitivity but lower resolution.

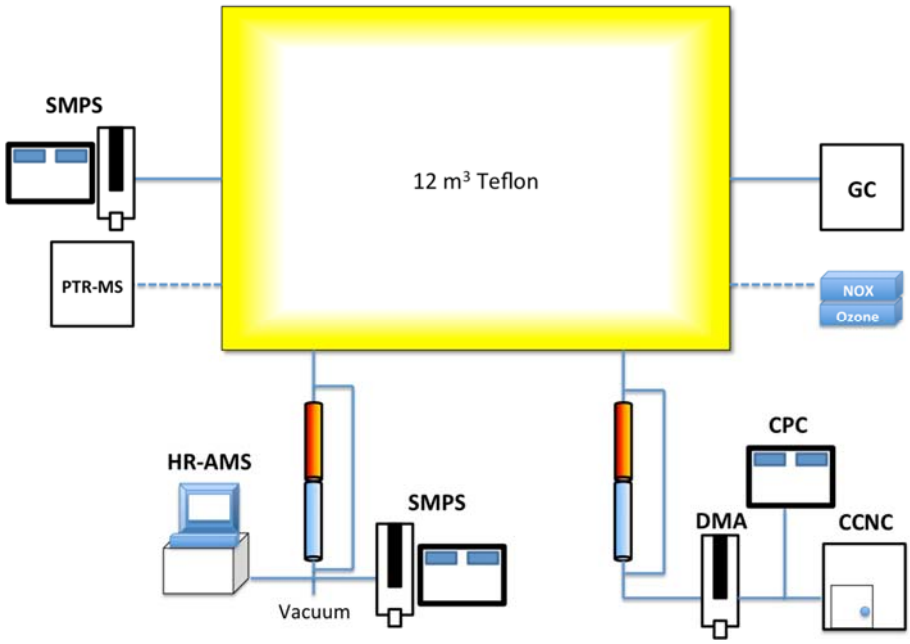

Figure 5.1: Schematic of experimental setup. Dotted lines indicate that the equipment was used when available.

Two thermodenuder (TD) systems were used and operated at the same temperature (switching between approximately 60, 80, and 100°C). Air from the chamber was split into two separate streams. In the first stream, OA volatility was measured using a TD system similar to that of Lee et al. (2010) in which particles passing through the TD are

heated to a predefined temperature and then SMPS and the AMS measure the particle size distributions and chemical composition, respectively. Properties of thermally-treated aerosol are compared against those measured by a bypass line at ambient temperature. The standard operating sample flow rate for the TD was 1 liter per minute (L min^{-1}), corresponding to a centerline residence time of ~15 s. In the TD followed by the AMS, the flow rate was also sometimes set to 0.6 L min^{-1}, corresponding to a centerline residence time of ~25 s, to evaluate the effects of a longer residence time on OA evaporation, though this data was not used for thermally-denuded CCN comparisons. In the second stream, aerosol was again passed alternately through the TD or bypass line, then size-selected (approximately 100 to 140 nm) using a differential mobility analyzer (DMA; TSI model 3080) operated with a sheath to aerosol ratio of 5:1. Aerosol flow was split to a CPC (TSI model 3010) and a cloud condensation nuclei counter (CCNc, Droplet Measurement Technologies; Roberts and Nenes, 2005; Lance et al., 2006) operated in Scanning Flow CCN Analysis (SFCA) mode (Moore and Nenes, 2009). SFCA permits fast CCN measurements of OA hygroscopicity. Dilution air of 1.1 L min^{-1} was introduced after the DMA before splitting to the CCNc and CPC. Flow to the CCNc was held constant at 1.1 L min^{-1} using a laminar flow element, while flow in the CCNc was linearly ramped between 0.1 and 0.9 L min^{-1} over 60 s. The top to bottom column temperature was 6°C for all experiments.

5.2.2 Data Analysis

5.2.2.1 CCNc Calibration

The CCNc instrument calibration is used to determine the relationship between instantaneous instrument flow rate and supersaturation as described in Moore and Nenes

(2009). Ammonium sulfate solution is atomized, dried using a silica gel diffusion dryer, charge-neutralized using Po-210, and classified by a DMA. The flow is then introduced into both a CPC and a CCNc. The activation ratio, or the ratio of CCN to total particles, is then plotted against the instantaneous flow rate to yield data that are fit to a sigmoidal activation ratio function. The critical flow rate, Q^*, is determined, corresponding to where half of the total particles are activated and to a level of supersaturation, s^*, equal to the critical supersaturation of the classified aerosol (Section 5.2.2.2). The Q^* and s^* are determined for a range of aerosol sizes, yielding, for the flow rate range (0.1-0.9 L min^{-1}) and temperature gradient (ΔT=6°C) in the CCNc column, supersaturations ranging from approximately 0.10 to 0.50%.

5.2.2.2 Determining Aerosol Hygroscopicity

Using the method outline in the previous section, s^* was determined for each flow rate upscan and downscan (though only upscan data were used in this study). All CCNc data were filtered for poor counting statistics by removing all activation spectra where the maximum CCN concentrations were lower than approximately 15 to 20 counts cm^{-3} (Moore et al., 2010). The characteristic hygroscopicity parameter, κ (Petters and Kreidenweis, 2007), of the monodisperse CCN is then determined by

$$\kappa = \frac{4A^3}{27 d_p^3 s^{*2}} \tag{5.1}$$

where $A=(4M_w\sigma_w)/(RT\rho_w)$; M_w, σ_w, and ρ_w are the molar mass, surface tension, and density of water, respectively. R is the universal gas constant, T is CCNc mid-column temperature, and d_p is the dry particle diameter selected by the DMA prior to the CCNc.

In the case of $(NH_4)_2SO_4$ seeded experiments (see Table 5.1), the measured κ will have a contribution from the organic components (*org*) as well as the inorganic seeds (*inorg*). These contributions can be described by

$$\kappa = \sum_j \kappa_j \varepsilon_j = \kappa_{org}\varepsilon_{org} + \kappa_{inorg}\varepsilon_{inorg} \quad (5.2)$$

where κ_j and ε_j are the hygroscopicity and volume fraction of each component, j. Size-resolved AMS fractions are used to determine ε_{org} and ε_{inorg}; however, κ_{org} could not be determined for the seeded experiments due to low mass loadings on the same order or magnitude as the AMS uncertainty. In the case of unseeded experiments, κ is equal to κ_{org} for both thermodenuded and non-denuded measurements.

5.2.2.3 AMS Analysis

All AMS data were corrected for depositional loss of particles onto the chamber walls, and for the condensational loss of organic vapors to wall-deposited particles. Additionally, the O:C ratios calculated here differ slightly from that of standard O:C calculations. In these experiments, no inorganic nitrate is introduced or anticipated. Hence the ions assigned to the nitrate family (NO^+, NO_2^+) are presumed to originate from organic nitrates and were added to the total organic aerosol mass. The relative ionization efficiency (RIE) of 1.0 is used to quantify the contribution from these fragments. The elemental analysis examines the oxidation state of the carbon atoms; hence, nitrate fragments (NO^+, NO_2^+) were not included in the calculation of O:C. This results in a higher represented O:C value (e.g., 0.90 presented here would be roughly in the range of 0.5 to 0.6 when using the standard O:C method). $\overline{OS}_C$ is then calculated as 2*O:C-H:C where H:C is the hydrogen to carbon ratio as in Kroll et al. (2011).

5.3 RESULTS

CCNc-derived organic hygroscopicity, κ_{org}, expressed as the average hygroscopicity of all measured sizes, versus the bulk O:C ratio and $\overline{OS}_C$ for each experiment is shown in Figure 5.2. Throughout all experiments, κ_{org} ranges between from 0.10 to 0.25 while bulk O:C ranges from approximately 0.85 to 1.05. For each experiment, after the initial period of photo-oxidation, κ_{org} remains fairly constant as does O:C. There is no clear correlation between κ_{org} and O:C across all experimental condition (Figure 5.2 top, left), consistent with the relationship between κ_{org} and $\overline{OS}_C$ (Figure 5.2 top, right). These results are against the conventional view that oxidative ageing of aerosol generally increases its hygroscopicity (e.g., Jimenez et al., 2009).

When investigating κ_{org} for experiments 1 and 3 where both non-denuded and thermally-denuded measurements were collected, it appears that thermally-denuded aerosol (combined measurements from 60, 80, and 100°C) may show a slightly decrease in κ_{org} with increased O:C (and $\overline{OS}_C$) (Figure 5.2 bottom), against the conventional idea that the less volatile aerosol is more hygroscopic as was also seen by Asa-Awuku et al. (2009), Meyer et al. (2009), Poulain et al. (2010), and Tang et al. (2012). This is, however, in agreement with the idea that the less volatile aerosol is the most oxidized as was also seen by Poulain et al. (2010). While the change in κ_{org} as well as O:C and $\overline{OS}_C$ cannot be concluded with confidence due to the relatively large variation in κ_{org}, it is possible that this relationship between hygroscopicity, oxidation, and volatility suggests that there may be another process, aside from bulk oxidation changes, causing changes in the measured hygroscopicity.

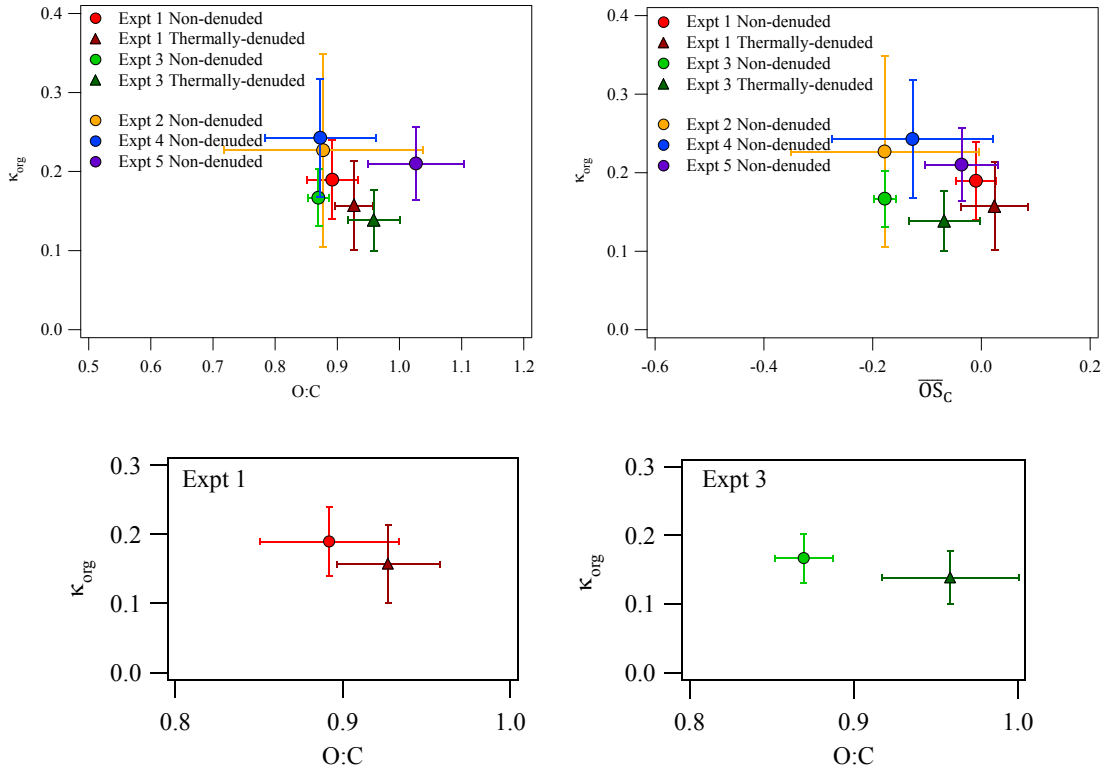

Figure 5.2: κ_{org} versus O:C (top, left) and $\overline{OS}_C$ (top, right) for all experiments as listed in Table 5.1. Also shown are magnified hygroscopicity and O:C for unseeded experiments with non-denuded and thermally-denuded measurements (bottom). Vertical and horizontal error bars represent the standard deviation in κ_{org} and O:C or $\overline{OS}_C$, respectively.

Sareen et al. (2013) showed that gas-phase compounds such as methylglyoxal can act as surfactants which depress surface tension and enhance CCN-activity (and hygroscopicity). As methylglyoxal as well as other gas-phase surface-active compounds such as benzaldehyde and glyoxal are known products of toluene oxidation by OH (e.g., Hu et al., 2007; Baltaretu et al., 2009; Hamilton et al., 2005; White et al., 2014), it is likely that gas-phase surfactants are present here. If surfactant films are present on the non-denuded aerosol, enhancing their hygroscopicity, then desorption of the surfactants later upon heating may increase surface tension and depress apparent hygroscopicity. A monolayer of surfactant adsorbed from the gas phase would induce a negligible impact

on bulk O:C or $\overline{OS}_C$, thus it is expected, as seen here, that the least volatile aerosol is the most oxidized. Altogether, this means that the proposed relationship of increased hygroscopicity and oxidation with decreased volatility may still hold in terms of the organic compounds in the aerosol, while surfactants may noticeably modulate apparent aerosol hygroscopicity.

5.4 CONCLUSIONS

Organic aerosol were formed by the photo-oxidation of toluene as well as mixtures of toluene with o-xylene, trimethylbenzene, and benzene, and with p-xylene and ethylbenzene under different oxidizing conditions and in the presence of NO_x. Approximately half of the total OA mass was attributed to organic nitrates, emphasizing the importance of these species in SOA formation under high NO_x conditions. CCN activity shows that for all experiments, during both thermally-denuded and non-denuded periods, κ_{org} ranges from approximately 0.10 to 0.25 with minimal changes in O:C and $\overline{OS}_C$ ranging from approximately 0.85 to 1.05 and -0.2 to 0.0, respectively. For all experiments, there is no clear correlation between κ_{org} and O:C or $\overline{OS}_C$. Comparison of thermally-denuded and non-denuded measurements showed a tendency for the mean κ_{org} to decrease upon heating in the thermal denuder while O:C increased. While thermally-denuded κ_{org} values are within a standard deviation of the non-denuded κ_{org}, this shift may be real, being a result of hygroscopic low volatility material leaving the aerosol upon heating in the denuder. The shift may also be a result of surface active compounds from the gas phase (such as methylglyoxal, a known product of toluene photo-oxidation, or other aromatic aldehydes that are known to exist in the gas phase) influencing surface tension, CCN-activity and apparent hygroscopicity. When adsorbed onto the aerosol, gas-

phase molecules would depress surface tension and elevate the hygroscopicity compared to the bulk material in the aerosol. The same molecules would tend to desorb from the aerosol upon heating in the thermal denuder, increase surface tension and decrease the apparent hygroscopicity (compared to the non-denuded aerosol). Although occurring from heating in the denuder, desorption of gas-phase molecules would also occur in the atmosphere upon dilution or changes in ambient temperature, resulting in a greater apparent hygroscopicity of the lesser volatile aerosol components. More experiments are needed which explore a greater range of oxidative conditions. Additionally, chamber experiments probing the effects of dilution on aerosol volatility with hygroscopicity may give insight into the relevance of surfactant-impacted hygroscopicity changes and the relationship between oxidation, hygroscopicity, and volatility.

CHAPTER 6

INVESTIGATION OF THE POTENTIAL LINK BETWEEN HYGROSCOPICITY, VOLATILITY, AND OXIDATION OF AMBIENT AND WATER-SOLUBLE AEROSOL IN THE SOUTHEASTERN UNITED STATES

6.1 INTRODUCTION

Aerosol are well known to be important drivers of climate from regional to global scales by scattering and absorbing radiation as well as acting as cloud condensation nuclei (IPCC, 2007). Though much progress has been made in specifically understanding the role of organic aerosol in the climate system, the formation of secondary organic aerosol (SOA) and the partitioning of semi-volatile organics is one topic that requires further study (e.g., Kanakidou et al., 2005; Goldstein and Galbally, 2007; Kroll and Seinfeld, 2008; Donahue et al., 2009; Hallquist et al., 2009; Ervens et al., 2011). Recent studies show that different estimation methods of SOA production result in ranges from 140 to 910 Tg C/yr (Goldstein and Galbally, 2007). The large uncertainty in these estimates (e.g., Pye and Seinfeld, 2010; Hallquist et al., 2009; Jimenez et al., 2009; Kanakidou et al., 2005) illustrates the need for better understanding of organic aerosol composition, volatility, hygroscopicity, and CCN activity.

Few studies have investigated the link between aerosol hygroscopicity, volatility, and level of aerosol oxidation (e.g., Jimenez et al., 2009; Poulain et al., 2010; Tritscher et al., 2011; Hong et al., 2013), though many have looked at links between only two of these parameters (e.g., Kuwata et al., 2007; Asa-Awuku et al., 2009; Meyer et al., 2009;

[1]This chapter contains work to be submitted for publication as: Cerully, K., Bougiatioti, A., Lu, X., Hite Jr., J. R., Guo, H., Ng, N. L., Weber, R., and Nenes, A.: Investigation of the Potential Link Between Hygroscopicity, Volatility, and Oxidation of Ambient and Water-soluble Aerosol in the Southeastern United States.

Massoli et al., 2010; Chang et al., 2010; Lambe et al., 2011; Lathem et al., 2013; Frosch et al., 2011, 2013; Villani et al., 2013). Several studies have shown and proposed parameterizations for the relationship between increasing organic hygroscopicity and oxidation (Chang et al., 2010; Massoli et al., 2010; Lambe et al., 2011; Frosch et al., 2013), with hygroscopicity being represented by growth factor (GF) derived from subsaturated measurements or the hygroscopicity parameter, κ, derived from supersaturated measurements (Petters and Kreidenweis, 2007), and oxidation represented by the oxygen to carbon ratio (O:C) or f_{44}, the ratio of the m/z 44 peak to the total signal in an aerosol mass spectrometer (AMS) (Ng et al., 2010; Aiken et al., 2008). Jimenez et al. (2009) showed results of several studies correlating GF with O:C and proposed a 2-dimensional framework for organic aerosol where hygroscopicity and oxidation level increase with decreased volatility. There are several other studies, though, that have shown that the link between two or all of properties is not always straightforward (e.g., Meyer et al., 2009; Poulain et al., 2010; Frosch et al., 2011; Tritscher et al., 2011; Lathem et al., 2013, Alfarra et al., 2013; Villani et al., 2013). Frosch et al. (2011) saw weak sensitivity of supersaturated κ to O:C and f_{44}, respectively and Alfarra et al. (2013) saw weak correlation for both subsaturated and supersaturated hygroscopicity measurements with f_{44} in laboratory studies of α-pinene SOA. Tritscher et al. (2011) found in chamber studies of α-pinene SOA that volatility generally decreased while subsaturated hygroscopicity and O:C remained fairly constant, and an additional study of α-pinene SOA by Meyer et al. (2009) measured a decrease in subsaturated hygroscopicity with increased volatility. Lathem et al. (2013) found that for biomass burning aerosol sampled during the ARCTAS and ARCPAC field campaigns, supersaturated organic

hygroscopicity increased while O:C remained fairly constant. In ambient measurements by Villani et al. (2013), it was observed that subsaturated hygroscopicity in several externally mixed air masses could increase or decrease after volatilization. Kuwata et al. (2007) found for subsaturated measurements of ambient particle in Tokyo that, after briefly heating to 400°C, a less hygroscopic particle mode was also less volatile while a more hygroscopic particle mode was more volatile. The results of these studies illustrate the range in possible relationships between hygroscopicity, volatility, and oxidation level, and the need to better understand why and when these linkages occur. An additional level of complexity arises in interpreting these results as subsaturated GF and supersaturated κ measurements can differ due to the difference in water volume between measurement conditions, thus impacting the assumption of an ideal solution and the importance of surface tension effects (Wex et al., 2009; Petters et al., 2009b; Ruehl et al., 2010). Furthermore, recent studies have shown that average carbon oxidation state, $\overline{\mathrm{OS}}_{\mathrm{c}}$, may be a better indicator of aerosol oxidation than O:C as O:C may not capture oxidative changes due to the breaking and forming of bonds (Kroll et al., 2009a; 2011). Also important to SOA formation and processing are aqueous phase aerosol. Aqueous particles can both absorb species from the gas phase and serve as a medium for aqueous SOA production (Zuend and Seinfeld, 2012; Ervens et al., 2011; Ervens et al., 2013). Hennigan et al. (2009) found that water-soluble organic carbon included a major portion of SOA in Atlanta. Aqueous SOA and its partitioning, predicted to be different than that of SOA in the gas phase (Ervens et al., 2011) will also have important impacts on aerosol volatility and hygroscopicity. It has been proposed that SOA produced in the aqueous phase may have higher κ than SOA formed in the gas-phase with an upper limit comparable to

ammonium sulfate (κ = 0.6) (Ervens et al., 2011), though few experiments have investigated the impact of SOA aqueous phase processes on total κ in ambient aerosol.

Atmospheric measurements are important for investigating the previously described aerosol complexities. In particular, the southeastern United States presents itself as a particularly interesting location of study. This region of the US has shown an overall cooling trend, in contrast to the warming trend typically seen throughout the US (Goldstein et al., 2009; Portmann et al., 2009). Goldstein et al. (2009) showed that the aerosol optical thickness, responsible for the dominant cooling in the summertime, likely resulted from SOA from biogenic volatile organic compounds (BVOC) reacting with anthropogenic pollution. Carlton and Turpin (2013) found that aqueous SOA formation is particularly important in the eastern United States (Carlton and Turpin 2013). These findings show that the SOA processes happening in this region are most definitely complex and important. The Southern Aerosol and Oxidant Study (SOAS) was a collaborative field mission which aimed to study the previously discussed issues. This study focuses on ambient aerosol and the water-soluble fraction of ambient aerosol collected at a SOAS field site in rural Alabama and uses a variety of aerosol instrumentation to probe aerosol composition, volatility, and CCN properties.

6.2. DATA COLLECTION

6.2.1 Measurement Site

Data were collected during the Southern Oxidant and Aerosol Study (SOAS), part of the Southeast Atmosphere Study (SAS) (http://www.eol.ucar.edu/projects/sas), in Centreville, Alabama (+32° 54' 11.81", -87° 14' 59.79"), a highly biogenic site with varying levels of anthropogenic influence (Carlton et al., n.d.). Measurements were taken

from June 1 through July 15, 2013 using a suite of aerosol instrumentation, including a Droplet Measurement Technologies Continuous-Flow Streamwise Thermal Gradient CCN counter (CFSTGC, referred to hereafter as the CCNc; Roberts and Nenes, 2005; Lance et al., 2006), thermodenuder (TD; Cerully et al., 2013), Particle-Into-Liquid-Sampler (PILS; Weber et al., 2001; Orsini et al., 2003), and high resolution time-of-flight aerosol mass spectrometer (HR-ToF-AMS, referred to hereafter as AMS; DeCarlo et al., 2006) to gain information of CCN activity and hygroscopicity, volatility, water-soluble aerosol components, and aerosol composition and oxidation, respectively. This paper will primarily focus on comparing non-denuded and thermally-denuded measurements in order to investigate any linkages between hygroscopicity, volatility, and oxidation for both ambient and water-soluble ambient $PM_{1.0}$ aerosol.

6.2.2 Experimental Setup and Data Collection

The instrument setup is shown in Figure 6.1. Aerosol were collected using a $PM_{1.0}$ cyclone and either sampled directly from ambient or passed through the PILS. For ambient sampling, aerosol were dried using a Nafion dryer and charge-neutralized using a Po-210 bipolar charging source. For PILS sampling, aerosol were collected directly from ambient before being dried, thus any aqueous phase material in the ambient aerosol is also captured by the PILS. The PILS liquid is then nebulized, dried with a Nafion dryer, and charge-neutralized. The polydisperse aerosol stream then passed through the TD or through a bypass line before being split to the AMS, Scanning Mobility Particle Sizer (SMPS; TSI classifier model 3080, CPC model 3022), and CCNc. The CCNc was operated in Scanning Flow CCN Analysis (SFCA) mode (Moore and Nenes, 2009), scanning flow rate sinusoidally from 0.2 to 0.9 L min^{-1} then back to 0.2 L min^{-1} over 2

minutes, resulting in a CCN spectrum between 0.10% and 0.40% supersaturation, *s* (see Section 6.3.1). The flow entering the CCNc was held constant at 1 L min^{-1} using a laminar flow box and introduced to the CCN column as needed. The sheath to aerosol ratio in the CCNc was approximately 10:1. The top-to-bottom temperature difference in the CCN instrument was 6°C. Temperature in the TD heating section was switched between 60, 80, or 100°C. In this setup, the TD was operated without a cooling section, though recondensation of vapors is minimal at low ambient mass loadings (e.g., Cerully et al., 2013; Saleh et al., 2011). The classifier was operated with a sheath flow rate of 3.0 L min^{-1} and aerosol flow rate of 0.30 L min^{-1} (10:1 ratio), controlled by the CPC 3022 in low flow mode. Aerosol size distributions were collected every 3 minutes, scanning particle sizes from 14.6 to 685.4 nm. The AMS was operated in V mode (DeCarlo et al., 2006) with a data averaging time of 3 minutes. AMS measures mass concentrations of non-sea salt chloride, sulfate, nitrate, ammonium, and organics while non-refractory species (at 600°C), including sea-salt, black carbon, and crustal material, are not detected. Separate from this setup was an additional PILS coupled with an ion chromatograph (IC), referred to hereafter as the PILS-IC, which measures the ambient water-soluble Na^+, NH_4^+, K^+, Ca^{2+}, Mg^{2+}, Cl^-, NO_3^-, NO_2^-, SO_4^{2-} as well as acetate, formate, and oxalate every 20 minutes (Orsini et al., 2003).

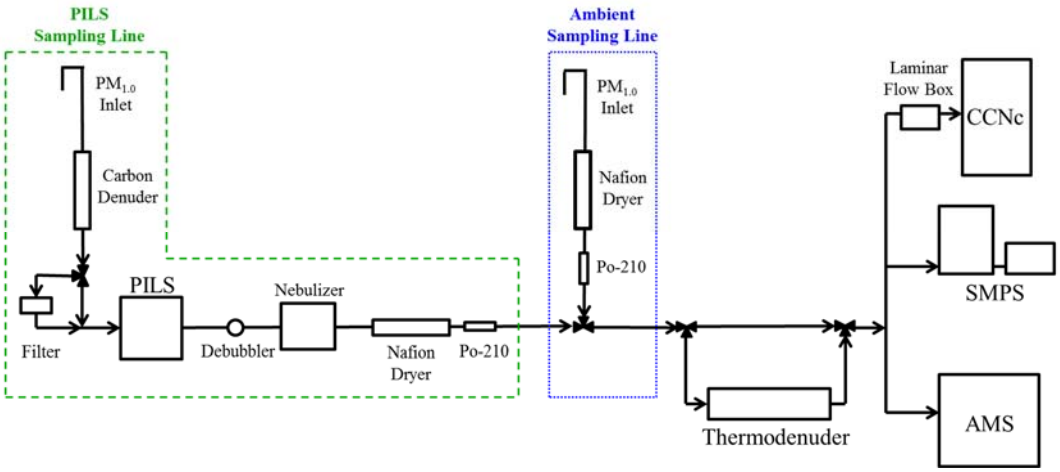

Figure 6.1: Instrument setup combining a PILS, thermodenuder, CCNc, and AMS to measure the water-soluble fraction of ambient aerosol (green dashed line) and ambient aerosol (blue dotted line).

The sampling schedule shown in Figure 6.2 was designed to allow for automated measurements of ambient and water-soluble ambient aerosol. Thermodenuded measurements were conducted June 20 to July 15. The temperature in the TD heating section was switched between 60 and 80°C from June 20 to midday June 30 (Figure 6.2, solid red line) and between 60 and 100°C from evening June 30 through July 15 (Figure 6.2, dashed line). The sampling schedule and instrument setup were changed slightly from July 7 to 9, though this only impacted the length between sampling intervals and for that reason is not show in Figure 6.2.

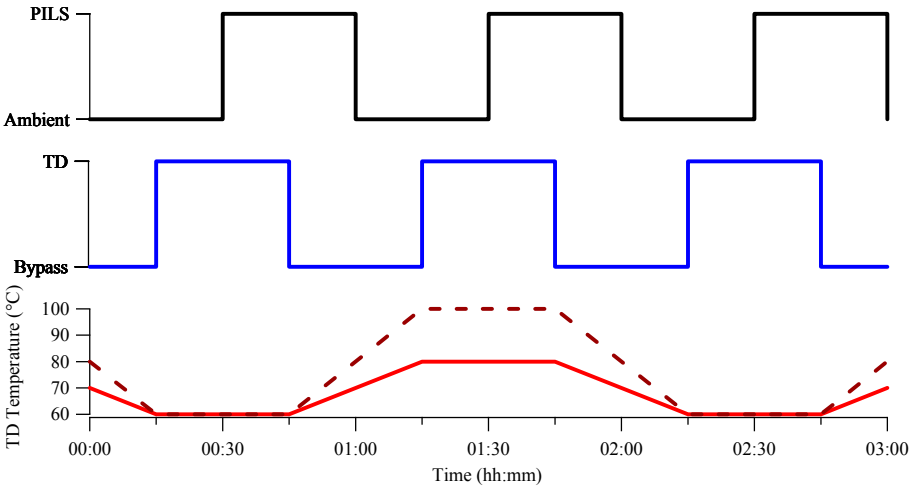

Figure 6.2: Example sampling schedule illustrating the valve switching between both PILS and ambient sampling lines and TD and bypass sampling lines. TD sampling temperatures from June 20 to midday June 30 are indicated by the red, solid line, and sampling temperatures from evening June 30 to July 15 are indicated by the dashed line.

SMPS distributions and AMS measurements sampled directly before or after each valve switch (i.e., between ambient and PILS or between bypass and TD) were eliminated, leaving 3 SMPS scans and AMS samples per 15 minute measurement interval. CCN properties (e.g., flow and CCN concentration) were averaged in cases where more than one scan occurred during a single SMPS sample. CCN spectra were smoothed by fitting CCN concentrations as a function of *s*. These fits were filtered for cases where flow rate fit parameter standard deviations are greater than 25 cm^3/min, resulting in a supersaturation uncertainty of approximately ± 0.03% (according to the calibration described in Section 6.3.1). The resulting CCN concentrations were compared with activation spectra predicted by applying Köhler theory to SMPS-measured concentrations under the assumption that the distributions had a κ of approximately 0.2-0.3, a general estimation of an aerosol population of organics and ammonium sulfate with equal volume fractions or slightly higher organic volume fraction

than ammonium sulfate (see Section 6.3.3), in order to filter for irregularities (e.g., unreasonable CCN concentrations, non-correlated activation slopes, size distributions effected by CPC flow inconsistencies). All measured supersaturation were corrected for supersaturation depletion (see Section 6.3.1). Data were further filtered for days with precipitation (data provided by Atmospheric Research & Analysis, Inc.) and for any measurement interruptions (e.g., truck deliveries to the sampling site). As flow, and therefore supersaturation, is scanned in the CCNc, spectra were divided into bins of s(%)±0.005% and averaged within each bin.

6.3. METHODOLOGY

6.3.1 Instrument Calibration and Supersaturation Depletion

The relationship between supersaturation and instantaneous flow rate was calibrated using the procedures of Moore and Nenes (2009). Briefly, ammonium sulfate solution is atomized, dried using two silica gel diffusion dryers and charge-neutralized using Po-210. The dried aerosol is then classified by a differential mobility analyzer (DMA; TSI model and split between a CPC, giving the total number of condensation nuclei (CN), and the CCNc. The activation ratio, or ratio of CCN to CN concentration, is plotted against instantaneous flow rate and fit to a sigmoidal function. The point where half of the total particles act as CCN corresponds to a critical flow rate. This flow rate corresponds to the known critical supersaturation, s_c, of the classified ammonium sulfate determined by Köhler Theory (Köhler, 1936). This relationship is determined for a range of classified ammonium sulfate particles, resulting in a calibration curve, in this case ranging from 0.10 to 0.40%, for the given flow rate range from 0.2 to 0.9 L min^{-1} and column top-to-bottom temperature gradient of 6°C.

The calibration method described above was conducted with ammonium sulfate aerosol concentrations below 700 cm^{-3} in order to avoid water vapor depletion in the instrument (Lathem and Nenes, 2011). For measurements made throughout the study, supersaturation depletion in the CCNc column was accounted for using the correction found in Raatikainen et al. (*in review*); this typically has a negligible effect when sampling low ambient number concentrations but can be important for sampling from the PILS-nebulizer system (Figure 6.1, green dashed line) where number concentrations can reach up to approximately 250,000 cm^{-3}.

6.3.2 Determining Total Aerosol Hygroscopicity

Aerosol activate in the CCNc when their critical supersaturation, s_c, is greater than the instantaneous supersaturation (i.e., flow rate), s, in the CCNc column. This s_c corresponds to a critical diameter, $d_{p,c}$. The $d_{p,c}$ is obtained by matching the concentration of CCN activated at a given s (where s=s_c) with the backwards integrated SMPS number distribution (thus, the corresponding size bin and $d_{p,c}$) (described in further detail in Moore et al., 2011). These parameters are used to determine the aerosol hygroscopicity parameter, κ (Petters and Kreidenweis, 2007)

$$\kappa = \frac{4A^3}{27 d_{p,c}^3 s_c^2} \tag{6.1}$$

where A=$(4M_w\sigma_w)/(RT\rho_w)$, and M_w, σ_w, and ρ_w are the molar mass, surface tension, and density, respectively, of water at the average mid-column temperature, T, in the CCNc (305 K). R is the universal gas constant. This analysis method operates under the assumption that activation kinetics are fast (i.e., that of a highly hygroscopic salt such as ammonium sulfate) and assuming that the aerosol are internally mixed. In cases where

ambient or thermodenuded measurements are inhomogeneous, κ is most representative of particles with sizes near $d_{p,c}$.

6.3.2.1 Uncertainty in Measured Hygroscopicity

The uncertainty in the measured κ can be mainly attributed to uncertainties in the measured particle diameter and instrument supersaturation and can be described by

$$\Delta(\kappa) = \sqrt{\left(\frac{\partial \kappa}{\partial s}\Delta s\right)^2 + \left(\frac{\partial \kappa}{\partial d_p}\Delta d_p\right)^2} \tag{6.2}$$

where Δs and Δd_p are the instrument uncertainties in CCNc-measured supersaturation and DMA-measured diameter, respectively. Absolute uncertainty from CCNc supersaturation is estimated at ±0.04% (Moore et al., 2011) while DMA sizing uncertainty, based on the width of the DMA transfer function (Wang and Flagan, 1990) and the 10:1 sheath to aerosol flow ratio used in this study, is approximately 10%. Average critical diameters of ambient aerosol 83, 95, and 116 nm measured at supersaturations of 0.40, 0.30, and 0.20%, respectively, are reported and discussed in Section 6.4. Applying these values to Equation (6.2) gives a $\Delta\kappa$ of 0.033, 0.053, and 0.097 for 0.40, 0.30, and 0.20% supersaturation, respectively.

6.3.3 Inferring Organic Aerosol Hygroscopicity

Total aerosol hygroscopicity can be described using a mixing rule

$$\kappa = \sum_j \varepsilon_j \kappa_j \tag{6.3}$$

where ε_j and κ_j are the volume fraction and hygroscopicity of species j, respectively (Petters and Kreidenweis, 2007). Using this rule, aerosol can be separated into its

organic, *org*, and inorganic, *inorg*, contributions to the total, measured hygroscopicity, where

$$\kappa = \varepsilon_{org}\kappa_{org} + \varepsilon_{inorg}\kappa_{inorg}. \quad (6.4)$$

Measurements of particle composition, in this case, can come from either AMS or PILS-IC measurements. Using the five ion concentrations measured by AMS, aerosol can be separated into its primarily inorganic ($[NH_4^+]$, $[SO_4^{2-}]$, $[Cl^-]$, and $[NO_3^-]$) and organic ([Org]) mass concentrations. A typical organic density of 1.4 g cm^{-3} is assumed for volume calculations (e.g., Moore et al., 2011; Lathem et al., 2013). In order to better assess the properties of the inorganic aerosol, the partitioning of aerosol between sulfate species is evaluated (Nenes et al., 1998; Moore et al., 2011; Lathem et al., 2013). Using the molar ratio of ammonium ions to sulfate ions, R_{SO_4}, sulfate is determined to exist as a mixture of ammonium bisulfate and sulfuric acid for R_{SO_4}<1, as ammonium sulfate and ammonium bisulfate for 1<R_{SO_4}<2, or as ammonium sulfate for R_{SO_4}>2. This method assumes that the relative contribution of nitrate is minimal (and will therefore exist mainly in the gas phase), as is the case in this study, and that there is no sodium, as this species is not measured by the AMS. Once the sulfate species type is determined, volume fractions are calculated using AMS mass fractions and the aerosol densities listed in Padró et al. (2010). The hygroscopicities of each sulfate species type are also taken from Padró et al. (2010). For mixtures of more than one compound (i.e., for the R_{SO_4}<1 or <R_{SO_4}<2 cases), inorganic properties are calculated as the average of the individual components' properties.

Alternatively, PILS-IC measurements can also be used to determine the inorganic and organic contributions to the aerosol. In this case, as measurements of Na^+ are included,

the speciation of the inorganic fraction of the aerosol becomes more complex as the addition of sodium species can greatly alter the average inorganic hygroscopicity if the relative contribution of each species within the inorganic portion of the aerosol is unknown. In order to address this issue, we employ the ISORROPIA aerosol thermodynamic equilibrium model to determine the speciation of inorganic compounds in the aerosol using the PILS-IC measurements (Nenes et al., 1998). κ and density for each of the components were taken from Padró et al (2010) when available. Otherwise, estimated intrinsic κ of Sullivan et al. (2009) were used with densities from Perry and Green (1984). As PILS-IC does not measure organic compounds, the AMS organic mass is used for calculation of volume fractions.

6.4 RESULTS

The temporal variation of κ and AMS inorganic mass fraction for ambient and PILS water-soluble ambient aerosol at s=0.4% are shown in Figure 6.3; All κ values for this study, as shown in Figure 6.3, represent the average of all κ values measured within a given 15 minute sampling period. Thermally-denuded measurements are indicated by the set point temperature which the aerosol were exposed to in the TD. Throughout the study, the trends in ambient and PILS κ are similar (not shown), though the magnitude can vary at different supersaturations as indicated in Table 6.1. Note that the standard deviations in κ in Table 6.1 for all conditions are typically very close to the $\Delta\kappa$ values of 0.033, 0.053, and 0.097 for 0.40, 0.30, and 0.20% supersaturation, respectively, calculated in Section 6.3.2.1; thus, it is expected that changes in the average reported κ are robust. PILS show a slightly larger average hygroscopicity at all s than for the ambient aerosol measured at both s=0.30% and s=0.40%. The increase in hygroscopicity of ambient aerosol with

decreasing supersaturation indicate that ambient particles have increasing hygroscopicity with size; average $d_{p,c}$ for ambient non-denuded aerosol at 0.40, 0.30, and 0.20% *s* are 83±9, 95±9, and 116±11 nm, respectively. As the mixing in the PILS system results in a completely chemically homogeneous aerosol than direct ambient measurements, PILS aerosol hygroscopicity is relatively invariant with supersaturation. As approximately 80% of the ambient aerosol measured throughout this study were found to be water-soluble (Hongyu Guo, personal correspondence, November 2013) and PILS aerosol composition and hygroscopicity is dominated by the mass and composition of the larger sampled aerosol sizes, it is expected that the PILS aerosol is also representative of the bulk ambient aerosol.. This is further supported by the fact that the ambient non-denuded aerosol hygroscopicity at the largest diameters (i.e., measured at s=0.20%) is similar to that of the measured PILS aerosol. The previous discussion makes it reasonable to assume that any additional aqueous processes taking place in PILS sampler have a negligible impact on the overall aerosol hygroscopicity. This assumption will be tested throughout the following analysis by comparing the properties of ambient aerosol measured at s=0.20%, which is expected to be most representative of the bulk aerosol and AMS measurements, and PILS aerosol measured at s=0.40%.

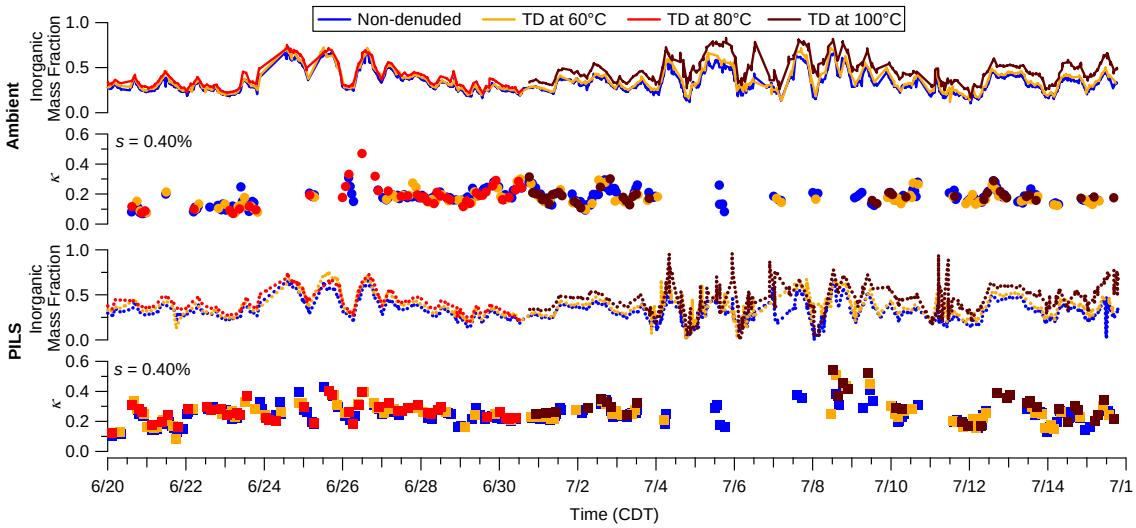

Figure 6.3: Temporal ambient (top) and PILS (bottom) κ and AMS inorganic mass fractions for the entire study. Non-denuded and thermally-denuded measurements are indicated by color. Each point represents an average of all κ values measured over each 15 minute sampling period.

Table 6.1: Average and standard deviation in κ of non-denuded and thermally-denuded ambient and water-soluble ambient aerosol.

	Ambient			PILS		
s (%)	0.40	0.30	0.20	0.40	0.30	0.20
Non-denuded	0.18±0.05	0.21±0.05	0.25±0.08	0.25±0.06	0.25±0.07	0.23±0.09
TD at 60°C	0.17±0.05	0.20±0.06	0.24±0.08	0.26±0.07	0.26±0.08	0.25±0.09
TD at 80°C	0.19±0.08	0.22±0.10	0.25± 0.10	0.26±0.06	0.27±0.07	0.27± 0.12
TD at 100°C	0.19±0.04	0.23±0.04	0.30± 0.05	0.31±0.10	0.27±0.10	0.31± 0.13

6.4.1 Thermally-denuded and Non-denuded κ

Comparisons of the hygroscopicities of thermally-denuded, referred to hereafter simply as denuded, and non-denuded aerosol sampled directly from ambient and by PILS are shown in Figure 6.4. The points shown are averages of measurements taken within each 15 minute sampling period and represent only those points where denuded and non-denuded samples were collected directly before or after one another. It is typically expected that thermally denuded aerosol would volatilize organics and show a resulting higher hygroscopicity than its non-denuded counterpart. Thermally-denuded PILS aerosol show a slightly higher hygroscopicity than the non-denuded aerosol, though these

changes in κ are only as high as approximately 10%. Thermally-denuded ambient aerosol, on the other hand, show hygroscopicity similar to that of the non-denuded aerosol.

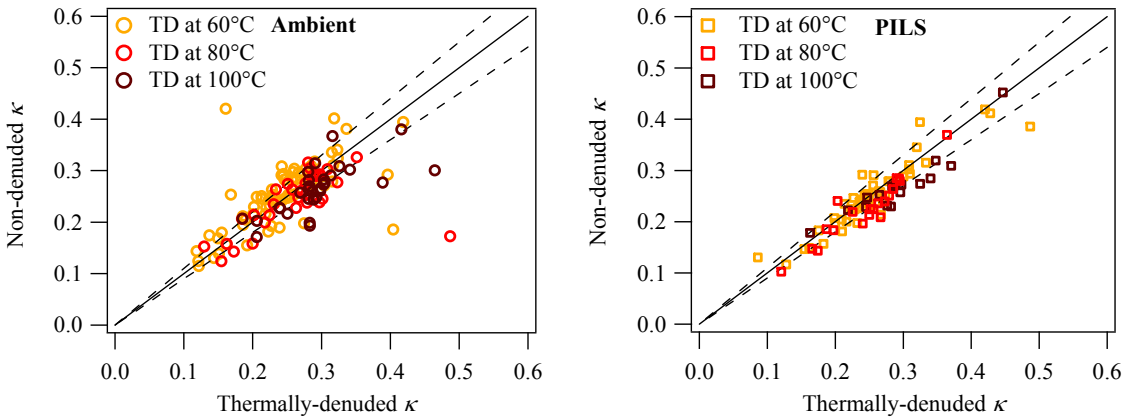

Figure 6.4: Non-denuded versus thermally-denuded κ at 60, 80, and 100°C TD sampling temperatures for ambient aerosol at s=0.20% (left) and PILS aerosol at s=0.40% (right). The solid line represents 1:1 agreement while dashed lines represent deviations of ±10%. All points shown are for periods where non-denuded measurements are directly followed by denuded measurements and vice versa.

A surprising result is that total aerosol hygroscopicity does not change much, even when significant volatilization occurs. There are several potential reasons why this may occur – here, we investigate how changes in κ are related to possible composition changes taking place in the aerosol, such as a negligible loss of mass, volatilization of inorganic material, or higher volatility compounds having higher hygroscopicity, and to the chosen measurement method. Regarding the loss of mass in the aerosol, if aerosol do not volatilize or volatilize very little material, a change in hygroscopicity after being thermally denuded would not be expected. Average ambient aerosol mass fractions remaining (MFR) calculated from AMS data and the average relative change in thermally-denuded hygroscopicity, κ_{TD}, versus non-denuded hygroscopicity, κ_o, for ambient measurements at s=0.20% and PILS measurements at s=0.40% are shown in

Table 6.2. Volatilization reaches as high as approximately 35% in the ambient aerosol and 55% in the PILS aerosol. Note that the mass fractions remaining, measured for the bulk aerosol, are not expected to be the same for the PILS and ambient aerosol due to the size-dependent composition seen only in the ambient aerosol; however, the expected changes in κ, if ambient aerosol at s=0.20% and PILS aerosol both represent bulk aerosol behavior, should be similar. Relative changes in hygroscopicity are, on average, only 12% for ambient mass losses of approximately 35%. Villani et al. (2013) also found small changes in hygroscopicity for thermally-denuded aerosol, measuring changes in subsaturated hygroscopicity generally less than 5% for thermally-denuded (from 70 to 100°C) aerosol measured at four unique ambient environments. They also found determined that particles could increase or decrease in total hygroscopicity upon thermally-denuding, as seen here.

Table 6.2: Average and standard deviation in MFR and relative change of thermally-denuded versus non-denuded aerosol for ambient κ measured at s=0.20% and PILS κ measured at s=0.40%.

	Ambient		PILS	
	MFR	$\frac{\kappa_{TD} - \kappa_o}{\kappa_o}$	MFR	$\frac{\kappa_{TD} - \kappa_o}{\kappa_o}$
TD at 60°C	0.90±0.10	-0.02±0.20	0.73±0.19	0.01±0.12
TD at 80°C	0.78±0.05	0.11±0.33	0.65±0.11	0.10±0.10
TD at 100°C	0.65±0.08	0.12±0.16	0.45±0.13	0.11±0.07

The magnitude of changes in κ is dependent on how mass is lost in the aerosol particles. Assuming that the mass loss is mainly from organics, the change in hygroscopicity expected for the data, particularly at 80 and 100°C for PILS and ambient data, should be high. For example, according to the mixing rule in Equation (6.4), if for a given particle composed of equal volumes of inorganic, assuming inorganic κ equals that of ammonium sulfate of 0.6 (Petters and Kreidenweis, 2007), and organic, assuming

organic κ of 0.2 (organic κ typically ranges from 0.1 to 0.3; Petters and Kreidenweis, 2007) measured κ would equal 0.4. If for that same particle, approximately loss of organic mass results in a particle that is 80% by volume inorganic and 20% by volume organic and assuming the same κ of inorganics and organics of 0.6 and 0.11, respectively, the resulting total κ would equal 0.52, resulting in an increase of 30% in measured κ. One issue that makes this argument more complex is that, while it might be expected that a majority of the mass fraction lost would be from organics, it is also known that inorganic compounds such as ammonium sulfate can volatilize at the temperatures in the thermodenuder. For example, ammonium sulfate aerosol has been found to volatilize at as low as 75°C (Clarke, 1991; Burtscher et al., 2001; An et al., 2007), potentially decreasing the expected change in hygroscopicity after denuding. Thus, if for the same particle used in the previous example, the total mass lost resulted in a particle with 70% inorganic volume and 30% organic volume, respectively, the resulting total κ would equal 0.45 and result in an increase of only 20%. In this case, the fraction of the total mass loss in the ambient aerosol due to inorganic volatilization, based on AMS composition data, was approximately 42±17%, 41±16%, and 44±15% at 60, 80, and 100°C, respectively, while organics were responsible for the rest of the mass loss. Thus, the small changes in κ are not completely surprising based on the above discussion.

An additional possibility for changes in κ to be suppressed even after loss of organic and inorganic materials is a decrease in the remaining organic hygroscopicity after denuding. Conventional thinking says that the more volatile the organic compounds, the less aged and less hygroscopic they are (e.g., Jimenez et al., 2009), though there has been little conclusive evidence that ambient aerosol actually behave according to this idea.

This means that if the lowest hygroscopicity compounds are volatilized first, the remaining organic compounds should be of higher hygroscopicity. If volatilized organic material is actually of higher κ than the remaining organics, however, a decrease in the hygroscopicity of the remaining organic could suppress changes seen in the total κ after denuding. In the following sections, specific changes in aerosol composition, organic hygroscopicity, and ageing will be investigated in order to attribute the changes in hygroscopicity seen between the non-denuded and denuded aerosol.

One final and necessary component in evaluating these results and their consequences on CCN is to consider the effects of ambient size-resolved chemistry seen in this study on the chosen analysis method. Regarding measurement methods, as described in Section 6.3.2, the critical dry diameter, $d_{p,c}$, is determined by matching the CCN concentration with the backwards integrated SMPS number distribution. Thus, κ is expected to be most representative of particles with similar diameter to $d_{p,c}$. According to Equation (6.1), $d_{p,c}$ at a given s will change if κ changes, as we might expect when volatilizing material in the denuder. For a mixture that is chemically homogeneous with size, as is the PILS aerosol, a change in $d_{p,c}$ should not have an effect on κ (see Table 6.1). As the ambient aerosol display size-resolved chemistry (Table 6.1), changes in chemistry with critical diameter could potentially play a role in κ; as a result, it is difficult to probe the overall changes in chemistry of a given particle (e.g., it is difficult to know the magnitude change of a given particle diameter with initial diameter $d_{p,o}$ after volatilization, especially in a chemically size-resolved system), but, as is done here, it is possible to look at how changes effect CCN activation at a given supersaturation. These changes in hygroscopicity, for a given supersaturation, are an important measure of the importance of volatilization on CCN

activity. Results reported in Table 6.2 clearly show that, even with ambient mass losses of ~35%, the effect of volatility on κ, and thus CCN activity, is small.

6.4.2 Inferred Organic Hygroscopicity

Organic hygroscopicity, κ_{org}, was inferred using composition measurements from bulk AMS and PILS-IC with ISORROPIA and the methods described in Section 6.3.3 (Table 6.3). PILS-IC compositions were averaged over 1 hour (i.e., spanning 2 periods of non-denuded PILS measurements in the PILS-AMS-CCNc setup). Using AMS components and the total measured κ to infer κ_{org} shows that, contrary to what is typically thought to happen, the κ_{org} of the less volatile fraction is decreased. Though the standard deviations in κ_{org} are nearly as large as the average κ_{org} values (Table 6.3), the consistent trend between PILS and ambient data, with the possible exception of ambient κ_{org} at 80°C where the highest standard deviation is also seen, suggests that the most volatile fraction in the aerosol actually is of higher hygroscopicity than the less volatile material. Though this contradicts the conventional view that the most volatile aerosol components are the least hygroscopic, the change in hygroscopicity of only the organic fraction of the aerosol with volatility, to the knowledge of these authors, has not been studied in the ambient. It is possible that the least volatile fraction is also the least hygroscopic due to the presence of oligomers, high molecular weight compounds with low volatility and hygroscopicity (e.g., Ervens et al., 2011; Li et al., 2011; Sareen et al., 2010; Asa-Awuku et al., 2009; Reynolds et al., 2006; Varutbangkul et al., 2006; Baltensperger et al., 2005; VanReken et al., 2005; Kalberer et al., 2004). As temperature is increased in the thermodenuder, the increased heating of particles may cause these oligomers to partially dissociate into more

volatile and more hygroscopic fragments upon heating, contributing to the decrease in hygroscopicity at increase temperatures in the TD (Table 6.3).

Table 6.3: Average and standard deviation in κ_{org} of non-denuded and denuded ambient aerosol at s=0.20% and water-soluble ambient aerosol at s=0.40% using bulk AMS composition and PILS-IC with ISORROPIA composition.

	AMS		PILS-IC
	Ambient (s=0.20%)	PILS (s=0.40%)	PILS (s=0.40%)
Non-denuded	0.14±0.09	0.14±0.06	0.11±0.07
TD at 60°C	0.12±0.08	0.12±0.06	--
TD at 80°C	0.12±0.11	0.09±0.04	--
TD at 100°C	0.08±0.07	0.08±0.06	--

In order to evaluate the importance of assumptions of the inorganic composition in inferring the organic hygroscopicity, κ_{org} was additionally determined for non-denuded PILS using data from a PILS-IC system sampling non-denuded ambient aerosol and located separate from the main PILS-CCNc-AMS setup. Data are input to the ISORROPIA aerosol equilibrium model to determine speciated composition of the inorganics, investigating how realistic the assumptions are of treating the inorganic hygroscopicity as an ammonium and sulfate system only (Section 6.3.3). ISORROPIA is able to resolve sodium, ammonium, magnesium, calcium, and potassium species. In this location, however, sodium, magnesium, calcium, and potassium components were found to typically be negligible. For this reason, there should be little difference in the assumed inorganic hygroscopicity using the AMS or PILS-IC analysis methods. The slight decrease in PILS κ_{org} (~0.03) resulting from PILS-IC versus AMS analysis confirm the validity of using simplified assumptions of aerosol speciation to calculate inorganic hygroscopicity for this study. It is not expected that these simplified assumptions made would change the trend of decreased κ_{org} with increased volatility seen here.

6.4.3 Organic Hygroscopicity and Aerosol Oxidation

The potential link between organic hygroscopicity and the level of aerosol oxidation is investigated using the κ_{org} inferred using AMS data in Section 6.4.2 with AMS measurements of the bulk O:C ratio. O:C throughout the study and for different TD sampling temperatures varied only slightly with ambient average O:C values of 0.58±0.06 for non-denuded aerosol and negligible variation in average O:C of 0.59±0.05, 0.57±0.04, and 0.59±0.06 for TD temps of 60, 80, and 100°C, respectively (Figure 6.5, left). PILS water-soluble ambient aerosol showed similar O:C values of 0.55±0.04, 0.57±0.05, 0.56±0.03, and 0.53±0.07 for non-denuded and denuded aerosol at 60, 80, and 100°C, respectively (Figure 6.5, right). Under these oxidation conditions, it is unclear whether there is any relationship between κ_{org} with O:C for the narrow range in O:C measured; correlation between κ_{org} and O:C in all cases is low ($R^2 < 0.23$ for ambient and < 0.53 for PILS aerosol).

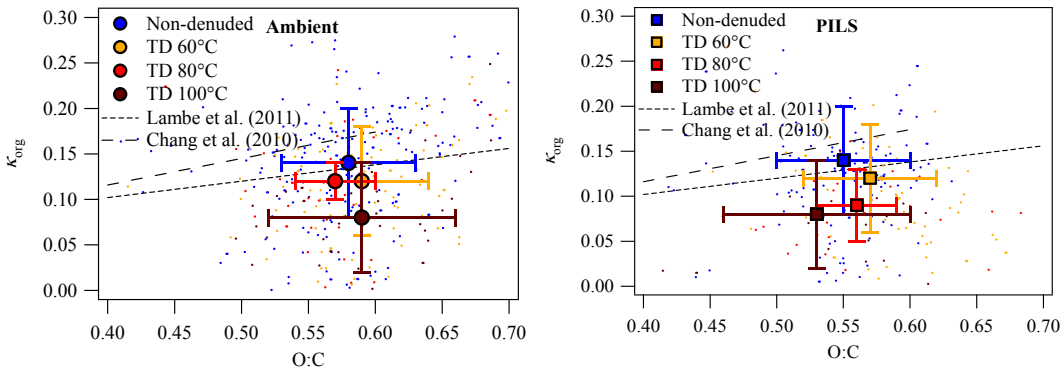

Figure 6.5: Variation in κ_{org} with O:C for ambient aerosol at s=0.2% and PILS aerosol at s=0.4% for non-denuded and thermally-denuded conditions. Small colored dots indicate all measured points while larger circles and squares indicate the averages for while errors bars indicate one standard deviation in measured values for ambient and PILS aerosol, respectively. Also shown are dashed lines indicating the parameterizations of κ_{org} with O:C from Lambe et al. (2011) and Chang et al. (2010).

The relationship between κ_{org} with average carbon oxidation state, $\overline{OS}_c$, calculated as 2*O:C-H:C, where H:C is the hydrogen to carbon ratio of the aerosol measured by AMS, is further investigated for the ambient aerosol (Figure 6.6, left). While there is again no clear relationship between κ_{org} and oxidation in terms of $\overline{OS}_c$, it appears that 100°C measurements are more oxidized in terms of $\overline{OS}_c$ than at other temperature measurement as might be expected, but not indicated by O:C. Measurements at 80°C, though, still appear to be less oxidized than thermally-denuded at 60°C. Recalling the measurement schedule (Section 6.2.2 and Figures 6.2 and 6.3), 60°C measurements were taken throughout the measurement period while 80°C were taken only during the beginning portion of the study and 100°C only during the latter portion of the study. Figure 6.6 shows the results of ambient κ_{org} and $\overline{OS}_c$ for each separate measurement period (right). In this case, oxidation state appears to be consistent with expectation in that oxidation increases as more material is volatilized as indicated by the change in $\overline{OS}_c$ between non-denuded, 60°C, and 100°C measurements (right, bottom) with comparable increases in $\overline{OS}_c$ for 60°C and 80°C measurements compared to non-denuded measurements (right, top). This is not, however, the case for O:C, as O:C of 60°C measurements remains greater than that of 100°C measurements (not shown). O:C of 60°C, 80°C, and non-denuded measurements are comparable (not shown). Overall, $\overline{OS}_c$ appears to be more consistent the expectation of the least volatile fraction being the most oxidized while O:C appears to show no correlation with volatilization. Even $\overline{OS}_c$, however, may appear to be inconsistent with theory over unique sampling periods (Figure 6.6, left). This is seemingly intuitive as changing air masses can change the relationship between hygroscopicity and volatility with oxidation, but it is still important to remember for

comparisons of oxidation measurements. Furthermore, the increase in oxidation with volatility is still consistent with the potential presence of oligomers discussed in Section 6.4.2.

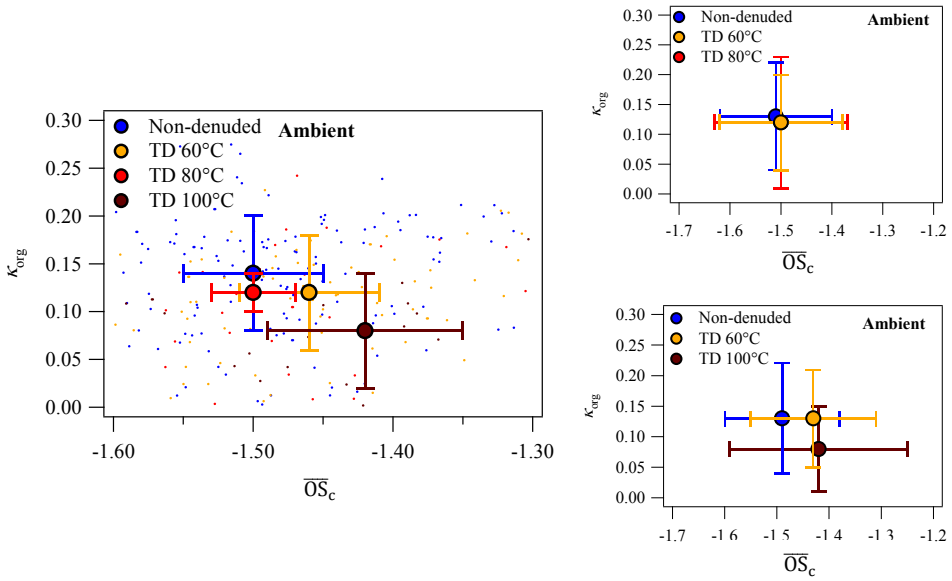

Figure 6.6: Variation in κ_{org} with $\overline{OS}_c$ for ambient aerosol at s=0.2% for the total study period (left) and for 80°C and 100°C measurement periods only (right top and bottom, respectively). Small colored dots indicate all measured points while larger circles indicate measurement averages and errors bars indicate a single standard deviation in measured values.

6.4.4 Attributing Organic Hygroscopicity to AMS Factors

AMS measurements were evaluated using Positive Matrix Factorization (PMF; Lanz et al., 2007). Results of 3-factor PMF of the total PILS aerosol measured by AMS were used to perform linear regression on the PILS non-denuded κ_{org} at s=0.40% by

$$\kappa_{org} = \varepsilon_{LVOOA}\kappa_{LVOOA} + \varepsilon_{SVOOA}\kappa_{SVOOA} + \varepsilon_{Isoprene-OA}\kappa_{Isoprene-OA} \quad (6.5)$$

where properties are representative of AMS mass spectra for low volatility oxygenated organic aerosol (LVOOA), semi-volatile oxygenated organic aerosol (SVOOA), and isoprene organic aerosol (Isoprene-OA), respectively (Lu Xu and Nga L. Ng, personal correspondence, November 2013). The densities for each factor are assumed to be equal.

A system of equations is determined using each measured PILS non-denuded κ_{org} and its corresponding PMF factor mass fractions. Results are further evaluated using a bootstrapping method and indicate that the while the average κ_{LVOOA} and $\kappa_{Isoprene-OA}$ are similar at 0.17±0.03 and 0.18±0.04, respectively, they are approximately twice as large as the average κ_{SVOOA} of 0.08±0.03 (Figure 6.7).

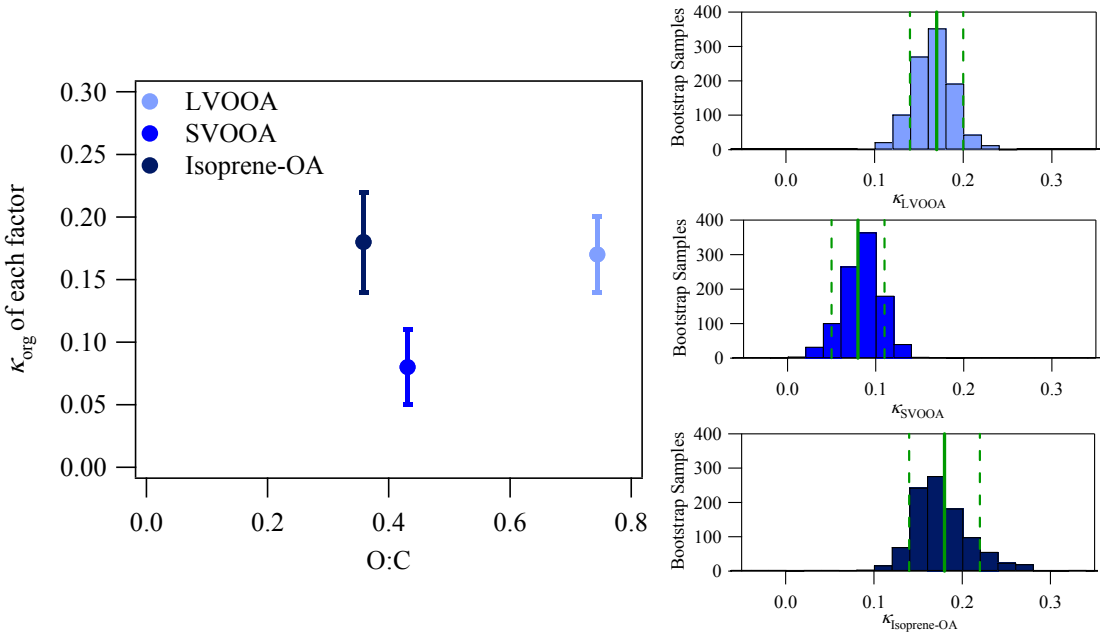

Figure 6.7: κ_{org} found for each PMF factor through linear regression versus O:C for non-denuded PILS aerosol at s=0.40% are shown on the left, where error bars represent the standard deviation. Examples of binned κ_{org} solutions from bootstrap analysis results of the linear regression are shown on the right, where the solid and dashed green lines represent the average and one standard deviation in each factor κ_{org}.

O:C, determined from the f_{44} AMS mass spectra of the three factors (Aiken et al., 2008) is highest for κ_{LVOOA}, with values of 0.74, 0.43, and 0.36 for factors κ_{LVOOA}, κ_{SVOOA}, and $\kappa_{Isoprene-OA}$, respectively. LVOOA has the highest κ_{org} and O:C, while SVOOA has the lowest κ_{org} but not the lowest O:C. In general, κ_{org} does not clearly correlate with O:C for all three factors. The increased oxidation and hygroscopicity of LVOOA as compared to SVOAA, however, is in agreement with trends reported by Jimenez et al. (2009) for

Hyytiälä, Finland as well as the accepted view that the less volatile aerosol is more highly oxidized and more hygroscopic. It is difficult to determine why Isoprene-OA displays the lowest O:C as well as a high value of κ_{org}, though this topic presents itself as an interesting area of future study. The results of O:C with κ_{org} of each PMF factor are comparable to that of $\overline{OS}_c$ with each factor κ_{org} (not shown).

6.5 CONCLUSIONS

The volatility, hygroscopicity, and oxidation of ambient and water-soluble ambient aerosol collected in a rural site in the southeastern U.S. during the SOAS field campaign were investigated. κ measured at 0.40, 0.30, and 0.20% supersaturation indicated that ambient aerosol composition was size-dependent while water-soluble ambient collected using PILS was more representative of the total bulk aerosol, which might be expected, in this case, as almost all of the ambient aerosol was found to be water-soluble. As average κ at s=0.20% for denuded and non-denuded aerosol are similar to that of the PILS at all supersaturations, PILS aerosol at s=0.40% and ambient aerosol at s=0.20% were compared throughout the rest of the study to probe total, bulk aerosol properties. In all cases, results of the ambient aerosol analysis at s=0.20% and PILS aerosol analysis s=0.40% were remarkably similar, confirming that, in this case, PILS was representative of the total bulk aerosol.

κ of thermally-denuded aerosol at 60, 80, and 100°C showed similar results for both PILS and ambient aerosol with κ increasing slightly with temperature. Even after volatilizing ~35% of ambient aerosol mass, relative changes in κ for PILS and ambient aerosol are only approximately 12%. With up to ~44% of the total mass lost due to inorganic volatilization, the small change in total κ is not entirely surprising. If this

finding is representative of other locations, this could mean that changes in volatility may be of minor significance in the case of bulk aerosol hygroscopic properties.

Furthermore, κ_{org} of the remaining aerosol after thermal-denuding was found to decrease slightly, meaning that the highest volatility organic compounds also had the highest hygroscopicities. Though this goes against conventional thinking that the highest volatility compounds are the least hygroscopic and could be due to the presence of oligomers in the aerosol that dissociate into more volatile and more hygroscopic fragments upon heating. The least volatile aerosol did appear to be the most oxidized, as expected. This however, was only indicated by $\overline{\mathrm{OS}}_c$, while no clear correlation was seen between O:C with volatility or hygroscopicity; thus, $\overline{\mathrm{OS}}_c$ has proven to be a better indicator of oxidation as discussed in Kroll et al. (2011). Results of AMS 3 factor PMF analysis for the PILS aerosol were used to attribute the organic hygroscopicity of each PMF factor to the total κ_{org}. κ_{LVOOA} and $\kappa_{Isoprene-OA}$ showed the greatest hygroscopicities of 0.17±0.03 and 0.18±0.04, respectively, and κ_{SVOOA} showed the least hygroscopicity of 0.08±0.03. No clear relationship between organic hygroscopicity and O:C was found for all factors, particularly as O:C in this study varies only slightly (average O:C of non-denuded and thermally-denuded ambient measurements range from only 0.59±0.05 to 0.57±0.04). The hygroscopicity and O:C of LVOOA, however, were greater than that of SVOOA, in agreement with the view that the least volatile aerosol is also the more oxidized and hygroscopic. Comparable results were found with comparison to $\overline{\mathrm{OS}}_c$ as an indicator of aerosol oxidation.

CHAPTER 7

CONCLUSIONS AND FUTURE RECOMMENDATIONS

7.1 SUMMARY OF RESULTS

The effect of aerosol on global climate is important and highly complex. The analysis in this work seeks to better understand the impact of organic compounds on aerosol behavior through investigating the link between aerosol hygroscopicity, volatility, oxidation, and cloud condensation nuclei (CCN) activity. This has been achieved through a number of studies conducted in laboratory experiments and in ground studies which employ a variety of instrument operation and data analysis techniques.

Chapter 3 explores aerosol hygroscopicity in a boreal forest. κ distributions were derived independently from Continuous Flow-Streamwise Thermal Gradient CCN Chamber (CFSTGC) and Hygroscopicity Tandem Differential Mobility Analyzer (HTDMA) measurements. CFSTGC-derived κ values for 40, 60, and 80 nm particles range mostly between 0.10 and 0.40 with an average characteristic of highly oxidized organics of 0.20±0.10, indicating that organics play a dominant role for this environment. Organic hygroscopicity of CCN-relevant sized particles was inferred using CFSTGC-derived κ values with bulk aerosol composition measurements. Results show that while the organic hygroscopicity found was in agreement with similar studies of boreal forests, inorganic hygroscopicity was greatly underpredicted, indicating that bulk measurements may overestimate the inorganic mass fraction of smaller particles in the study and should be used with caution particularly in regions with size-dependent composition. Diurnal trends of κ show a minimum at sunrise and a maximum in the late afternoon; this trend

covaries with f_{44}, suggesting that this trend of increased hygroscopicity with oxidation may be found across both CCN-relevant sized particles and larger particles representative of bulk composition.

Towards capturing the link between organic aerosol and volatility, Chapter 4 discusses the development and characterization of a newly-constructed thermodenuder for the study and interpretation of aerosol volatility. While thermodenuders have previously been used to investigate volatility, this work focuses on detailed understanding of instrument performance and measurement evaluations. Hygroscopicity and volatility of known, single-component organic compounds were measured in the laboratory using a volatility tandem differential mobility analyzer (VT-DMA) setup in combination with a CCN spectrometer. Measurement results were interpreted with a comprehensive instrument model that determines both the volatilized organic vapor distribution and the semi-volatile partitioning and retrieves aerosol properties with constrained uncertainty. Special attention is given to the interpretation of the size distribution of the thermodenuded aerosol, deconvolving the effects of impurities and multiple charging, and to simplifications on the treatment of thermodenuder geometry, temperature, and the cooling section, and the resulting effect on inferred particle volatility. Retrieved vapor pressures of the pure organic acids measured are consistent with published literature. Future work will focus on resolving measurements of more complex mixtures of known organics previously conducted in the laboratory with the thermodenuder model and further applying this to unknown, ambient aerosol.

The final chapters discuss the implementation of a thermodenuder in combination with measurements of CCN activity and aerosol composition in two unique studies. The

first investigates organic aerosol properties in a controlled environmental chamber. The investigation of hygroscopicity and oxidation level of thermally-denuded and non-denuded secondary organic aerosol (SOA) from toluene photo-oxidation suggests that processes aside from bulk oxidation changes may impact aerosol hygroscopicity. For all experiments, there is no clear correlation between κ_{org} and O:C or $\overline{OS}_C$. A comparison of thermally-denuded and non-denuded measurements for two experiments showed that the mean κ_{org} decreases slightly while O:C (and $\overline{OS}_C$) increased, though thermally-denuded κ_{org}, however, are still within the a standard deviation of the non-denuded κ_{org}. These results may suggest the potential for surface active compounds such as methylglyoxal or other aromatic aldehydes to act as film-forming compounds that depress surface tension and enhance CCN-activity, as the breakup of surfactant films would result in a perceived decrease in hygroscopicity. Future studies with greater ranges of oxidation conditions are needed to investigate these effects in detail.

Finally, ambient aerosol were sampled in a remote location in the southeastern United States using measurements of aerosol composition, solubility, and CCN-activity from an AMS, PILS, and CCNc, respectively. Investigation of ambient aerosol and the water-soluble portion of ambient aerosol showed that, in this case, where ambient aerosol was found to be chemically size-resolved and up to 80% of the ambient aerosol was found to water-soluble, both ambient aerosol sampled at the lowest supersaturation (s=0.20%) and water-soluble aerosol sampled at three different supersaturations (s=0.20, 0.30, and 0.40%) are representative of the bulk ambient aerosol. It was found the thermally-denuded ambient total aerosol hygroscopicity (measured at s=0.20%) increased only slightly (≤12%) even after volatilization of ~35% of the total aerosol mass, implying that

aerosol volatility may impact hygroscopicity less than expected. Additionally, the organic hygroscopicity, κ_{org}, was found to decrease at increasing thermodenuder temperatures, which goes against the conventional idea that the highest volatility aerosol are also the least hygroscopic. The aerosol did, however, increase in oxidation as thermodenuder temperature increased, based on $\overline{OS}_c$ but not necessarily O:C. Finally, the total organic hygroscopicity as well as the organic hygroscopicity related to three major factors from aerosol mass spectrometry (AMS) positive matrix factorization (PMF) analysis showed no clear correlation with the level of aerosol oxidation for all factors while low volatility oxidized organic aerosol (LVOOA) showed greater hygroscopicity and oxidation, in terms of O:C and $\overline{OS}_c$, than semi-volatile oxidized organic aerosol (SVOOA), as might be expected.

7.2 A GENERALIZED VIEW OF AEROSOL PROPERTY RELATIONSHIPS

Combined results of κ_{org} versus O:C from the CMU chamber studies in Chapter 5 with those of the SOAS field mission in Chapter 6 are shown in Figure 7.1. Also shown are several published literature parameterizations and datasets from laboratory and ambient studies. Though Hyytiälä data from Chapter 3 may correlate with O:C, the chemically size-resolved measurements do not allow for a direct comparison between κ_{org} and bulk O:C here; thus, representative measurements reported by Jimenez et al. (2009) for Hyytiälä for low volatility and semi-volatile oxygenated organic aerosol, LVOOA and SVOOA, respectively, are also shown on Figure 7.1. Additionally, the Frosch et al. (2011) parameterization, unlike the Chang et al. (2010) and Lambe et al. (2011) parameterizations from studies finding that κ_{org} was positively correlated with O:C, is

from a study where weak sensitivity of κ_{org} to O:C was found. Frosch et al. (2011) determined the parameterization from a least squares fit with r = 0.25. Measurements shown from Lathem et al. (2013) and Moore et al. (2011) are both from aircraft samples of biomass burning plumes in the Arctic. Coverage of data presented by Jimenez et al. (2009) showing the relationship of κ_{org} and growth factor of organics with O:C across several chamber and ambient studies is represented by the dark gray shaded area, while coverage of a variety of chamber studies reporting that κ_{org} was independent of oxidation by Tang et al. (2012) and Alfarra et al. (2013) are represented by the light gray and tan shaded areas, respectively. Alfarra et al. (2013) reported oxidation in terms of $f_{44,}$ which was converted to O:C for use in Figure 7.1 (Aiken et al., 2008).

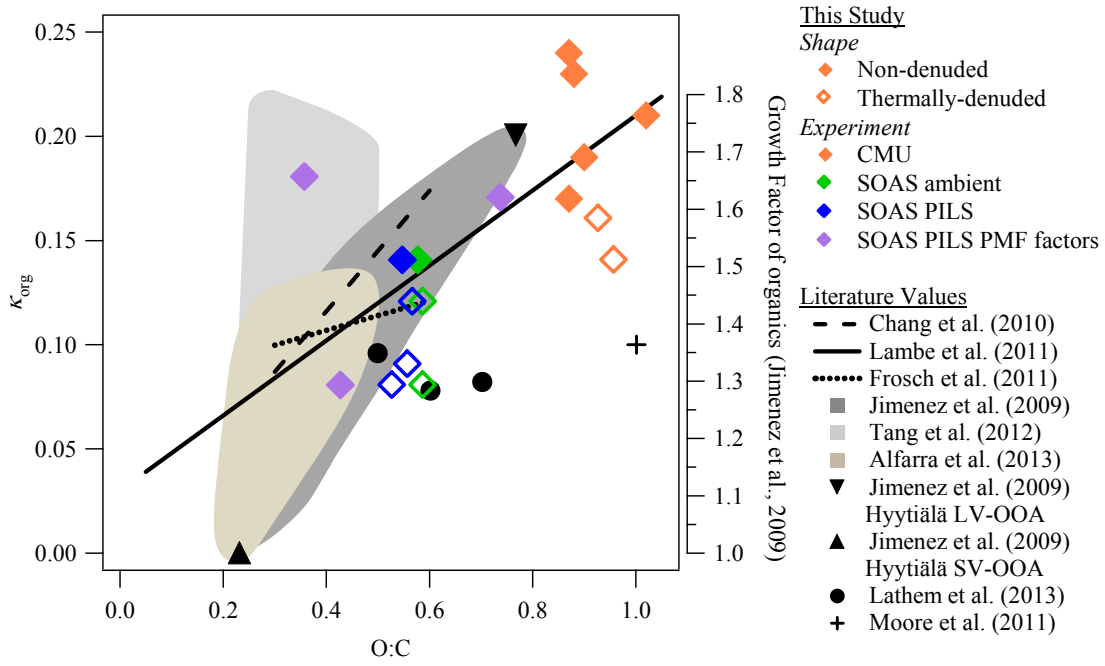

Figure 7.1: Combined results from laboratory and ambient data reported in Chapters 5 and 6 (diamonds), respectively. Non-denuded measurements are indicated by filled diamonds while open diamonds indicated thermally-denuded measurements. Also shown are two proposed parameterizations (solid and dashed black lines) and another parameterization for a study showing weak correlation between κ_{org} and O:C (dotted black line). Measurements of Hyytiälä LVOOA and SVOOA from Jimenez et al. (2009) are shown (triangles) as well as data collected from Arctic biomass burning plumes by Lathem et al. (2013) and Moore et al. (2011). General coverage of datasets of Jimenez et al. (2009), Tang et al. (2012), and Alfarra et al. (2013) are represented by the dark gray, light gray, and tan shaded areas, respectively.

For both the CMU and SOAS studies, a clear correlation between κ_{org} and bulk O:C was not seen, yet combined κ_{org} versus O:C data from all experiments (Figure 7.1) reasonably follow the general trend of increasing κ_{org} with O:C. This shows that while many detailed processes may effect κ_{org} within a narrow range of O:C, the general trend still seems to apply across a large range of O:C. Additionally, it was found for SOAS data in Chapter 5 that the most volatile aerosol were, against conventional thinking, the most hygroscopic, resulting in a lower κ_{org} in the aerosol with increased volatility. This result implied that the proposed 2-dimensional volatility framework by Jimenez et al. (2009)

where κ_{org} and O:C increases with decreasing volatility might not be as straightforward as expected. When considering all experiments, however, it seems that volatilized aerosol experiments show a generally decreased κ_{org} compared to non-denuded aerosol, while still following the κ_{org} versus O:C trend. The parameterization of Frosch et al. (2011) and the datasets of Alfarra et al. (2013) and Tang et al. (2012), all studies where a weak correlation was found between κ_{org} and O:C, also potentially appear to be consistent with an overarching correlation between κ_{org} and O:C when shown in the context of the many measurements in Figure 7.1. The results of the previous chapters combined with Figure 7.1 show the interesting complexity of looking at κ_{org} and O:C between one or several experiments versus looking at a larger view of combined laboratory and environmental datasets and illustrate the need for further study of both non-denuded and thermally-denuded ambient aerosol.

APPENDIX A

ANALYSIS OF HYGROSCOPICITY DISTRIBUTIONS

There are several assumptions made in using and analyzing results from the PDF in Equation (3.5) in order to arrive at appropriate, meaningful results for $\sigma(\kappa)$. An important issue regards the sigmoidal fit function, as it can yield non-negligible probability for atmospherically irrelevant κ (Figure A.1). For example, in Equation (3.4), when κ is ten times greater than κ^* and C=−2, then $R_a(\kappa)$=0.9E, which means that there is a 10% probability that κ >10κ^*. This is unrealistic for ambient data collected during the campaign. We have filtered the data to exclude distributions for which C>−2 as this kind of flat activation curve is often strongly influenced by multiply charged particles. On the other hand, values of C<−15 were filtered, because any values lower than −15 means that activation cannot be resolved with a supersaturation step size of 0.2%. This also happens to be the practical limit for the lowest observed C from instrument calibration experiments where higher resolution can be used. A small fraction of the data is subject to these issues and has a minimal impact on the results. We have also chosen to implement a constant upper limit for integration of 1 as this is the upper limit of atmospherically-relevant κ values (except for sea salt, whose κ≈1.2 (Petters and Kreidenweis, 2007)) and well above those seen in Hyytiälä during this campaign.

Instrument operation also induces some broadening of R_a(s) and $R_a(\kappa)$ and contributes to $\sigma(\kappa)$. An ideal instrument sampling a chemically homogenous mixture of monodisperse particles would result in $R_a(\kappa)$ being a step function with $\sigma(\kappa)$=0 and C=−1. In reality, the finite width of the DMA transfer function (Wang and Flagan, 1990) and a corresponding

transfer function in the CFSTGC from exposure to a finite range of supersaturations, the assumption of particle sphericity, and fluctuations in instrument operation (i.e., flow rate and temperature) all induce a broadening of the response to give a finite, but still steep slope for $R_a(s)$.

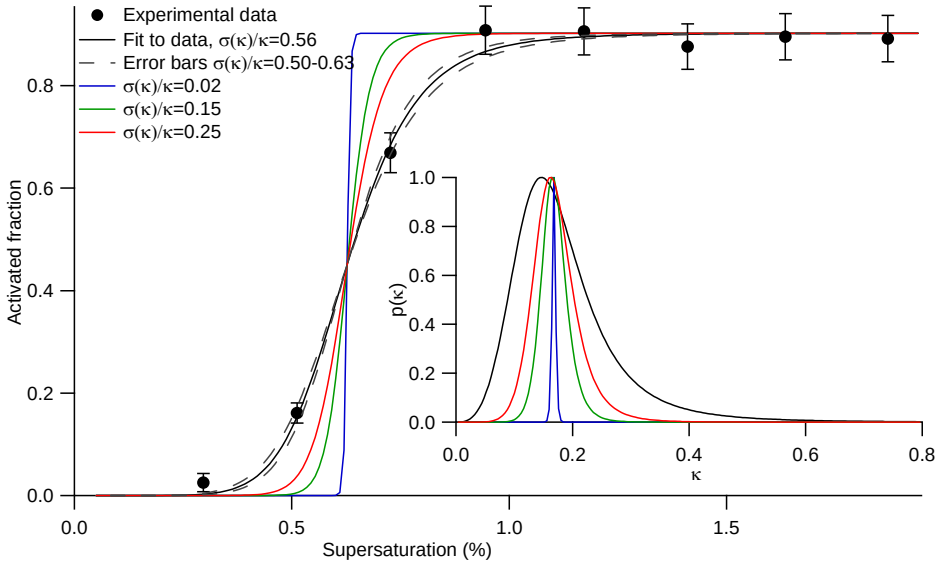

Figure A.1: An example of measured and fitted activation spectrum (60 nm dry size, 4/14/2007 18:55:00) and three examples of activation spectra with different $\sigma(\kappa)$ values. Corresponding κ distributions are shown in the inset. Error bars represent Poisson counting uncertainties.

In practice, the inferred $\sigma(\kappa)$ contains a fairly constant instrument offset and a strongly time-dependent component that represents the actual chemical variability. In terms of $\sigma(\kappa)/\kappa$, most of the observed values in Hyytiälä are between 0.25 and 1.3, so the instrument offset (~0.25) is rather small compared to the effect of chemical variability. As the first step to explain the instrument offset for $\sigma(\kappa)/\kappa$ (~0.25) we have estimated the magnitude of instrument supersaturation fluctuations. For example, the upper limit for instrument supersaturation fluctuations due to variations in CFSTGC temperatures was found to be $\sigma(s)/s$=0.01. Based on Equation (3.3), $\sigma(\kappa)=(d\kappa/ds)\sigma(s) = 2\kappa/s\sigma(s)$, which means that $\sigma(\kappa)/\kappa$ =0.02. This is a small value compared with the lowest observed value

of 0.25, and under normal operation supersaturation fluctuations can be considered as a second order effect. Several other possibilities such as fluctuations in pressure and inlet RH were also considered, but these are found to have even smaller contribution to the instrument $\sigma(\kappa)$.

As shown by Lance (2007), the DMA transfer function results in significant spread to the activation spectrum. For example, the relative width of the DMA transfer function (Wang and Flagan, 1990) for a 4.5:1 sheath-to-aerosol flow ratio is roughly $\sigma(D_p)/D_p$=0.053. Again, an order of magnitude approximation based on Equation (3.3) shows that $\sigma(\kappa)/\kappa$= 3×0.053=0.16. Another important contribution to the spread in the activation spectrum comes from multiply charged particles as these larger particles activate at lower supersaturations. There are no simple ways to estimate this effect, because the fraction of multiply charged particles depends on charging probability and size distribution at the charger, which is not always known and hardly ever constant. When expecting uniform particle distribution at the charger, accounting for multiply charged particles (Gunn, 1956; Wiedensohler and Fissan, 1988) and DMA transfer function effects (Wang and Flagan, 1990) increases $\sigma(\kappa)/\kappa$ for 80 nm particles to about 0.2, but the effect is negligible for 40 nm particles. As a result, the DMA transfer function explains 64–80% of the observed $\sigma(\kappa)$ offset. The unexplainable fraction of the $\sigma(\kappa)$ offset is caused by a combination of several second order effects such as CFSTGC transfer function, diffusion widening of the size distributions, and using the simplified hygroscopicity approach (Equation (3.3)).

Figure A.1 shows an example of a typical fitted activation curve based on ambient observations and calculated activation curves for different $\sigma(\kappa)/\kappa$ values mentioned

above. It can be seen that the steepest detected distributions ($\sigma(\kappa)/\kappa$ =0.25) are similar to the distribution based only on the DMA transfer function ($\sigma(\kappa)/\kappa$ =0.16). In addition, ambient distributions can usually be clearly distinguished from the instrument limit ($\sigma(\kappa)/\kappa$ =0.25).

To conclude, the $\sigma(\kappa)$ values include various effects of normal operation uncertainties, dominated by the DMA transfer function. With the exception of the multiply charged particles, these effects are practically time and size invariant. This means that calculated $\sigma(\kappa)$ values contain a fairly constant instrument offset (roughly 0.25 in the current data), but the remaining, much larger variations (from 0.25 to well above 1) can be related to chemical variability. More comprehensive methods exist for separating variability in particle size and composition (e.g., Lance, 2007; Su et al., 2010), but the current method is a very good approximation and very simple to implement.

The error bars in activation ratios (Figure A.1) represent Poisson counting uncertainties, which are equal to the square root of the number of observed counts. It would be possible to use these uncertainties as weights when fitting the sigmoid and in the error analysis after the fitting, but here we have used the more "traditional" approach of assuming equal weights and computing parameter uncertainties from the residual. For most activation curves, both fitting methods give similar predictions; in the example of Figure A.1, E=0.902±0.013, C=−7.78±0.73, and s^*= 0.628±0.011 assuming equal weights, while E= 0.903±0.022, C=−7.52±0.81, and s^*=0.627±0.014 for the weighted fit. Significant differences in the fitted parameters are seen only when the fits are poorly constrained by the data.

Error analysis can be used to estimate the net effect of uncertainties. Chemical variability, $\sigma(\kappa)$, is calculated from Equation (3.6), and it depends on characteristic hygroscopicity (κ^* or just κ from now on) and C. When dry particle diameter and temperature uncertainties are assumed negligible, κ uncertainty depends only on that of critical supersaturation (Δs):

$$\Delta(\kappa) = \left|\frac{\partial \kappa}{\partial s}\Delta(s)\right| = 2\frac{\kappa}{s}\Delta(s) \tag{A.1}$$

Chemical variability is an integral function, so closed form expression cannot be derived for the uncertainty. Uncertainties of C and κ must be propagated using numerically calculated gradients.

$$\Delta(\sigma(\kappa)) = \sqrt{\left(\frac{\partial \sigma(\kappa)}{\partial C}\Delta(\mathrm{C})\right)^2 + \left(\frac{\partial \sigma(\kappa)}{\partial \kappa}\Delta(\kappa)\right)^2} \tag{A.2}$$

For the relative chemical variability, _(_)/_, the uncertainty in _ must also be accounted for.

$$\Delta(\sigma(\kappa)/\kappa) = \sqrt{\left(\frac{1}{\kappa}\Delta(\sigma(\kappa))\right)^2 + \left(\frac{\sigma(\kappa)}{\kappa^2}\Delta(\kappa)\right)^2} \tag{A.3}$$

Average uncertainties are shown in Table A.1. Uncertainties of s, E, and C are based on fitting while those of the derived quantities (κ, $\sigma(\kappa)$, and $\sigma(\kappa)/\kappa$) are calculated using Equations (A.1) through (A.3).

Table A.1: Average uncertainty values for fitted (s^*, E and C) and derived (κ,$\sigma(\kappa)$ and $\sigma(\kappa)/\kappa$ parameters.

Particle Size (nm)	s^*	E	C	κ	$\sigma(\kappa)$	$\sigma(\kappa)/\kappa$
40	0.023	0.036	0.98	0.009	0.013	0.074
60	0.018	0.024	1.26	0.012	0.019	0.115
80	0.017	0.023	1.72	0.021	0.026	0.151

Few data are available for comparison of $\sigma(\kappa)/\kappa$ values; uncertainty between instrument offsets and the effect of ambient size distributions may induce additional uncertainty on the inferred chemical variability. However, Su et al. (2011) found quite

similar values for a megacity environment, indicating that variability between instruments are not dominating. The same study obtained log-normal hygroscopicity distribution parameters for several constant instrument supersaturations (see Table 1 in Su et al., 2011). Arithmetic distribution parameters were calculated from the log-normal parameters and the activation dry particle sizes were calculated from the mean hygroscopicity parameter and supersaturation (solved from Equation (3.3)) values. The results for the three closest dry particle sizes are shown in Table A.2. While our values indicate increasing $\sigma(\kappa)/\kappa$ as a function of dry particle size, there is a weaker opposite trend in the Su et al. (2011) data. Clear deviations are seen at the larger particle sizes, which possibly reflect true compositional variability between megacity and boreal forest environments.

Table A.2: Comparison of data with Su et al. (2011)

Cerully et al. (2011)				Su et al. (2010)					
Size (nm)	κ	$\sigma(\kappa)$	$\frac{\sigma(\kappa)}{\kappa}$	Size (nm)	κ_g	κ	$\sigma_g(\kappa)$	$\sigma(\kappa)$	$\frac{\sigma(\kappa)}{\kappa}$
40	0.20±0.06	0.11±0.04	0.55	39	0.30	0.35	1.74	0.21	0.60
60	0.19±0.06	0.12±0.05	0.63	55	0.38	0.42	1.60	0.21	0.50
80	0.22±0.06	0.17±0.04	0.77	75	0.47	0.54	1.67	0.29	0.54

APPENDIX B

EQUATIONS SOLVED FOR THERMODENUDER FLOW FIELD CALCULATION

Below are the equations used in the FORTRAN 77 computational fluid dynamics code used for determining the flow and other scalar fields in the thermodenuder. The equations are resented below in a similar manner as in Nenes et al. (2001).

$$\frac{\partial}{\partial t}(r\rho\phi) + \frac{\partial}{\partial z}(r\rho u\phi) + \frac{\partial}{\partial r}(r\rho v\phi) - \frac{\partial}{\partial z}\left(r\Gamma_\phi \frac{\partial \phi}{\partial z}\right) - \frac{\partial}{\partial r}\left(r\Gamma_\phi \frac{\partial \phi}{\partial r}\right) = S_\phi \qquad \text{(B.1)}$$

where the terms are substituted according to Table B.1 for the various conserved quantities.

Table B.1: Definition of source terms and transport coefficients for Equation (B.1)

Conserved Quantity	ϕ	Γ_ϕ	S_ϕ
Continuity	1	0	0
z – momentum	u	μ	$-r\frac{\partial P}{\partial r} + r\frac{\partial}{\partial z}\left(\mu\frac{\partial u}{\partial r}\right) + \frac{\partial}{\partial r}\left(r\mu\frac{\partial v}{\partial r}\right) + J_{buoy}$
r – momentum	v	μ	$-r\frac{\partial P}{\partial r} + r\frac{\partial}{\partial z}\left(\mu\frac{\partial u}{\partial r}\right) + \frac{\partial}{\partial r}\left(r\mu\frac{\partial v}{\partial r}\right) - \frac{\mu v}{r}$
Heat	T	$\frac{k_a}{c_p}$	$\frac{\Delta H}{c_p}J_{volat}$
Organic Vapor	m_{evap}	ρD_{AB}	$-\rho J_{volat}$

The source term for thermal buoyancy effects is defined as

$$J_{buoy} = -\rho g_{\lambda_2}\left[\frac{T - T_{bulk}(r)}{T_{bulk}(r)}\right] \qquad \text{(B.2)}$$

where g_{λ_2} is the component of gravity in the r direction and $T_{bulk}(r)$ is the average temperature along z at position r.

The source (or sink) term for organic vapor is defined as

$$J_{volat} = \frac{\pi\rho}{2M}\sum_{i=1}^{n} N_i d_{pi}^2 \frac{dd_{pi}}{dt} \quad \text{(B.3)}$$

where *n* is the number of size bins in the aerosol distribution with particular diameter and number concentration, and the rate of change is obtained from Equation (B.2), the aerosol evaporation equation.

APPENDIX C

TABLE OF LITERATURE VOLATILITY PARAMETER VALUES

Table C.1: Compiled literature values for reference volatility parameters. The listed values regard either vaporization or sublimation as indicated by the phase designation – either solid (S) or supercooled liquid (L). If the source did not provide adequate information to make such a conclusion, then "?" is used to indicate that phase is not specified. Uncertainties presented in the literature source are translated (if necessary) to maximum and minimum bounds with an average value. C^* is calculated as in Table 4.2.

	P^o(298K) ($Pa \times 10^{-5}$)			ΔH ($J\ mol^{-1} \times 10^5$)			Phase	C^*(298K) ($\mu g\ m^{-3}$)
	Avg.	Max.	Min.	Avg.	Max.	Min.		
Adipic Acid								
Bilde et al. (2003)	0.98	1.47	0.49	1.54	1.60	1.48	S	0.578
Saleh et al. (2010) [a]	3.30	4.20	2.40	1.32	1.40	1.24	S	1.947
Saleh et al. (2010) [h]	4.20	6.40	2.00	1.26	1.47	1.05	S	2.477
Salo et al. (2010)	5.80	7.60	4.40	0.97	1.05	0.89	S	3.421
Cappa et al. (2007)	0.26	0.36	0.16	1.45	1.50	1.40	S	0.153
Riipinen et al. (2007)	0.40	0.50	0.30	1.48*	1.70*	1.26*	S	0.236
Riipinen et al. (2007)	17.00	20.00	14.00	1.13	1.35	0.91	L	10.03
Chatto. et al. (2001)	1.70	-	-	1.40	-	-	?	1.003
Saleh et al. (2009)	3.40	4.60	2.00	1.35	1.48	1.22	S	2.005
Booth et al. (2009)	0.33	0.71	-0.06	1.19	1.45	0.93	S	0.193
Booth et al. (2010)	21.40	37.45	5.35	0.83	1.09	0.57	L	12.62
Azelaic Acid								
Bilde et al. (2003)	0.60	0.90	0.30	1.53	1.77	1.29	S	0.456
Saleh et al. (2010) [a]	1.40	1.90	0.90	1.45	1.60	1.30	S	1.064
Saleh et al. (2010) [h]	0.90	1.20	0.60	1.58	1.75	1.41	S	0.684
Salo et al. (2010)	4.70	5.50	4.00	0.96	1.01	0.91	S	3.571
Cappa et al. (2007)	1.00E-03	1.60E-03	4.00E-04	1.78	1.83	1.73	S	7.6E-04
Malonic Acid								
Bilde et al. (2003)	36.00	54.00	18.00	0.92	1.07	0.77	S	15.12
Soonsin et al. (2010)	43.00	58.00	28.00	0.96	1.07	0.85	L	18.06
Soonsin et al. (2010)	8.00	10.90	5.10	1.07	1.11	1.03	S	3.360
Riipinen et al. (2007)	5.20	6.30	4.10	1.41*	1.66*	1.16*	S	2.184
Riipinen et al. (2007)	49.00	59.00	39.00	1.22	1.47	0.97	L	20.58
Booth et al. (2009)	57.30	68.70	45.90	0.92	0.96	0.88	S	24.07
Booth et al. (2010)	319.00	558.25	79.75	0.73	0.77	0.69	L	134.0
Pope et al. (2010)	67.00	93.00	55.00	1.42	1.62	1.22	L	28.14

Succinic Acid								
Bilde et al. (2003)	3.90	5.85	1.95	1.38	1.49	1.27	S	1.859
Salo et al. (2010)	6.40	8.40	4.60	1.12	1.24	1.00	S	3.050
Cappa et al. (2007)	3.20	3.80	2.60	1.28	1.30	1.26	S	1.525
Riipinen et al. (2007)	2.50	3.10	1.90	1.37*	1.60*	1.14*	S	1.192
Riipinen et al. (2007)	99.00	123.00	75.00	1.04	1.27	0.81	L	47.19
Soonsin et al. (2010)	170.00	220.00	120.00	1.06	1.14	0.98	L	81.03
Soonsin et al. (2010)	0.60	0.81	0.39	1.25	1.33	1.17	S	0.286
Saleh et al. (2009)	37.00	48.00	26.00	0.88	0.91	0.85	S	17.64
Booth et al. (2009)	11.30	16.00	6.60	0.93	0.99	0.87	S	5.386
Booth et al. (2010)	386.00	675.50	96.50	0.62	0.68	0.56	L	184.0
Suberic Acid								
Bilde et al. (2003)	0.12	0.18	0.06	1.84	1.96	1.72	S	0.084
Chatto. et al. (2001)	0.34	-	-	1.48	-	-	?	0.239
Salo et al. (2010)	1.40	2.00	1.00	1.01	1.11	0.91	S	0.984
Cappa et al. (2007)	0.02	0.03	0.01	1.68	1.75	1.61	S	0.013
Booth et al. (2011)	2.23	3.90	0.56	1.53†	1.65†	1.41†	L	1.568
Pimelic Acid								
Bilde et al. (2003)	5.10	7.65	2.55	1.47	1.58	1.36	S	3.297
Chatto. et al. (2001)	1.20	-	-	1.78	-	-	?	0.776
Salo et al. (2010)	17.00	25.00	12.00	1.27	1.47	1.07	S	10.99
Cappa et al. (2007)	0.39	0.45	0.33	1.53	1.57	1.49	S	0.252
Booth et al. (2011)	26.30	46.03	6.58	1.23†	1.34†	1.12†	L	17.00
Saleh et al. (2009)	7.20	8.90	5.50	1.49	1.59	1.39	S	4.655

[a]Atomization used as the aerosol generation technique
[h]Homogeneous nucleation used as the aerosol generation technique
*ΔH_{sub} calculated by using equation and reference values for ΔH_{fus} (Yaws, 2003; Booth et al., 2010) and heat capacity from liquid results
†ΔH_{vap} obtained from Bilde et al. (2003) estimates of solid values

APPENDIX D

DATA INVERSION SENSITIVITY TESTS

Volatility parameter retrievals were repeated for various assumptions regarding certain aspects of the model. First, the parameters retrieved for all experimental simulations were repeated for the case where just the heating section was considered and are compared to simulations that included the full model geometry (Figure D.1a). Including only the heating section results in an increase of the retrieved saturation vapor pressures by about a factor of two on average with a corresponding slight decrease in the enthalpy change. This is associated with the comparably shorter residence time in the model domain in that case which then requires a higher volatility across all temperature settings in order to fit the experimental data.

Second, the parameter retrieval for all simulations was repeated for two different cases of different accommodation coefficients: 0.1 and 0.01, compared to the base case of unity (Figure D.1b). The results indicate that, in general, a decrease in accommodation coefficient by an order of magnitude results in a corresponding increase in saturation vapor pressure. This is the greatest sensitivity observed for our experimental conditions but is actually dampened by an increase in the aerosol mass concentration (not shown).

Additional sensitivity tests are also presented to assess the sensitivity of the parameter retrieval to experimental variation in relevant temperatures. These tests were done for one of the organic compounds under consideration (adipic acid) under both the assumption of unity accommodation coefficient and using the available literature value (the two separate points in Figure D.1c, d). The experimental conditions for the adipic acid

measurements are less than+/- 1 K in the thermodenuder set point temperature at the first thermocouple (wall boundary condition) and +/- 5 K in the thermodenuder inlet temperature. The wall temperature variation has a larger potential impact than variations in the inlet temperature; however, the variation is still small and within the estimated uncertainty range.

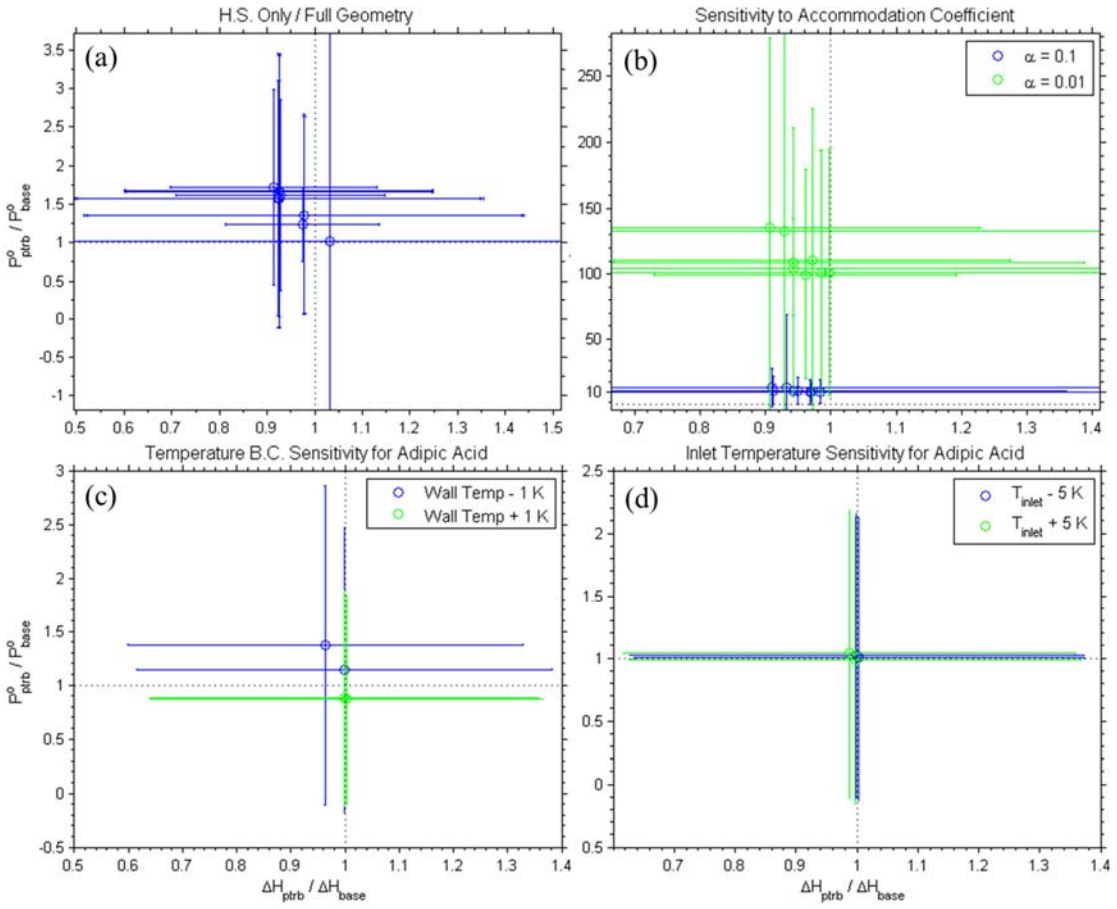

Figure D.1: Model sensitivity tests for (a) whether or not the cooling section is considered, (b) variation in the accommodation coefficient, (c) variation in the wall temperature boundary conditions, and (d) variation in the inlet temperature.

APPENDIX E

MODAL DIAMETER FOR NON-VOLATILE RESIDUALS AND MULTIPLY CHARGED PARTICLES

To confirm that the smallest mode is consistent with the amount of impurities in the aerosol, the non-volatile residual diameter, $d_{p,resid}$, was estimated from the reported fractional mass purity (f) for each compound considered, the inlet diameter, $d_{p,in}$, the density of the organic compound (ρ_{org}), and an assumption about the density of the residual matter (ρ_{resid}):

$$d_{p,resid} = \left(d_{p,in}^3 \frac{\rho}{\rho_{resid}} (1 - f) \right)^{1/3} \quad \text{(E.1)}$$

$d_{p,resid}$ is computed twice, assuming ρ_{resid} is equal to the density of NaCl (ρ_{NaCl}) and assuming it has the same density as the organic component (ρ_{org}). The two calculations were performed to illustrate the uncertainty associated with the residual diameter. The uncertainty in the inlet diameter measurement (from the width of the DMA transfer function) is also propagated through the estimate of the residual diameter. These calculated values were compared with the $d_{p,out}$ values of the lowest diameter mode from the SMPS data. Figure E.1 illustrates the comparison for each organic acid at the reported mass purities. The data appear to fall into two distinct sets of points in the figures: one close to the 1:1 line and another well underneath it. For malonic acid, the mass purity was assumed to be 98%. Particular observations were considered to be affected by low-volatility material when values of $d_{p,out}$ and $d_{p,resid}$ fall within uncertainty near the 1:1 line. Data that was just outside of agreement were also considered to be contaminated. The

contribution of impurities from the deionized water is not thought to be important, as atomization of pure deionized water did not show any appreciable particle concentrations.

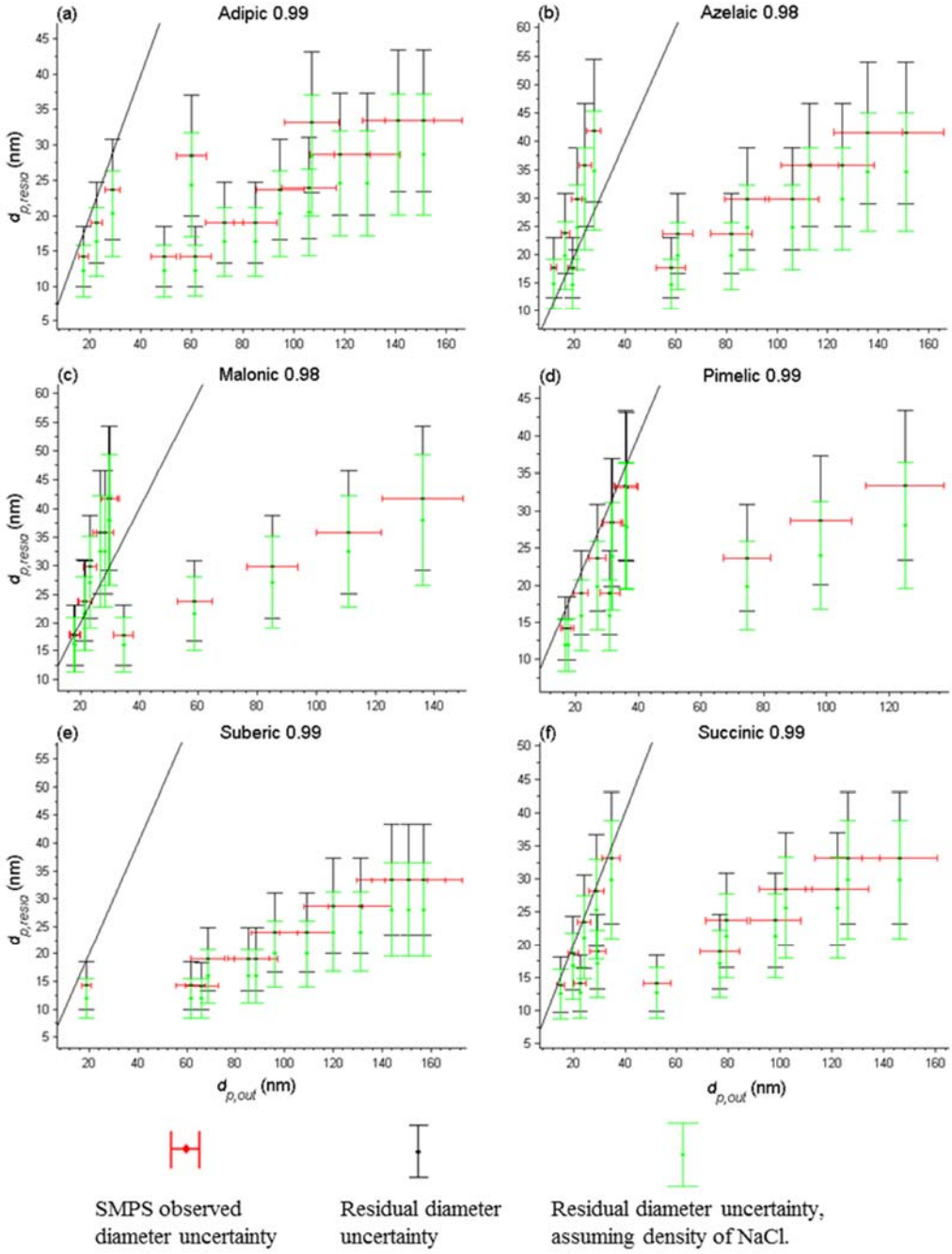

Figure E.1: Observed outlet diameter against the expected residual diameter calculated by Equation (D.1). The uncertainty in the observations is based on the DMA transfer function for a 10:1 sheath to aerosol flow ratio. The uncertainty in the calculated residual diameters is propagated through Equation (D.1). Uncertainty in the residual component density is represented by choosing two possible densities: NaCl or the organic compound (black/green).

The electrical mobility of particles in the DMA is related to particle properties by

$$Z_e = \frac{qC_c}{3\pi\mu d_p} \tag{E.2}$$

with μ defined as the viscosity of air, q is the number of elementary charges on the particle, and $C_c(d_p) = 1 + \frac{2\lambda}{D_p}\left[1.257 + 0.4\exp\left(-\frac{1.1d_p}{2\lambda}\right)\right]$ is the Cunningham slip correction factor (Seinfeld and Pandis, 2006). The presence of double-charged particles can explain the largest diameter mode in the occasional tri-modal distribution observed for thermodenuded aerosol, and is determined as follows. Considering a spherical aerosol with the same electrical mobility as the single-charged aerosol with $d_{p,in}$, the double-charged diameter, $d_{p,2x}$, application of Equation (E.2) yields

$$d_{p,2x} = \frac{2C_c(d_{p,2x})}{1C_c(d_{p,in})} d_{p,in} \tag{E.3}$$

The dependence of C_c on particle diameter requires the calculation to be iterated until it converges to a particular value of $d_{p,2x}$. These $d_{p,2x}$ were then used to initialize the aerosol module using the same volatility parameters estimated from the fitting of the middle mode of the thermodenuded particles. The model results (d_{pm}) were compared against the largest diameter mode in the observed size distribution ($d_{p,out}$) (Figure E.2). Suberic and pimelic acid results are not shown because neither was observed to exhibit trimodal size distributions in the measurements, likely because the former did not volatilize enough while the latter was too volatile. Figure E.2 clearly shows that the model-predicted outlet diameter for the double-charged particles agrees with the largest diameter mode, regardless of the number of modes observed; thus, the third (rightmost on SMPS scan) mode was not observed when the outlet diameters for the double-charged and single-charged outlet diameters were similar. This explanation is consistent with the laboratory

setup where the particle charge distribution was re-equilibrated at the second DMA downstream of the thermodenuder.

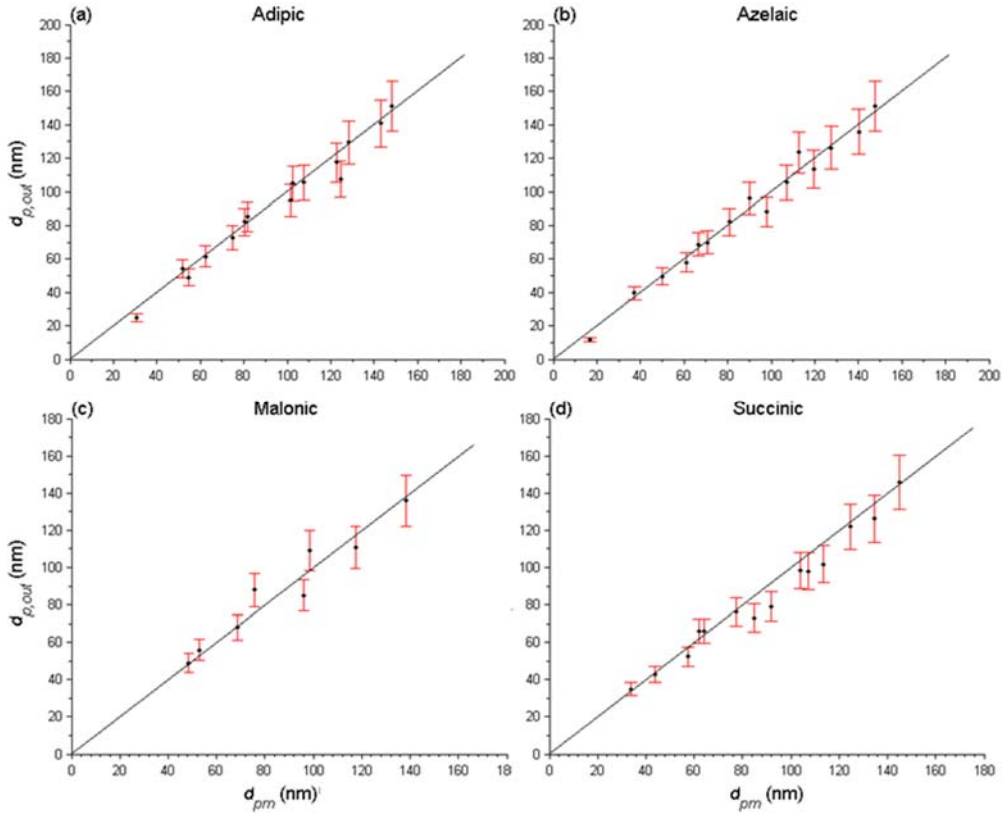

Figure E.2: Output of the thermodenuder model (d_{pm}) when it was initialized with the calculated double-charged diameters ($d_{p,2x}$) versus the largest observed outlet mode diameter ($d_{p,out}$). Error bars represent the measurement uncertainty from the DMA transfer function.

The additional possibility that nucleation in the thermodenuder cooling section could cause the smallest size mode to appear in the SMPS scans is considered. Direct comparison of the SMPS and CPC measured total particle concentrations before and after the thermodenuder is inconclusive, considering the problems associated with the SMPS inversion process when the sample aerosol are charge neutralized a second time before the second DMA. Thus, an alternative approach is considered to determine if nucleation could consistently explain the appearance of the smallest mode. For this, we estimate the

maximum saturation ratio, R_n, of the gas phase as follows. To first order, the organic vapor pressure at any point in the thermodenuder is equal to the vapor that initially enters it plus the amount that volatilizes from the aerosol phase

$$P_\infty = P_\infty(z = 0) + \frac{m_{evap} R T_\infty}{M} \quad \text{(E.4)}$$

where m_{evap} is the volatilized mass concentration (kg m^{-3} air), R is the ideal gas constant, and T_∞ is the local temperature. Since aerosol in this study are generated by atomization and subsequent rapid drying of aqueous solution, little time is allowed for equilibration between the aerosol and vapor phases, so we assume that P_∞(z = 0) is negligible. We then express $R_n = \frac{P_\infty}{P^o}$ as

$$R_n = \frac{P_\infty(z=0)}{P^o} + \frac{m_{evap} R T_\infty}{M P^o} \cong \frac{m_{evap} R T_\infty}{M P^o} \quad \text{(E.5)}$$

The maximum saturation ratio is calculated at the expected temperature of the cooling section, 25°C, using literature values for the saturation vapor pressures (Figure E.3). Of particular interest are the results for malonic (Figure E.3d) and suberic (Figure E.3e) acids. Based on this calculation, it would be much more likely for nucleation to occur in the suberic acid experiments than in the malonic acid experiments because the saturation ratios at the highest temperatures for the former could be up to over twelve times higher than the latter – which were, moreover, subsaturated. However, visual inspection of the separate SMPS scans for all of the malonic and suberic acid results shows that the appearance of the smallest mode occurs more often (most scans) for malonic acid but inconsistently for suberic acid (Figure E.4). Thus, the hypothesis that vapor buildup could be causing nucleation in the cooling section appears to be inconsistent with the data. Considering that a more consistent alternative hypothesis exists (above), the smallest

diameter modes in the SMPS are more likely do to residual non-volatile cores that arising from nucleation in the thermodenuder.

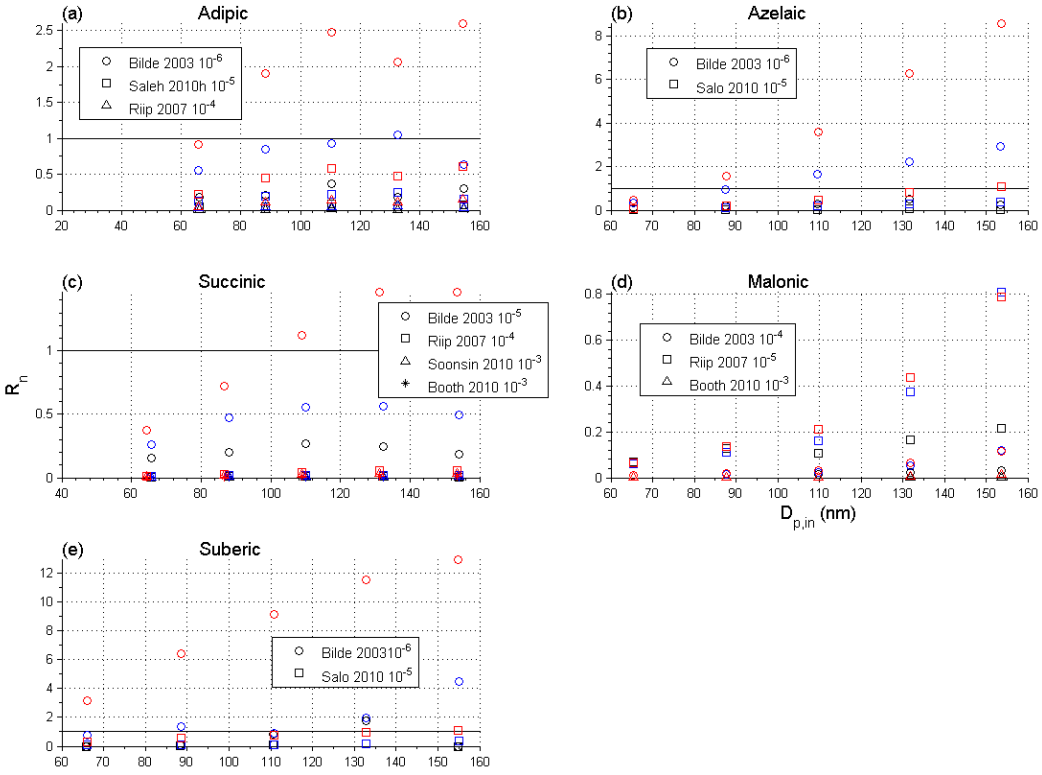

Figure E.3: The value of R_n is compared against the inlet diameter ($d_{p,in}$) and is calculated for a variety of P^o indicated by the legend entries which reference corresponding rows in Table 4.2 of the main text and at a nominal cooling section temperature of 25°C. The color scheme used to indicate the temperature set point is the same as in Figure 4.9. In effect, R_n provides a maximum possible saturation ratio in the cooling section, based on thermodynamic parameters in the literature and the measured experimental data.

Data tables for each set of experiments are presented in Appendix F. Errors in the size distribution measurement could influence the optimization; this is particularly important when packaged SMPS analysis software, such as the Aerosol Instrument Manager (AIM) program (TSI, version 8.1.0.0), is used as it automatically outputs the mode with the highest concentration, even if it may not represent the mode that expresses the true particle volatility. For this reason we present modal diameters automatically identified by

AIM and that using our method that corrects for the presence of doublets and non-volatile cores. Comments indicate points omitted due to non-volatile core interference (NV) and points adjusted to an alternative mode considering either non-volatile core interference and presence of double-charged particles or both (AM).

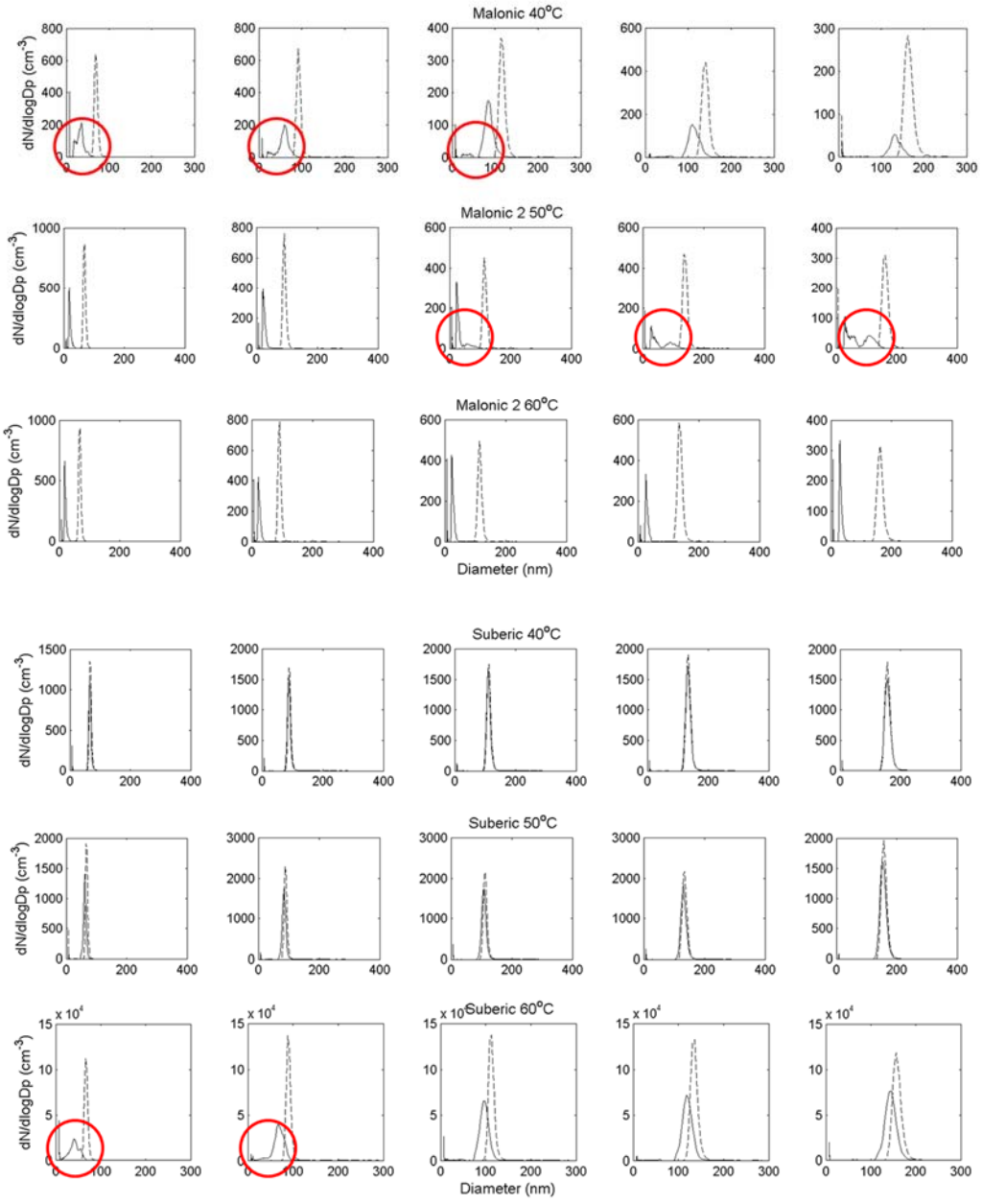

Figure E.4: Sample scans of thermodenuded malonic (top 3 rows) and suberic acid aerosol at temperature set points of 40, 50, and 60˚C

APPENDIX F

MODE DIAMETER DATA TABLES FROM EXPERIMENTS

Table F.1: Adipic acid average mode diameter data

Set point temperature (°C)	$d_{p,in}$ (nm)	$d_{p,out}$ observed by AIM (nm)	$d_{p,out}$ using correct mode (nm)	Comment
40	66.0	61.5	61.5	
	88.3	85.1	85.1	
	111	106	106	
	133	129	129	
	155	151	151	
50	65.9	49.0	49.0	
	88.2	72.8	72.8	
	110	94.7	94.7	
	1.33	118	118	
	1.55	141	141	
60	65.8	17.5	-	NV
	88.2	22.5	-	NV
	110	28.9	57.3	AM
	132	59.8	82.1	AM
	154	107	107	

Table F.2: Azelaic acid average mode diameter data

Set point temperature (°C)	$d_{p,in}$ (nm)	$d_{p,out}$ observed by AIM (nm)	$d_{p,out}$ using correct mode (nm)	Comment
40	65.3	58.0	58.0	
	87.5	82.0	82.0	
	110	106	106	
	132	126	126	
	153	151	151	
50	65.3	19.1	35.9	AM
	87.5	60.8	60.8	
	110	88.2	88.2	
	132	113	113	
	153	136	136	
60	65.4	11.8	-	NV
	87.6	16.3	-	NV
	110	20.9	-	NV
	132	24.1	56.0	AM
	154	27.6	87.1	AM

Table F.3: Malonic acid average mode diameter data

Set point temperature (°C)	$d_{p,in}$ (nm)	$d_{p,out}$ observed by AIM (nm)	$d_{p,out}$ using correct mode (nm)	Comment
40	65.5	16.0	33.0	AM
	87.7	54.3	54.3	
	110	81.1	81.1	
	132	104	104	
	154	129	129	
50	65.5	25.9	-	NV
	87.7	30.3	-	NV
	110	34.6	-	NV
	132	35.2	-	NV
	154	39.2	52.7	AM
60	65.5	25.9	-	NV
	87.7	30.0	-	NV
	110	34.0	-	NV
	132	34.2	-	NV
	154	38.5	-	NV

Table F.4: Pimelic acid average mode diameter data

Set point temperature (°C)	$d_{p,in}$ (nm)	$d_{p,out}$ observed by AIM (nm)	$d_{p,out}$ using correct mode (nm)	Comment
40	65.9	17.7	-	NV
	88.2	30.9	46.7	AM
	110	74.6	74.6	
	133	98.2	98.2	
	155	125	125	
50	65.8	16.8	-	NV
	88.1	21.7	-	NV
	110	26.9	-	NV
	132	31.4	-	NV
	154	36.3	-	NV
60	65.9	16.8	-	NV
	88.2	21.7	-	NV
	110	26.9	-	NV
	132	31.8	-	NV
	155	35.9	-	NV

Remarks: Do not expect to obtain a robust parameter fit due to non-volatile core interference.

Table F.5: Suberic acid average mode diameter data

Set point temperature (°C)	$d_{p,in}$ (nm)	$d_{p,out}$ observed by AIM (nm)	$d_{p,out}$ using correct mode (nm)	Comment
40	65.9	66.1	65.9	Growth (w/in uncert.)
	88.4	88.2	88.2	
	111	109	109	
	133	131	131	
	155	157	155	Growth (w/in uncert.)
50	66.1	61.5	61.5	
	88.5	85.1	85.1	
	111	109	109	
	133	131	131	
	155	151	151	
60	66.1	18.7	40.9	AM
	88.5	68.6	68.6	
	111	95.9	95.9	
	133	120	120	
	155	144	144	

Table F.6: Succinic acid average mode diameter data

Set point temperature (°C)	$d_{p,in}$ (nm)	$d_{p,out}$ observed by AIM (nm)	$d_{p,out}$ using correct mode (nm)	Comment
40	65.7	52.3	52.3	
	88.0	76.4	76.4	
	110	98.2	98.2	
	132	122	122	
	154	146	146	
50	65.7	22.5	-	NV
	88.0	29.4	52.7	AM
	110	79.1	79.1	
	132	102	102	
	154	126	126	
60	64.5	15.1	-	NV
	86.7	19.9	-	NV
	109	24.1	-	NV
	131	28.9	-	NV
	154	34.6	-	NV

REFERENCES

Aalto, P. and Kulmala, M.: Using a cloud condensation nuclei counter to study CCN properties and concentrations, Boreal Env. Res., 5, 349–359, 2000.

Aiken, A. C., DeCarlo, P. F., Kroll, J. H., Worsnop, D. R., Huffman, J. A., Docherty, K., Ulbrich, I. M., Mohr, C., Kimmel, J. R., Sueper, D., Zhang, Q., Sun, Y., Trimborn, A., Northway, M., Ziemann, P. J., Canagaratna, M. R., Onasch, T. B., Alfarra, R., Prevot, A. S. H., Dommen, J., Duplissy, J., Metzger, A., Baltensperger, U., and Jimenez, J. L.: *O/C* and *OM/OC* ratios of primary, secondary, and ambient organic aerosols with high-resolution time-of-flight aerosol mass spectrometry, Environ. Sci. Technol., 42, 4478–4485, 2008.

Alfarra, M. R., Coe, H., Allan, J. D., Bower, K. N., Boudries, H., Canagaratna, M. R., Jimenez, J. L., Jayne, J. T., Garforth, A. A., Li, S.-M., and Worsnop, D. R.: Characterization of urban and rural organic particulate in the Lower Fraser Valley using two Aerodyne aerosol mass spectrometers, Atmos. Environ., 38, 5745-5758, 2004.

Alfarra, M. R., Good, N., Wyche, K. P., Hamilton, J. F., Monks, P. S., Lewis, A. C., and McFiggans, G.: Water uptake is independent of the inferred composition of secondary aerosols derived from multiple biogenic VOCs, Atmos. Chem. Phys., 13, 11769-11789, doi: 10.5194/acp-13-11769-2013, 2013.

Allan, J. D., Jimenez, J. L., Williams, P. I., Alfarra, M. R., Bower, K. N., Jayne, J. T., Coe, H., and Worsnop, D. R.: Quantitative sampling using an aerodyne aerosol mass spectrometer 1: Techniques of data interpretation and error analysis, J. Geophys. Res., 108, 4090, doi: 10.1029/2002JD002358, 2003.

Allan, J. D., Delia, A. E., Coe, H., Bower, K. N., Alfarra, M. R., Jimenez, J. L., Middlebrook, A. M., Drewnick, F., Onasch, T. B., Canagaratna, M. R., Jayne, J. T., and Worsnop, D. R.: A generalized method for the extraction of chemically resolved mass spectra from Aerodyne Aerosol Mass Spectrometer data, J. Aerosol Sci., 35, 909–922, 2004.

Allan, J. D., Alfarra, M. R., Bower, K. N., Coe, H., Jayne, J. T., Worsnop, D. R., Aalto, P. P., Kulmala, M., Hyötyläinen, T., Cavalli, F., and Laaksonen, A.: Size and composition measurements of background aerosol and new particle growth in a Finnish forest during QUEST 2 using an Aerodyne Aerosol Mass Spectrometer, Atmos. Chem. Phys., 6, 315–327, doi: 10.5194/acp-6-315-2006, 2006.

An, W. J., Pathak, R. K., Lee, B. H. Pandis, S. N.: Aerosol volatility measurement using an improved thermodenuder: Application to secondary organic aerosol, J. Aerosol Sci., 48, 305-314, doi: 10.1016/j.jaerosci.2006.12.002, 2007.

Andreae, M. O. and Rosenfeld, D.: Aerosol-cloud-precipitation interactions. Part 1. The nature and sources of cloud-active aerosols, Earth-Sci. Rev., 89, 13–41, 2008.

Asa-Awuku, A., and Nenes, A.: The effect of solute dissolution kinetics on cloud droplet formation: Extended Köhler theory, J. Geophys. Res.,112, D22201, doi: 10.1029/2005JD00693, 2007.

Asa-Awuku, A., Sullivan, A. P., Hennigan, C. J., Weber, R. J., and Nenes, A.: Investigation of molar volume and surfactant characteristics of water-soluble organic compounds in biomass burning aerosol, Atmos. Chem. Phys., 8, 799-812, doi: 10.5194/acp-8-799-2008, 2008.

Asa-Awuku, A., Engelhart, G. J., Lee, B. H., Pandis, S. N., and Nenes, A.: Relating CCN activity, volatility, and droplet growth kinetics of β-caryophyllene secondary organic aerosol, Atmos. Chem. Phys., 9, 795–812, doi: 10.5194/acp-9-795-2009, 2009.

Asa-Awuku, A., Nenes, A., Gao, S., Flagan, R. C., and Seinfeld, J. H.: Water-soluble SOA from Alkene ozonolysis: composition and droplet activation kinetics inferences from analysis of CCN activity, Atmos. Chem. Phys., 10, 1585–1597, doi:10.5194/acp-10-1585-2010, 2010.

Asa-Awuku, A., Moore, R. H., Nenes, A., Bahreini, R., Holloway, J. S., Brock, C. A., Middlebrook, A. M., Ryerson, T., Jimenez, J., DeCarlo, P., Hecobian, A., Weber, R., Stickel, R., Tanner, D. J., and Huey, L. G.: Airborne Cloud Condensation Nuclei Measurements during the 2006 Texas Air Quality Study, J. Geophys. Res., 116, D11201, doi: 10.1029/2010JD014874, 2011.

Baltaretu, C. O., Lichtman, E. I., Hadler, A. B. and Elrod, M. J.: Primary atmospheric oxidation mechanism for toluene, The journal of physical chemistry. A, 113, 221-230, doi: 10.1021/jp806841t, 2009.

Baltensperger, U., Kalberer, M., Dommen, J., Paulsen, D., Alfarra, e Sax, M., Steinbacher, M., Prevot, A. S. H., Sjoren, S., Weingartner, and Zenobi, R.: Secondary organic aerosols from anthropogenic and biogenic precursors, Faraday Discussions, 130, 265, doi: 10.1039/B417367H, 2005.

Barth, M., McFadden, J. P., Sun, J., Wiedinmyer, C., Chuang, P., Collins, D., Griffin, R., Hannigan, M., Karl, T., Kim, S.-W., Lasher-Trapp, S., Levis, S., Litvak, M., Mahowald, N., Moore, K., Nandi, S., Nenes, A., Potosnak, M., Raymond, T. M., Smith, J., Still, C., and Stroud, C.: Coupling between land ecosystems and the atmospheric hydrologic cycle through biogenic aerosol pathways, Bull. Amer. Meteor. Soc., 86, 1738–1742, 2005.

Bilde, M., Svenningsson, B., Mønster, J., and Rosenørn, T.: Even-odd alternation of evaporation rates and vapor pressures of C3-C9 dicarboxylic acid aerosols, Environ. Sci. Tech., 37, 1371, 2003.

Bird, R. B., Stewart, W. E., Lightfoot, E. N.: Transport Phenomena (2nd ed.), New York, NY: John Wiley & Sons, Inc., 2002.

Birmili, W., Schwirn, K., Nowak, A., Petäjä, T., Joutsensaari, J., Rose, D., Wiedensohler, A., Hämeri, K., Aalto, P., Kulmala, M., and Boy, M.: Measurements of humidified particle number size distributions in a Finnish boreal forest: derivation of hygroscopic particle growth factors, Boreal Env. Res., 14, 458–480, 2009.

Booth, A. M., Markus, T., McFiggans, G., Percival, C. J., McGillen, M. R., and Topping, D. O.: Design and construction of a simple Knudsen Effusion Mass Spectrometer (KEMS) system for vapour pressure measurements of low volatility organics, Atmos. Meas. Tech., 2, 355-361, doi: 10.5194/amt-2-355-2009, 2009.

Booth, A. M., Barley, M. H., Topping, D. O., McFiggans, G., Garforth, A., and Percival, C. J.: Solid state and sub-cooled liquid vapor pressures of substituted dicarboxylic acids using Knudsen Effusion Mass Spectrometry (KEMS) and Differential Scanning Calorimetry, Atmos. Chem. Phys., 10, 4879-4892, doi: 10.5194/acp-10-4879-2010, 2010.

Booth, A. M., Montague, W. J., Barley, M. H., Topping, D. O., McFiggans, G., Garforth, A., and Percival, C. J. (2011). Solid state and sub-cooled liquid vapor pressures of cyclic aliphatic dicarboxylic acids, Atmos. Chem. Phys., 11,655-665, doi: 10.5194/acp-11-655-2011, 2011.

Bougiatioti, A., Fountoukis, C., Kalivitis, N., Pandis, S. N., Nenes, A., and Mihalopoulos, N.: Cloud condensation nuclei measurements in the marine boundary layer of the Eastern Mediterranean: CCN closure and droplet growth kinetics, Atmos. Chem. Phys., 9, 7053–7066, doi: 10.5194/acp-9-7053-2009, 2009.

Bougiatioti, A., Nenes, A., Fountoukis, C., Kalivitis, N., Pandis, S. N., and Mihalopoulos, N.: Size-resolved CCN distributions and activation kinetics of aged continental and marine aerosol, Atmos. Chem. Phys., 11, 8791–8808, doi: 10.5194/acp-11-8791-2011, 2011.

Boy, M., Petäjä, T., Dal Maso, M., Rannik, Ü., Rinne, J., Aalto, P., Laaksonen, A., Vaattovaara, P., Joutsensaari, J., Hoffmann, T., Warnke, J., Apostolaki, M., Stephanou, E. G., Tsapakis, M., Kouvarakis, A., Pio, C., Carvalho, A., Römpp, A., Moortgat, G., Spirig, C., Guenther, A., Greenberg, J., Ciccioli, P., and Kulmala, M.: Overview of the field measurement campaign in Hyytiälä, August 2001 in the framework of the EU project OSOA, Atmos. Chem. Phys., 4, 657–678, doi: 10.5194/acp-4-657-2004, 2004.

Broekhuizen, K., Kumar, P. P., and Abbatt, J. P. D.: Partially soluble organics as cloud condensation nuclei: Role of trace soluble and surface active species, Geophys. Res. Lett., 31, L01107, doi: 10.1029/2003GL018203, 2004.

Brown, P. N., Byrne, G.D., and Hindmarsh, A. C.: VODE, a variable-coefficient ODE solver, SIAM J. Sci. Comput., 10, 1038–1051, 1989.

Burtscher, H., Baltensperger, U., Bukowiecki, N., Cohn, P., Hüglin, C., Mohr, M., Matter, U., Nyeki, S., Schmatloch, V., Streit, N., and Weingartner, E.: Separation of volatile and non-volatile aerosol fractions by thermodesorption: instrumental development and applications, J. Aerosol Sci., 32, 427-442, doi: 10.1016/S0021-8502(00)00089-6, 2001.

Canagaratna, M. R., Jayne, J. T., Jimenez, J. L., Allan, J. D., Alfarra, M. R., Zhang, Q., Onasch, T. B., Drewnick, F., Coe, H., Middlebrook, A., Delia, A., Williams, L. R., Trimborn, A. M., Northway, M. J., DeCarlo, P. F., Kolb, C. E., Davidovits, P., and Worsnop, D. R.: Chemical and microphysical characterization of ambient aerosols with the Aerodyne aerosol mass spectrometer, Mass Spectrom. Rev., 26, 185–222, 2007.

Cappa, C. D.: A model of aerosol evaporation kinetics in a thermodenuder. Atmos. Meas. Tech., 3, 579-592, doi: 10.5194/amt-3-579-2010, 2010.

Cappa, C. D., and Jimenez, J. L.: Quantitative estimates of the volatility of ambient organic aerosol, Atmos. Chem. Phys., 10, 5409-5424, doi: 10.5194/acp-10-5409-2010, 2010.

Cappa, C. D., Lovejoy, E. R., and Ravishankara, A. R.: Determination of evaporation rates and vapor pressures of very low volatility compounds: A study of the C_4-C_{10} dicarboxylic acids, J. Phys. Chem., 111, 3099-3109, doi: 10.1021/jp068686q, 2007.

Carlton, A. G., Goldstein, A. and Jimenez, J. F.: The Southern Oxidant and Aerosol Study (SOAS): Measuring and modeling at the interface of air quality and climate change to understand biosphere-atmosphere interactions [White Paper], Retrieved October 2013 from http://climate.envsci.rutgers.edu/SOAS/SOAS_White_Paper_final.pdf.

Cerully, K. M., Raatikainen, T., Lance, S., Tkacik, D., Tiitta, P., Petäjä, T., Ehn, M., Kulmala, M., Worsnop, D. R., Laaksonen, A., Smith, J. N., and Nenes, A.: Aerosol hygroscopicity and CCN activation kinetics in a boreal forest environment during the 2007 EUCAARI campaign, Atmos. Chem. Phys. 11, 12369-12386, doi: 10.5194/acp-11-12369-2011, 2011.

Cerully, K., Hite, J., McLaughlin, M., and Nenes, A. (2013) Towards the Determination of Joint Volatility-Hygroscopicity Distributions: Instrument Development and

Response Characterization for Single-Component Aerosol, Aeros. Sci. Tech., 48, 295-311, doi: 10.1080/02786826.2013.870326, 2014.

Chang, R. Y.-W., Slowik, J. G., Shantz, N. C., Vlasenko, A., Liggio, J., Sjostedt, S. J., Leaitch,W. R., and Abbatt, J. P. D.: The hygroscopicity parameter (κ) of ambient organic aerosol at a field site subject to biogenic and anthropogenic influences: relationship to degree of aerosol oxidation, Atmos. Chem. Phys., 10, 5047–5064, doi: 10.5194/acp-10-5047-2010, 2010.

Chattopadhyay, S., Tobias, H. J., and Ziemann, P. J.: A method for measuring vapor pressures of low-volatility organic aerosol compounds using a thermal desorption particle beam mass spectrometer, Anal. Chem., 73, 3797-3803, 2001.

Chuang, P. Y.: Measurements of the timescale of hygroscopic growth for atmospheric aerosols, J. Geophys. Res., 108, 4282, doi: 10.1029/2002JD002757, 2003.

Chuang, P. Y., Charlson, R. J., and Seinfeld, J. H.: Kinetic limitations on droplet formation in clouds, Nature, 390, 594–596, 1997.

Clarke, A. D.: A thermo-optic technique for in-situ analysis of size-resolved aerosol physicochemistry, Atmos. Environ., 25, 635-644, doi: 10.1016/0960-1686(91)90061-B, 1991.

Corrigan, C. E., and Novakov, T.: Cloud condensation nucleus activity of organic compounds: a laboratory study, Atmos. Environ., 33, 2661-2668, doi: 10.1016/S1352-2310(98)00310-0, 1999.

Crosier, J., Jimenez, J. L., Allan, J. D., Bower, K. N., Williams, P. I., Alfarra, M. R., Canagaratna, M. R., Jayne, J. T., Worsnop, D. R., and Coe, H.: Technical note: Description and use of the new Jump Mass Spectrum mode of operation for the Aerodyne Quadrupole Aerosol Mass Spectrometers (Q-AMS), Aerosol Sci. Tech., 41, 865–872, 2007.

Cruz, C. N., and Pandis, S. N.: A study of the ability of pure secondary organic aerosol to act as cloud condensation nuclei, Atmos. Environ., 31, 2205-2214, doi: 10.1016/S1352-2310(97)00054-X, 1997.

DeCarlo, P. F., Kimmel, J. R., Trimborn, A., Northway, M. J., Jayne, J. T., Aiken, A. C., Gonin , M., Fuhrer, K., Horvath, T., Docherty, K. S, Worsnop, D. R, and Jimenez, J. L.: Field-deployable, high-resolution, time-of-flight aerosol mass spectrometer, Anal. Chem., 78, 8281–8289, doi: 10.1021/ac061249n, 2006.

de Gouw, J. A., Goldan, P. D., Warneke, C., Kuster, W. C., Roberts, J. M., Marchewka, M., Bertman, S. B., Pszenny, A. A. P. and Keene, W. C.: Validation of proton transfer reaction-mass spectrometry (PTR-MS) measurements of gas-phase organic compounds in the atmosphere during the New England Air Quality Study

(NEAQS) in 2002, J. Geophys. Res.-Atmos., 108, 4682, doi: 10.1029/2003JD003863, 2003.

Donahue et al., N. M., Robinson, A. L., Stanier, C. O., and Pandis, S. N.: Coupled partitioning, dilution, and chemical aging of semivolatile organics. Environ. Sci. Tech., 40, 2635-2643, doi: 10.2012/es052297c, 2006.

Donahue, N. M., Robinson, A. L., and Pandis, S. N.: Atmospheric organic particulate matter: From smoke to secondary organic aerosol. Atmos. Environ., 43, 94-106, doi: 10.1016/j.atmosenv.2008.09.055, 2009.

Dusek, U., Frank, G. P., Hildebrandt, L., Curtius, J., Schneider, J., Walter, S., Chand, D., Drewnick, F., Hings, S., Jung, D., Bormann, S., and Andreae, M. O.: Size matters more than chemistry for cloud-nucleating ability of aerosol particles, Science, 312, 1375-1378, doi: 10.1126/science.1125261, 2006.

Dusek, U., Frank, G. P., Curtius, J., Drewnick, F., Schneider, J., Kürten, A., Rose, D., Andreae, M. O., Borrmann, and Pöschl, U.: Enhanced organic mass fraction and decreased hygroscopicity of cloud condensation nuclei (CCN) during new particle formation events, Geophys. Res. Lett., 37, L03804, doi: 10.1029/2009GL040930, 2010.

Ehn, M., Petäjä, T., Aufmhoff, H., Aalto, P., Hämeri, K., Arnold, F., Laaksonen, A., and Kulmala, M.: Hygroscopic properties of ultrafine aerosol particles in the boreal forest: diurnal variation, solubility and the influence of sulfuric acid, Atmos. Chem. Phys., 7, 211–222, doi: 10.5194/acp-7-211-2007, 2007.

Engelhart, G. J., Asa-Awuku, A., Nenes, A., and Pandis, S. N.: CCN activity and droplet growth kinetics of fresh and aged monoterpene secondary organic aerosol, Atmos. Chem. Phys.,8, 3937–3949, doi: 10.5194/acp-8-3937-2008, 2008.

Engelhart, G. J., Moore, R. H., Nenes, A., and Pandis, S. N.: Cloud condensation nuclei activity of isoprene secondary organic aerosol, J. Geophys. Res., 116, D02207, doi: 10.1029/2010JD014706, 2011.

Ervens, B., Turpin, B. J., and Weber, R. J.: Secondary organic aerosol formation in cloud droplets and aqueous particles (aqSOA): a review of laboratory, field and model studies, Atmos. Chem. Phys., 11, 11069-11102, doi: 10.5194/acp-11-11069-2011, 2011.

Ervens, B., Wang, Y., Eagar, J., Leaitch, W. R., Macdonald, A. M., Valsaraj, K. T., and Herckes, P.: Dissolved organic carbon (DOC) and select aldehydes in cloud and fog water: the role of the aqueous phase in impacting trace gas budgets, Atmos. Chem. Phys., 13, 5117-5135, doi: 10.5194/acp-13-5117-2013, 2013.

Facchini, M. C., Mircea, M., Fuzzi, S., and Charlson, R. J.: Cloud albedo enhancement by surface-active organic solutes in growing droplets, Nature, 401, 257-259, doi: 10.1038/45758, 1999.

Facchini, M. C., Decesari, S., Mircea, M., Fuzzi, S., and Loglio, G.: Surface tension of atmospheric wet aerosol and cloud/fog droplets in relation to their organic carbon content and chemical composition, Atmos. Environ., 34, 4853-4857, 2000.

Faulhaber, A. E., Thomas, B. M., Jimenez, J. L., Jayne, J. T., Worsnop, D. R., and Ziemman, P. J.: Characterization of a thermodenuder-particle beam mass spectrometer system for the study of organic aerosol volatility and composition. Atmos. Chem. Phys., 2, 15-31, doi: 10.5194/amt-2-15-2009, 2009.

Feingold, G., and Chuang, P. Y.: Analysis of the influence of film-forming compounds on droplet growth: Implication for cloud microphysical processes and climate. J. Atmos. Sci., 59, 2006-2018, 2002.

Fierz, M., Vernooij, M. G. C., and Burtscher, H.: An improved low-flow thermodenuder. J. Aerosol Sci., 38, 1163-1168, doi:10.1016/j.jaerosci.2007.08.006, 2007.

Frosch, M., Zardini, A. A., Platt, S. M., Müller, L., Reinnig, M.-C., Hoffmann, T., and Bilde, M.: Thermodynamic properties and cloud droplet activation of a series of oxo-acids, Atmos. Chem. Phys., 10, 5873-5890, doi:10.5194/acp-10-5873-2010, 2010.

Frosch, M., Bilde, M., DeCarlo, P. F., Jurányi, Z., Tritscher, T., Dommen, J., Donahue, N. M., Gysel, M., Weingartner, E., and Baltensperger, U.: Relating cloud condensation nuclei activity and oxidation level of α-pinene secondary organic aerosols. J. Geophys. Res., 116, D2212, doi: 10.1029/2011JD01640, 2011.

Frosch, M., Bilde, M., Nenes, A., Praplan, A. P., Jurányi, Z., Dommen, J., Gysel, M., Weingartner, E., and Baltensperger, U.: CCN activity and volatility of β-caryophyllene secondary organic aerosol, Atmos. Chem. Phys. 13, 2283-2297, doi: 10.5194/acp-13-2283-2013, 2013.

Fuchs, N. and Sutugin, A.: High dispersed aerosols, in: Topics in Current Aerosol Research, vol. 2, Pergamon Press, Oxford, 1971.

Fuentes, E., and McFiggans, G.: A modeling approach to evaluate the uncertainty in estimating evaporation behavior and volatility of organic aerosols. Atmos. Meas. Tech., 5, 735-757, doi: 10.5194/amt-5-735-2012, 2012.

Fuller, E. N., Schettle, P. D., and Giddings, J. C.: A new method for prediction of binary gas-phase diffusion coefficients. Ind. Eng. Chem., 58, 18-57, 1966.

Gantt, N., Xu, J., Meskhidze, N., Zhang, Y., Nenes, A., Ghan, S. J., Liu, X., Easter, R., and Zaveri, R.: Global distribution and climate forcing of marine organic aerosol – Part 2: Effects on cloud properties and radiative forcing. Atmos. Chem. Phys., 12, 6555-6563, doi: 10.5184/acp-12-6555-2012, 2012.

Goldstein, A. H., and Galbally, I. E.: Known and unexplored organic constituents in the Earth's atmosphere, Environ. Sci. Tech., 5, 1514-1521, doi: 10.1021/es072476p, 2007.

Good, N., Topping, D. O., Allan, J. D., Flynn, M., Fuentes, E., Irwin, M., Williams, P. I., Coe, H., and McFiggans, G.: Consistency between parameterizations of aerosol hygroscopicity and CCN activity during the RHaMBLe discovery cruise, Atmos. Chem. Phys., 10, 3189–3203, doi:10.5194/acp-10-3189-2010, 2010.

Gunn, R. and Woessner, R.: Measurements of the systematic electrification of aerosols, J. Coll. Sci., 11, 254–259, 1956.

Gunthe, S. S., King, S. M., Rose, D., Chen, Q., Roldin, P., Farmer, D. K., Jimenez, J. L., Artaxo, P., Andreae, M. O., Martin, S. T., and Pöschl, U.: Cloud condensation nuclei in pristine tropical rainforest air of Amazonia: size-resolved measurements and modeling of atmospheric aerosol composition and CCN activity, Atmos. Chem. Phys., 9, 7551–7575, doi: 10.5194/acp-9-7551-2009, 2009.

Hallquist, M., Wenger, J. C., Baltensperger, U., Rudich, Y., Simpson, D., Claeys, M., Dommen, J., Donahue, N. M., George, C., Goldstein, A. H., Hamilton, J. F., Herrmann, H., Hoffmann, T., Iinuma, Y., Jang, M., Jenkin, M. E., Jimenez, J. L., Kiendler-Scharr, A., Maenhaut, W., McFiggans, G., Mentel, Th. F., Monod, A., Prévôt, A. S. H., Seinfeld, J. H., Surratt, J. D., Szmigielski, R., and Wildt, J.: The formation, properties and impact of secondary organic aerosol: current and emerging issues. Atmos. Chem. Phys., 9, 5155-5236, doi: 10.5194/acp-9-5155-2009, 2009.

Hämeri, K., Väkevä, M., Aalto, P. P., Kulmala, M., Swietlicki, E., Zhou, J., Seidl, W., Becker, E., and O'Dowd, C., D.: Hygroscopic and CCN properties of aerosol particles in boreal forests, Tellus, 53B, 359–379, 2001.

Hamilton, J. F., Webb, P. J., Lewis, A. C., and Reviejo, M. M.: Quantifying small molecules in secondary organic aerosol formed during the photo-oxidation of toluene with hydroxyl radicals, Atmos. Environ., 39, 7263-7275, 2005.

Hari, P. and Kulmala, M.: Station for Measuring Ecosystem–Atmosphere Relations (SMEAR II), Boreal Env. Res., 10, 315– 322, 2005.

Hinds, William C.: Aerosol technology: properties, behavior, and measurement of airborne particles (2nd ed.), New York, NY: John Wiley & Sons, Inc., 1999.

Hong, J., Häkkinen, S. A. K., Paramonov, M., Äijälä, M., Hakala, J., Nieminen, T., Mikkilä, J., Prisle, N., Kulmala, M., Riipinen, I., Bilde, M., Kerminen, V.-M., and Petäjä, T.: Hygroscopicity, CCN and volatility properties of submicron atmospheric aerosol in a boreal forest environment during the summer of 2010, Atmos. Chem. Phys. Discuss., 13, 29097-29136, doi: 10.5194/acpd-13-29097-2013, 2013.

Hori, M., Ohta, S., Murao, N., and Yamagata, S.: Activation capability of water soluble organic substances as CCN. J. Aerosol. Sci., 34, 419–448, 2003.

Hu, D., Tolocka, M., Li, Q., Kamens, R. M.: A kinetic mechanism for predicting secondary organic aerosol formation from toluene oxidation in the presence of NO_x and natural sunlight, Atmos. Environ., 41, 6478-6496, doi: 10.101/j.atmosenv.2007.04.025, 2007.

Huff Hartz, K. E. H., Tischuk, J. E., Chan, M. N., Chan, C. K., Donahue, N. M., and Pandis, S. N.: Cloud condensation nuclei activation of limited solubility organic aerosol. Atmos. Environ., 40, 605–617, doi: 10.1016/j.atmosenv.2005.09.076, 2006.

Huffman, J. A., Ziemann, P. J., Jayne, J. T., Worsnop, D. R., and Jimenez, J. L.: Development and Characterization of a Fast-Stepping/Scanning Thermodenuder for Chemically-Resolved Aerosol Volatility Measurements. Aerosol Sci. Tech., 42, 395-407, doi: 10.1080/02786820802104981, 2008.

Hyvärinen, A.-P., Lihavainen, H., Gaman, A., Vairila, L., Ojala, H., Kulmala, M., and Viisanen, Y.: Surface tensions and densities of oxalic, malonic, succinic, maleic, malic, and cis-pinonic acids. J. Chem. Eng. Data, 51, 255, doi: 10.1021/je050366x, 2006.

Intergovernmental Panel on Climate Change (IPCC): Climate Change 2007: The Physical Science Basis, Summary for Policymakers, Retrieved from http://www.ipcc.ch/ publications_and_data/ar4/syr/en/contents.html, 2007.

Intergovernmental Panel on Climate Change (IPCC): Climate Change 2013: The Physical Science Basis, Summary for Policymakers, Retrieved from http://www.ipcc.ch/report/ar5/wg1/, 2013.

International Mathematical and Statistical Library, Houston, Texas, (program IMSL-ZXSSQ).

Irwin, M., Robinson, N., Allan, J. D., Coe, H., and McFiggans, G.: Size-resolved aerosol water uptake and cloud condensation nuclei measurements as measured above a Southeast Asian rainforest during OP3, Atmos. Chem. Phys., 11, 11157-11174, doi:10.5194/acp-11-11157-2011, 2011.

Jayne, J. T., Leard, D. C., Zhang, X., Davidovits, P., Smith, K. A., Kolb, C. E., Worsnop, D. R: Development of an aerosol mass spectrometer for size and composition analysis of submicron particles, Aerosol Sci. Tech., 33, 49–70, 2000.

Jensen, J. B. and Charlson, R. J.: On the efficiency of nucleation scavenging, Tellus, 36, 367–375, 1984.

Jimenez, J. L., Jayne, J. T., Shi, Q., Kolb, C. E., Worsnop, D. R., Yourshaw, I., Seinfeld, J. H., Flagan, R. C., Zhang, X., Smith, K. A., Morris, J., and Davidovits, P.: Ambient aerosol sampling using the Aerodyne Aerosol Mass Spectrometer, J. Geophys. Res., 108, 8425, doi: 10.1029/2001JD001213, 2003.

Jimenez, J.L., Canagaratna, M. R., Donahue, N. M., Prevot, A. S. H., Zhang, Q., Kroll, J. H., DeCarlo, P. F., Allan, J. D., Coe, H., Ng, N. L., Aiken, A. C., Docherty, K. S., Ulbrich, I. M., Grieshop, A. P., Robinson, A. L., Duplissy, J., Smith, J. D., Wilson, K. R., Lanz, V. A., Hueglin, C., Sun, Y. L., Tian, J., Laaksonen, A., Raatikainen, T., Rautiainen, J., Vaattovaara, P., Ehn, M., Kulmala, M., Tomlinson, J. M., Collins, D. R., Cubison, M. J., Dunlea, E. J., Huffman, J. A., Onasch, T. B., Alfarra, M. R., Williams, P. I., Bower, K., Kondo, Y., Schneider, J., Drewnick, F., Borrmann, S., Weimer, S., Demerjian, K., Salcedo, D., Cottrell, L., Griffin, R., Takami, A., Miyoshi, T., Hatakeyama, S., Shimono, A., Sun, J. Y., Zhang, Y. M., Dzepina, K., Kimmel, J. R., Sueper, D., Jayne, J. T., Herndon, S. C., Trimborn, A. M., Williams, L. R., Wood, E. C., Middlebrook, A. M., Kolb, C. E., Baltensperger, U., and Worsnop, D. R.: Evolution of organic aerosols in the atmosphere, Science, 326, 1525–1529, doi: 10.1126/science.1180353, 2009.

Kalberer, M., Paulsen, D., Sax, M., Steinbacher, M., Dommen, J., Prevot, A. S. H., Fisseha, R., Weingartner, E., Frankevich, V., Zenobi, R., and Baltensperger, U.: Identification of polymers as major components of atmospheric organic aerosols, Science, 303, 1659–1662, doi: 10.1126/science.1092185 , 2004.

Kanakidou, M., Seinfeld, J. H., Pandis, S. N., Barnes, I., Dentener, F. J., Facchini, M. C., Van Dingenen, R., Ervens, B., Nenes, A., Nielsen, C. J., Swietlicki, E., Putaud, J. P., Balkanski, Y., Fuzzi, S., Horth, J., Moortgat, G. K., Winterhalter, R., Myhre, C. E. L., Tsigaridis, K., Vignati, E., Stephanou, E. G., and Wilson, J.: Organic aerosol and global climate modelling: a review, Atmos. Chem. Phys., 5, 1053–1123, doi: 10.5194/acp-5-1053-2005, 2005.

King, S. M., Rosenoern, T., Shilling, J. E., Chen, Q., and Martin, S. T.: Increased cloud activation potential of secondary organic aerosol for atmospheric mass loadings, Atmos. Chem. Phys., 9, 2959-2971, doi: 10.5194/acp-9-2959-2009, 2009.

Köhler, H.: The nucleus in and the growth of hygroscopic droplets, T. Faraday Soc., 43, 1152–1161, 1936.

Kroll, J. H., and Seinfeld, J. H.: Chemistry of secondary organic aerosol: Formation and evolution of low-volatility organic in the atmosphere, Atmos. Environ., 42, 3593-3624, 2008.

Kroll, J. H., Smith, J. D., Che, D. L., Kessler, S. H., Worsnop, D. R., and Wilson, K. R.: Measurement of fragmentation and functionalization pathways in the heterogeneous oxidation of oxidized organic aerosol, Phys. Chem. Chem. Phys., 2009, 11, 8005-8014, doi: 10.1039/B905289E, 2009a.

Kroll, J., Worsnop, D., Kolb, C., Kessler, S., Jimenez, J., Aiken, A., DeCarlo, P., Donahue, N., Wilson, K., Smith, J., Onasch, T., Canagaratna, M., and Ng, S.: Describing oxidation of organics using the AMS [PDF document], Retrieved from http://cires.colorado.edu/jimenez-group/UsrMtgs/UsersMtg10/kroll_AMSusersMeeting_2009.pdf, 2009b.

Kroll, J. H., Donahue, N. M., Jimenez, J. L., Kessler, S. H., Canagaratna, M. R., Wilson, K. R., Altieri, K., E., Mazzoleni, L. R., Wozniak, A. S., Bluhm, H., Mysak, E. R., Smith, J. D., Kolb, C. E., and Worsnop, D. R.: Carbon oxidation state as a metric for describing the chemistry of atmospheric organic aerosol, Nature Chemistry, 3, 133-139, doi: 10.1038/nchem.948, 2011.

Kulmala, M., Laaksonen, A., Korhonen, P., Vesala, T., Ahonen, T., and Barrett, J. C.: The effect of atmospheric nitric acid vapour on CCN activation, J. Geophys. Res., 98, 22949–22958, 1993.

Kulmala, M., Hämeri, K., Aalto, P., Mäkelä, J.M., Pirjola, L., Nilsson, E. D., Buzorius, G., Rannik, Ü., Dal Maso, M., Seild, W., Hoffmann, T., Jansson, R., Hansson, H.-C., Viisanen, Y., Laaksonen, A. and O'Dowd, C. D.: Overview of the international project on biogenic aerosol formation in the boreal forest (BIOFOR), Tellus, 53B, 324–343, 2001.

Kulmala, M., Suni, T., Lehtinen, K. E. J., Dal Maso, M., Boy, M., Reissell, A., Rannik, Ü., Aalto, P., Keronen, P., Hakola, H., Bäck, J., Hoffmann, T., Vesala, T., and Hari, P.: A new feedback mechanism linking forests, aerosols, and climate, Atmos. Chem. Phys., 4, 557–562, doi:10.5194/acp-4-557-2004, 2004.

Kulmala, M., Asmi, A., Lappalainen, H. K., Carslaw, K. S., Pöschl, U., Baltensperger, U., Hov, Ø., Brenquier, J.-L., Pandis, S. N., Facchini, M. C., Hansson, H.-C., Wiedensohler, A., and O'Dowd, C. D.: Introduction: European Integrated Project on Aerosol Cloud Climate and Air Quality interactions (EUCAARI) integrating aerosol research from nano to global scales, Atmos. Chem. Phys., 9, 2825–2841, doi:10.5194/acp-9-2825-2009, 2009.

Kumar, P. P., Broekhuizen, K., and Abbatt, J. P. D.: Organic acids as cloud condensation nuclei: Laboratory studies of highly soluble and insoluble species. Atmos. Chem. Phys., 3, 509–520, doi: 10.5194/acp-3-509-2003, 2003.

Kuwata, M., Kondo, Y., Mochida, M., Takegawa, N., and Kawamura, K.: Dependence of CCN activity of less volatile particles on the amount of coating observed in Tokyo, J. Geophys. Res., 112, D11207, doi: 10.1029/2006JD007758, 2007.

Kuwata, M., Shao, W., Lebouteiller, R., and Martin, S.T.: Classifying organic materials by oxygen-to-carbon elemental ratio to predict the activation regime of cloud condensation nuclei (CCN), Atmos. Chem. Phys., 13, 5309-5324, doi:10.5194/acp-13-5309-2013, 2013.

Lack, D. A., Cappa, C. D., Langridge, J., Bahreini, R., Buffaloe, G., Brock, C., Cerully, K., Coffman, D., Hayden, K., Holloway, J., Lerner, B., Massoli, P., Li, S.-M., McLaren, R., Middlebrook, A. M., Moore, R., Nenes, A., Nuaaman, I., Onasch, T. B., Peischl, J., Perring, A., Quinn, P. K., Ryerson, T., Schwartz, J. P., Spackman, R., Wofsy, S. C., Worsnop, D., Xiang, B., and Williams, E.: Impact of Fuel Quality Regulation and Speed Reductions on Shipping Emissions: Implications for Climate and Air Quality. Environ. Sci. Tech., 45, 9052-9060, 2011.

Lambe, A. T., Onasch, T. B., Massoli, P., Croasdale, D. R., Wright, J. P., Ahern, A. T., Williams, L. R., Worsnop, D. R., Brune, W. H., and Davidovits, P.: Laboratory studies of the chemical composition and cloud condensation nuclei (CCN) activity of secondary organic aerosol (SOA) and oxidixed primary organic aerosol (OPOA). Atmos. Chem. Phys., 11, 8913-8928, doi:10.5194/acp-11-8913-2011, 2011.

Lance, S.: Quantifying compositional impacts of ambient aerosol on cloud droplet formation, Published Doctoral Thesis, available at: http://etd.gatech.edu/theses/available/etd-11132007-175217/unrestricted/lance_sara_m_200712phd[1].pdf, 2007.

Lance, S., Nenes, A., and Rissman, T.: Chemical and dynamical effects on cloud droplet number: Implications for estimates of the aerosol indirect effect, J. Geophys. Res., 109, D22208, doi: 10.1029/2004JD004596, 2004.

Lance, S., Medina, J., Smith, J. N., and Nenes, A.: Mapping the operation of the DMT continuous flow CCN counter, Aerosol Sci. Technol., 40, 242–254, doi:10.1080/02786820500543290, 2006.

Lance, S., Nenes, A., Mazzoleni, C., Dubey, M. K., Gates, H., Varutbangkul, V., Rissmas, T. A., Murphy, S. M., Sorooshian, A., Flagan, R. C., Seinfeld, J. H., Feingold, G., and Jonsson, H. H.: Cloud condensation nuclei activity, closure, and droplet growth kinetics of Houston aerosol during the Gulf of Mexico Atmospheric Composition and Climate Study (GoMACCS), J. Geophys. Res., 114, D00F15, doi: 10.1029/2008JD011699, 2009.

Lanz, V. A., Alfarra, M. R., Baltensperger, U., Buchmann, B., Hueglin, C., and Prévôt, A. S. H.: Source apportionment of submicron organic aerosols at an urban site by factor analytical modelling of aerosol mass spectra, Atmos. Chem. Phys., 7, 1503-1522, doi:10.5194/acp-7-1503-2007, 2007.

Lathem, T. L., Kumar, P., Nenes, A., Dufek, J., Sokolik, I. N., Trail, M., and Russell, A.: Hygroscopic properties of volcanic ash, Geophys. Res. Lett., 38, L11802, doi: 10.1029/2011GL047298, 2011.

Lathem, T. L. and Nenes, A.: Water vapor depletion in the DMT Continuous Flow CCN Chamber: effects on supersaturation and droplet growth, Aerosol Sci. Technol., 45, 604–615, doi:10.1080/02786826.2010.551146, 2011.

Lathem, T. L., Beyersdorf, A. J., Thornhill, K. L., Winstead, E. L., Cubison, M. J., Hecobian, A., Jimenez, J. L., Weber, R. J., Anderson, B. E., and Nenes, A.: Analysis of CCN activity of Arctic aerosol and Canadian biomass burning during summer 2008, Atmos. Chem. Phys., **13**, 2735-2756, doi: 10.5194/acp-13-2735-2013, 2013.

Lee, B. H., Kostenidou, E., Hildebrandt, L. Riipinen, I., Engelhart, G. J., Mohr, C., DeCarlo, P. F., Mihalopoulos, N., Prevot, A. S. H., Baltensperger, U., and Pandis, S. N.: Measurement of the ambient organic aerosol volatility distribution: application during the Finokalia Aerosol Measurement Experiment (FAME-2008). Atmos. Chem. Phys., 10, 12149-12160, doi: 10.5194/acp-10-12149-2010, 2010.

Li, Z., Williams, A. L., and Rood, M. J.: Influence of Soluble Surfactant Properties on the Activation of Aerosol Particles Containing Inorganic Solute, J. Atmos. Sci., 55, 1859–1866, 1998.

Li, Z., Schwier, A. N., Sareen, N., and McNeill, V. F.: Reactive processing of formaldehyde and acetaldehyde in aqueous aerosol mimics: surface tension depression and secondary organic products, Atmos. Chem. Phys., 11, 11617-11629, doi: 10.5194/acp-11-11617-2011, 2011.

Lim, Y. B., Tan, Y., and Turpin, B. J.: Chemical insights, explicit chemistry, and yields of secondary organic aerosol from OH radical oxidation of methylglyoxal and glyoxal in the aqueous phase, Atmos. Chem. Phys., 13, 8651-8667, doi: 10.5194/acp-13-8651-2013, 2013.

Liu, B. Y. H., Pui, D. Y. H., Whitby, K. T., Kittelson, D. B., Kousaka, Y., and McKenzie, R. L.: The aerosol mobility chromatograph: A new detector for sulfuric acid aerosols, Atmos. Environ., 12, 99–104, 1978.

Massoli, P., Lambe, A. T., Ahern, A. T., Williams, L. R., Ehn, M., Mikkilä, Canagaratna, M. R., Brune,W. H., Onasch, T. B., Jayne, J. T., Petäjä, Kulmala, M., Laaksonen,

A., Kolb, C. E., Davidovits, P., and Worsnop, D. R.: Relationship between aerosol oxidation level and hygroscopic properties of laboratory generated secondary organic aerosol (SOA) particles, Geophys. Res. Lett., 37, L24801, doi: 10.1029/2010GL045258, 2010.

Medina, J., Nenes, A., Sotiropoulou, R.-E. P., Cotrell, L. D., Ziembia, L. D., Beckman, P. J., and Griffin, R. J.: Cloud condensation nuclei closure during the International Consortium for Atmospheric Research on Transport and Transformation 2004 campaign: Effects of size-resolved composition, J. Geophys. Res., 112, D10S31, doi: 10.1029/2006JD007588, 2007.

Meyer, N. K., Duplissy, J., Gysel, M., Metzger, A., Dommen, J., Weingartner, E., Alfarra, M. R., Prevot, A. S. H., Fletcher, C., Good, N., McFiggans, G., Jonsson, Å. M., Hallquist, M., Baltensperger, U., and Ristovski, Z. D.: Analysis of the hygroscopic and volatile properties of ammonium sulphate seeded and unseeded SOA particles, Atmos. Chem. Phys., 9, 721-732, doi: 10.5194/acp-9-721-2009, 2009.

Mochida, M., Nishita-Hara, C., Kitamori, Y., Aggarwal, S. G., Kawamura, K., Miura, K., and Takami, A.: Size-segregated measurements of cloud condensation nucleus activity and hygroscopic growth for aerosols at Cape Hedo, Japan, in spring 2008, J. Geophys. Res., 115, D21207, doi: 10.1029/2009JD013216, 2010.

Moore, R. H., and Nenes, A.: Scanning Flow CCN Analysis - A Method for Fast Measurements of CCN Spectra. Aerosol Sci. Technol., 43, 1192-1207, doi: 10.1080/0278682090328978, 2009.

Moore, R., Nenes, A., and Medina, J.: Scanning Mobility CCN Analysis – A method for fast measurements of size resolved CCN distributions and activation kinetics, Aerosol Sci. Tech., 44, 861–871, doi: 10.1080/02786826.2010.498715, 2010.

Moore, R. H., Bahreini, R., Brock, C. A., Froyd, K. D., Cozic, J., Holloway, J. S., Middlebrook, A. M., Murphy, D. M., and Nenes, A.: Hygroscopicity and Composition of Alaskan Arctic CCN During April 2008, Atmos. Chem. Phys., 11**,** 11807-11825, doi: 10.5194/acp-11-11807-2011, 2011.

Moore, R. H., Cerully, K., Bahreini, R., Brock, C. A., Middlebrook, A. M., and Nenes, A.: Hygroscopicity and composition of California CCN during summer 2010, J. Geophys. Res., 117, D00V12, doi: 10.1029/2011JD017352, 2012a.

Moore, R. H., Raatikainen, T., Langridge, J. M., Bahreini, R., Brock, C. A., Holloway, J. S., Lack, D. A., Middlebrook, A. M., Perring, A. E., Schwarz, J. P., Spackman, J. R., and Nenes, A.: CCN spectra, hygroscopicity, and droplet activation kinetics of secondary organic aerosol resulting from the 2010 Deepwater Horizon oil spill, Environ. Sci. Tech., 46, 3093-3100, doi: 10:1021/es203362w, 2012b.

Murphy, S. M., Agrawal, H., Sorooshian, A., Padró, L. T., Gates, H., Hersey, S., Welch, W. A., Jung, H., Miller, J. W., Cocker, D.R., Nenes, A., Jonsson, H., Flagan, R. C., and Seinfeld, J. H.: Comprehensive simultaneous shipboard and airborne characterization of exhaust from a modern container ship at sea, Environ. Sci. Technol., 43, 4626–4640, doi: 10.1021/es802413j, 2009.

Nemitz, E., Jimenez, J. L., Huffman, J. A., Ulbrich, I. M., Canagaratna, M. R., Worsnop, D. R., and Guenther, A. B.: An eddy-covariance system for the measurement of surface/atmosphere exchange fluxes of submicron aerosol chemical species – first application above an urban area, Aerosol Sci. Technol., 42, 636–657, doi: 10.1080/02786820802227352, 2008.

Nenes, A., Pilinis, C., and Pandis, S. N.: ISORROPIA: A New Thermodynamic Model for Multiphase Multicomponent Inorganic Aerosols, Aquat. Geochem., 4*, 1*23-152, doi: 10.1023/A%3A1009604003981, 1998.

Nenes, A., Chuang, P.Y., Flagan, R.C., and Seinfeld, J.H.: A theoretical analysis of cloud condensation nucleus (CCN) instruments. J. Geophys. Res., 106, 3449–3474, doi: 10.1029/2000JD900614, 2001.

Nenes, A., Ghan, S., Abdul-Razzak, H., Chuang, P. Y., Seinfeld, J. H.: Kinetic limitations on cloud droplet formation and impact on cloud albedo, Tellus, 53B, 133–149, doi:10.1034/j.1600-0889.2001.d01-12.x; 2001.

Nenes, A., Charlson, R. J., Facchini, M. C., Kulmala, M., Laaksonen, A., and Seinfeld, J. H.: Can chemical effects on cloud droplet number rival the first indirect effect?, Geophys. Res. Lett., 29, 1848, doi: 10.1029/2002GL015295, 2002.

Ng, N. L., Canagaratna, M. R., Zhang, Q., Jimenez, J. L., Tian, J., Ulbrich, I. M., Kroll, J. H., Docherty, K. S., Chhabra, P. S., Bahreini, R., Murphy, S. M., Seinfeld, J. H., Hildebrandt, L., Donahue, N. M., DeCarlo, P. F., Lanz, V. A., Prévôt, A. S. H., Dinar, E., Rudich, Y., and Worsnop, D. R.: Organic aerosol components observed in Northern Hemispheric datasets from Aerosol Mass Spectrometry, Atmos. Chem. Phys., 10, 4625-4641, doi: 10.5194/acp-10-4625-2010, 2010.

Nieminen, T., Manninen, H. E., Sihto, S.-L., Yli-Juuti, T., Mauldin III, R. L., Petäjä, T., Riipinen, I., Kerminen, V.-M., and Kulmala, M.: Connection of sulfuric acid to atmospheric nucleation in boreal forest, Environ. Sci. Technol., 43, 4715–4721, 2009.

Novakov, T., and Penner, J. E.: Large Contributions of Organic Aerosols to Cloud-Condensation Nuclei Concentrations. Nature, 365, 823–826, doi: 10.1038/365823a0, 2003.

Orsini, D. A., Wiedensohler, A., and Stratmann, F.: A New Volatility Tandem Differential Mobility Analyzer to Measure the Volatile Sulfuric Acid Aerosol Fraction. J. Atmos. Ocean. Tech., 16, 760-772, 1998.

Orsini, D., Y. Ma, A. Sullivan, B. Sierau, K. Baumann, and R. Weber, Refinements to the Particle-Into-Liquid Sampler (PILS) For Ground and Airborne Measurements Of Water Soluble Aerosol Composition, *Atm. Environ.*, *37*, 1243-1259, 2003.

Padró, L. T., Asa-Awuku, A., Morrison, R., and Nenes, A.: Inferring thermodynamic properties from CCN activation experiments: single-component and binary aerosols, Atmos. Chem. Phys., 7, 5263–5274, doi: 10.5194/acp-7-5263-2007, 2007.

Padró, L. T., Tkacik, D., Lathem, T., Hennigan, C., Sullivan, A.P., Weber, R.J., Huey, L.G., and Nenes, A.: Investigation of cloud condensation nuclei properties and droplet growth kinetics of the water-soluble aerosol fraction in Mexico City, J. Geophys. Res., 115, D09204, doi: 10.1029/2009JD013195, 2010.

Patankar, S. V.: Numerical heat transfer and fluid flow, New York, NY: McGraw-Hill, 1980.

Perry, R. H., and Green, D. W., eds.: Physical and Chemical Data, In *Perry's Chemical Engineers' Handbook*, 7th ed., McGraw-Hill, New York, 1997.

Petäjä, T., Kerminen, V.-M., Hämeri, K., Vaattovaara, P., Joutsensaari, J., Junkermann, W., Laaksonen, A., and Kulmala, M.: Effects of SO2 oxidation on ambient aerosol growth in water and ethanol vapours, Atmos. Chem. Phys., 5, 767–779, doi:10.5194/acp-5-767-2005, 2005.

Petters, M. D and Kreidenweis, S. M.: A single parameter representation of hygroscopic growth and cloud condensation nucleus activity, Atmos. Chem. Phys., 7, 1961–1971, doi:10.5194/acp-7-1961-2007, 2007.

Petters, M. D., Carrico, C. M., Kreidenweis, S. M., Prenni, A. J., DeMott, P. J., Collett Jr., J. L., and Moosmüller, H.: Cloud condensation nucleation activity of biomass burning aerosol, J. Geophys. Res., 114, D22205, doi:10.1029/2009JD012353, 2009a.

Petters, M. D., Wex, H., Carrico, C. M., Hallbauer, E., Massling, A., McMeeking, G. R., Poulain, L., Wu, Z., Kreidenweis, S. M., and Stratmann, F.: Towards closing the gap between hygroscopic growth and activation for secondary organic aerosol – Part 2: Theoretical approaches, Atmos. Chem. Phys., 9, 3999-4009, doi:10.5194/acp-9-3999-2009, 2009b.

Pope, F. D., Tong, H., Dennis-Smither, B. J., Griffiths, P. T., Clegg, S. L., Reid, J. P., and Cox, R. A.: Studies of single aerosol particles containing malonic acid, glutaric

acid, and their mixtures with sodium chloride. II. Liquid-state vapor pressures of the acids. J. Phys. Chem. A., 114, 10156-10165, doi:10.1021/jp1052979, 2010.

Pöschl, U., Martin, S. T., Sinha, B., Chen, Q., Gunthe, S. S., Huffman, J. A., Borrmann, S., Farmer, D. K., Garland, R. M., Helas, G., Jimenez, J. L., King, S. M., Manzi, A., Mikhailov, E., Pauliquevis, T., Petters, M. D., Prenni, A. J., Roldin, P., Rose, D., Schneider, J., Su, H., Zorn, S. R., Artaxo, P., and Andreae, M. O.: Rainforest aerosols as biogenic nuclei of cloud and precipitation in the Amazon, Science, 329, 1513–1516, doi:10.1126/science.1191056, 2010.

Pöschl, U.: Gas-particle interactions of tropospheric aerosols: Kinetic and thermodynamic perspectives of multiphase chemical reactions, amorphous organic substances, and the activation of cloud condensation nuclei, Atmos. Res., 101, 562–573, doi:10.1016/j.atmosres.2010.12.018, 2011.

Poulain, L., Wu., Z., Petters, M. D., Wex, H., Hallbauer, E., Wehner, B., Massling, A., Kreidenweis, S. M., and Stratmann, F.: Towards closing the gap between hygroscopic growth and CCN activation for secondary organic aerosol – Part 3: Influence of the chemical composition on the hygroscopic properties and volatile fractions of aerosol, Atmos. Chem. Phys. 10, 3775-3785, 2010.

Prenni, A. J., DeMott, P. J., Kreidenweis, S. M., and Sherman, D. E.: The effects of low molecular weight dicarboxylic acids on cloud formation. J. Phys. Chem. A., 105, 11240–11248, doi: 10.1021/jp012427d, 2001.

Prenni, A. J., Petters, M. D., Kreidenweis, S. M., DeMott, P. J., and Ziemann, P. J.: Cloud droplet activation of secondary organic aerosol, J. Geophys. Res., 112, D10223, doi: 10.1029/2006JD007963, 2007.

Pringle, K. J., Tost, H., Pozzer, A., Pöschl, U., and Lelieveld, J.: Global distribution of the effective aerosol hygroscopicity parameter for CCN activation, Atmos. Chem. Phys., 10, 5241-5255, doi:10.5194/acp-10-5241-2010, 2010.

Pye, H. O. T., and Seinfeld, J. H.: A global perspective on aerosol from low-volatility organic compounds. Atmos. Chem. Phys., 10, 4377-4401, doi: 10.5194/acp-10-4377-2010, 2010.

Raatikainen, T., Vaattovaara, P., Tiitta, P., Miettinen, P., Rautiainen, J., M. Ehn, M., Kulmala, M., Laaksonen, A., and Worsnop, D. R.: Physicochemical properties and origin of organic groups detected in boreal forest using an aerosol mass spectrometer, Atmos. Chem. Phys., 10, 2063–2077, doi: 10.5194/acp-10-2063-2010, 2010.

Raatikainen, T., Lin, J. J, Cerully, K., Lathem, T. L., Moore, R. H. and Nenes, A.: CCN data interpretation under dynamic operation conditions, Aerosol Sci. Tech., *in review*.

Rader, D. J. and McMurry, P. H.: Application of the tandem differential mobility analyzer to studies of droplet growth or evaporation, J. Aerosol Sci., 17, 771–787, 1986.

Ravindran, P., Davis, E. J., and Ray, A. K.: Diffusivities of low-volatility species in light gases. AIChE J., 25, 966-975, doi:10.1002/aic.690250607, 1979.

Raymond, T. and Pandis, S. N.: Cloud activation of single-component organic aerosol particles, J. Geophys. Res., 107, 4787, doi: 10.1029/2002JD002159, 2002.

Raymond, T. M., and Pandis, S. N.: Formation of cloud droplets by multicomponent organic particles. J. Geophys. Res., 108, 4469, doi: 10.1029/2003JD003503, 2003.

Reynolds, J. C., Last, D. J., McGillen, M., Nijs, A., Horn, A. B., Percival, C., Carpenter, L. J., and Lewis, A. C.: Structural analysis of oligomeric molecules formed from the reaction products of oleic acid ozonolysis, Environ. Sci. Technol., 40, 6674–6681, doi: 10.1021/es060942p, 2006.

Riipinen, I., Koponen, I. K., Frank, G. P., Hyvarinen, A.-P., Vanhanen, J., Lihavainen, H., Lehtinen, K. E. J., Bilde, M.., and Kulmala, M..: Adipic and malonic acid aqueous solutions: surface tensions and saturation vapor pressures. J. Phys. Chem., 111, 12995–13002, doi: 10.1021/jp073731v, 2007.

Riipinen, I., Pierce, J. R., Donahue, N. M., and Pandis, S. N.: Equilibration time scales of organic aerosol inside thermodenuders: Evaporation kinetics versus thermodynamics. Atmos. Environ., 44, 597-607, doi: 10.1016/j.atmosenv.2009.11.022, 2010.

Riipinen, I., Pierce, J. R., Yli-Juuti, T., Nieminen, T., Häkkinen, S., Ehn, M., Junninen, H., Lehtipalo, K., Petäjä, T., Slowik, J., Chang, R., Shantz, N. C., Abbatt, J., Leaitch, W. R., Kerminen, V.-M., Worsnop, D. R., Pandis, S. N., Donahue, N. M., and Kulmala, M.: Organic condensation: a vital link connecting aerosol formation to cloud condensation nuclei (CCN) concentrations. Atmos. Chem. Phys., 11, 3865-3878. doi: 10.5194/acp-11-3865-2011, 2011.

Rissman, T.A., Varutbangkul, V., Surratt, J.D., Topping, D.O., McFiggans, G., Flagan, R.C., and Seinfeld, J.H.: Cloud condensation nucleus (CCN) behavior of organic aerosol particles generated by atomization of water and methanol solutions, Atmos. Chem. Phys., 7, 2949-2971, doi:10.5194/acp-7-2949-2007, 2007.

Roberts, G. and Nenes, A.: A Continuous-Flow Streamwise Thermal-Gradient CCN Chamber for atmospheric measurements, Aerosol Sci. Technol., 39, 206–221, doi: 10.1080/027868290913988, 2005.

Roelofs, G. J.: A GCM study of organic matter in marine aerosol and its potential contribution to cloud drop activation. Atmos. Chem. Phys., 8, 709-719, doi: 10.5194/acp-8-709-2008, 2008.

Rose, D., Gunthe, S. S., Mikhailov, E., Frank, G. P., Dusek, U., Andreae, M. O., and Pöschl, U.: Calibration and measurement uncertainties of a continuous-flow cloud condensation nuclei counter (DMT-CCNC): CCN activation of ammonium sulfate and sodium chloride aerosol particles in theory and experiment, Atmos. Chem. Phys., 8, 1153–1179, doi:10.5194/acp-8-1153-2008, 2008.

Rose, D., Nowak, A., Achtert, P., Wiedensohler, A., Hu, M., Shao, M., Zhang, Y., Andreae, M. O., and Pöschl, U.: Cloud condensation nuclei in polluted air and biomass burning smoke near the mega-city Guangzhou, China - Part 1: Size-resolved measurements and implications for the modeling of aerosol particle hygroscopicity and CCN activity, Atmos. Chem. Phys., 10, 3365–3383, doi:10.5194/acp-10-3365-2010, 2010.

Ruehl, C. R., Chuang, P. Y., and Nenes, A.: How quickly do cloud droplets form on atmospheric particles?, Atmos. Chem. Phys., 8, 1043–1055, doi:10.5194/acp-8-1043-2008, 2008.

Ruehl, C. R., Chuang, P. Y. and Nenes, A.: Distinct CCN activation kinetics above the marine boundary layer along the California coast, Geophys. Res. Let., 36, L15814, doi: 10.1029/2009GL038839, 2009.

Ruehl, C. R., Chuang, P. Y., and Nenes, A.: Aerosol hygroscopicity at high (99 to 100%) relative humidities, Atmos. Chem. Phys., 10, 1329-1344, doi: 10.5194/acp-10-1329-2010, 2010.

Ruehl, C. R., Chuang, P. Y., Nenes, A., Cappa, C. D., Kolesar, J. R., and Goldstein, A. H.: Strong evidence of surface tension reduction in microscopic aqueous droplets, Geophys. Res. Let., 39, L23801, doi: 10.1029/2012GL053706, 2012.

Saleh, R., Shihadeh A., and Khlystov, A.: Determination of evaporation coefficients of semi-volatile organic aerosols using an integrated volume—tandem differential mobility analysis (IV-TDMA) method. J. Aerosol Sci., 40, 1019-1029, doi: 10.1080/02786826.2011.602762, 2009.

Saleh, R., Shihadeh, A., and Khlystov, A.: Effect of aerosol generation method on measured saturation pressure and enthalpy of vaporization of dicarboxylic acid aerosols. Aerosol Sci. Technol., 44, 302–307, doi: 10.1080/02786821003591810, 2010.

Saleh, R., Shihadeh, A., and Khlystov, A.: On transport phenomena and equilibration time scales in thermodenuder. Atmos. Meas. Tech., 4, 571-581, doi: 10.5194/amt-4-571-2011, 2011.

Saleh, R., Khlystov, A., and Shihadeh, S.: Determination of evaporation coefficients of ambient and laboratory-general semivolatile organic aerosols from phase equilibration kinetics in a thermodenuder. Aeros. Sci. Tech., 46, 22-30, doi: 10.1080/02786826.2011.602762, 2012.

Salo, K., Jonsson, A. M., Andersson, P. U., and Hallquist, M.: Aerosol Volatility and Enthalpy of Sublimation of Carboxylic Acids. J. Phys. Chem. A., 114, 4586−4594, doi: 10.1021/jp910105h, 2010.

Salo, K., Hallquist, M., Jonsson, Å. M., Saathoff, H., Naumann, K.-H., Spindler, C., Tillmann, R., Fuchs, H., Bohn, B., Rubach, F., Mentel, Th. F., Müller, L., Reinnig, M., Hoffmann, T., and Donahue, N. M.: Volatility of secondary organic aerosol during OH radical induced ageing. Atmos. Chem. Phys., 11, 11055-11067, doi: 10.5194/acp-11-11055-2011, 2011.

Sareen, N., Schwier, A. N., Shapiro, E. L., Mitroo, D., and McNeill, V. F.: Secondary organic material formed by methylglyoxal in aqueous aerosol mimics, Atmos. Chem. Phys., 10, 997-1016, doi: 10.5194/acp-10-997-2010, 2010.

Sareen, N., Schwier, A. N., Lathem, T. L., Nenes, A., McNeill, V. F.: Surfactants from the gas phase may promote cloud droplet formation, PNAS, 110, 2723-2728, doi: 10.1073/pnas.1204838110, 2013.

Schwier, A. N., Sareen, N., Lathem, T. L., Nenes., A., and McNeill, V. F.: Ozone oxidation of oleic acid surface films decreases aerosol cloud condensation nuclei activity, J. Geophys., Res., 116, D16202, doi: 10.1029/2010JD015520, 2011.

Seinfeld, J. H. and Pandis, S. N.: Atmospheric Chemistry and Physics: From Air Pollution to Climate Change, 2, John Wiley & Sons, Inc., Hoboken, NJ, 2006.

Shulman, M. L., Jacobson, M. C., Carlson, R. J., Synovec, R. E., and Young, T. E.: Dissolution behavior and surface tension effects of organic compounds in nucleating cloud droplets, Geophys. Res. Let, 23, 277–280, doi: 10.1029/95GL03810, 1996.

Sihto, S.-L., Mikkilä, J., Vanhanen, J., Ehn, M., Liao, L., Lehtipalo, K., Aalto, P. P., Duplissy, J., Petäjä, T., Kerminen, V.-M., Boy, M., and Kulmala, M.: Seasonal variation of CCN concentrations and aerosol activation properties in boreal forest, Atmos. Chem. Phys., 11, 13269-13285, doi:10.5194/acp-11-13269-2011, 2011.

Soonsin, V., Zardini, A. A., Marcolli, C., Zuend, A., and Krieger, U. K.: The vapor pressures and activities of dicarboxylic acids reconsidered: the impact of the physical state of the aerosol. Atmos. Chem. Phys. 10, 11753-11767, doi: 10.5194/acp-10-11753-2010, 2010.

Sorooshian, A., Murphy, S. M., Hersey, S., Gates, H., Padró, L. T., Nenes, A., Brechtel, F. J., Jonsson, H., Flagan, R. C., and Seinfeld, J. H.: Comprehensive airborne characterization of aerosol from a major bovine source, Atmos. Chem. Phys., 8, 5489-5520, doi:10.5194/acp-8-5489-2008, 2008.

Su, H., Rose, D., Cheng, Y. F., Gunthe, S. S., Massling, A., Stock, M., Wiedensohler, A., Andreae, M. O., and Pöschl, U.: Hygroscopicity distribution concept for measurement data analysis and modeling of aerosol particle mixing state with regard to hygroscopic growth and CCN activation, Atmos. Chem. Phys., 10, 7489–7503, doi:10.5194/acp-10-7489-2010, 2010.

Sullivan, R. C., Moore, M. J. K., Petters, M. D., Kreidenweis, S. M., Roberts, G. C., and Prather, K. A.: Effect of chemical mixing state on the hygroscopicity and cloud nucleation properties of calcium mineral dust particles, Atmos. Chem. Phys., 9, 3303-3316, doi: 10.5194/acp-9-3303-2009, 2009.

Sun, J. and Ariya, P. A.: Atmospheric Organic and Bio-aerosols as Cloud Condensation Nuclei (CCN): A Review, Atmos. Environ., 40, 795-820, 2006.

Swietlicki, E., Hansson, H.-C., Hämeri, K., Svenningsson, B., Massling, A., McFiggans, G., McMurry, P.H., Petäjä, T., Tunved, P., Gysel, M., Topping, D., Weingartner, E., Baltensperger, U., Rissler, J., Wiedensohler, A. and Kulmala, M.: Hygroscopic properties of sub-micrometer atmospheric aerosol particles measured with H-TDMA instruments in various environments – a review, Tellus, 60B, 432–469, 2008.

Tang, X., Cocker III, D. R., and Asa-Awuku, A.: Are sesquiterpenes a good source of secondary organic cloud condensation nuclei (CCN)? Revisiting β-caryophyllene CCN, Atmos. Chem. Phys., 12, 8377-8388, doi: 10.5194/acp-12-8377-2012, 2012.

Tao, Y., and McMurry, P.: Vapor pressures and surface free energies of C14-C18 monocarboxylic acids and C5 and C6 dicarboxylic acids. Environ. Sci. Technol., 23, 1519, 1989.

Topping, D. O., McFiggans, G. B., Kiss, G., Varga, Z., Facchini, M. C., Decesari, S., and Mircea, M.: Surface tensions of multi-component mixed inorganic/organic aqueous systems of atmospheric significance: measurements, model predictions and importance for cloud activation predictions, Atmos. Chem. Phys., 7, 2371-2398, doi: 10.5194/acp-7-2371-2007, 2007.

Tritscher, T., Dommen, J., DeCarlo, P.F., Gysel, M., Barmet, P. B., Praplan, A. P., Weingartner, E., Prévôt, A. S. H., Riipinen, I., Donahue, N. M., and Baltensperger, U.: Volatility and hygroscopicity of aging secondary organic aerosol in a smog chamber, Atmos. Chem. Phys., 11, 11477-11496, doi:10.5194/acp-11-11477-2011, 2011.

Twomey, S.: Pollution and the planetary albedo, Atmos. Environ., 8, 1251–1256, 1974.

Twomey, S.: The influence of pollution on the shortwave albedo of clouds, J. Atmos. Sci., 34, 1149–1152, 1977.

Väkevä, M., Kulmala, M., Stratmann, F., and Hämeri, K.: Field measurements of hygroscopic properties and state of mixing of nucleation mode particles, Atmos. Chem. Phys., 2, 55–66, doi:10.5194/acp-2-55-2002, 2002.

VanReken, T. M., Ng, N. L., Flagan, R. C., and Seinfeld, J. H.: Cloud condensation nucleus activation properties of biogenic secondary organic aerosol, J. Geophys. Res., 110, d07206, doi: 10.1029/2004JD005465, 2005.

Varutbangkul, V., Brechtel, F. J., Bahreini, R., Ng, N. L., Keywood, M. D., Kroll, J. H., Flagan, R. C., Seinfeld, J. H., Lee, A., and Goldstein, A. H.: Hygroscopicity of secondary organic aerosols formed by oxidation of cycloalkenes, monoterpenes, sesquiterpenes, and related compounds, Atmos. Chem. Phys., 6, 2367-2388, doi:10.5194/acp-6-2367-2006, 2006.

Villani, P., Sellegri, K., Monier, M., and Laj, P.: Influence of semi-volatile species on particle hygroscopic growth, Atmos. Environ., 79, 129-173, 2013.

Virtanen, A., Joutsensaari, J., Koop, T., Kannosto, J., Yli-Pirila, P., Leskinen, J., Makela, J. M., Holopainen, J. K., Poeschl, U., Kulmala, M., Worsnop, D. R., and Laaksonen, A.: An amorphous solid state of biogenic secondary organic aerosol particles. Nature, 467, 824-827, doi: 10.1038/nature09455, 2010.

Wang, S. C. and Flagan, R. C.: Scanning Electrical Mobility Spectrometer, Aerosol Sci. Technol., 13, 230–240, 1990.

Weber, R. J., Orsini, D., Daun, Y., Lee, Y.-N., Klotz, P., and Brechtel, F.: A particle-into-liquid collector for rapid measurements of aerosol chemical composition, Aeros. Sci. Tech., *35*, 718-727, 2001.

Wehner, B., Philippin, S., and Wiedensohler, A.: Design and calibration of a thermodenuder with an improved heating unit to measure the size-dependent volatile fraction of aerosol particles. J. Aerosol Sci., 33, 1087-1093, doi: 10.1016/s0021-8502(02)00056-3, 2002.

Wex, H., Petters, M. D., Carrico, C. M., Hallbauer, E., Massling, A., McMeeking, G. R., Poulain, L., Wu, Z., Kreidenweis, S. M., and Stratmann, F.: Towards closing the gap between hygroscopic growth and activation for secondary organic aerosol: Part 1 – Evidence from measurements, Atmos. Chem. Phys., 9, 3987-3997, doi:10.5194/acp-9-3987-2009, 2009.

White, S. J., Jamie, I. M., Angove, D. E.: Chemical characterisation of semi-volatile and aerosol compounds from the photooxidation of toluene and NO_x, Atmos. Environ., 83, 237-244, 2014.

Wiedensohler, A. and Fissan, H. J.: Aerosol charging in high purity gases, J. Aerosol Sci., 19, 867–870, 1988.

Xu, L., Kollman, M., Song, C., Shilling, J., and Ng, N. L.: Effects of NOx on the volatility of secondary organic aerosol from isoprene photooxidation, Environ. Sci. Tech., *in review*.

Yaws, C. L.: Yaws' Handbook of thermodynamic and physical properties of chemical compounds. Knovel, in section: Surface Tension. Online version available at: http://app.knovel.com/hotlink/toc/id:kpYHTPPCC4/yaws-handbook-thermodynamic, 2003.

Yu, S.: Role of Organic Acids (Formic, Acetic, Pyruvic and Oxalic) in the Formation of Cloud Condensation Nuclei (CCN): a Review, Atmos. Rev., 53, 185-217, 2007.

Zuend, A. and Seinfeld, J. H.: Modeling the gas-particle partitioning of secondary organic aerosol: the importance of liquid-liquid phase separation, Atmos. Chem. Phys., 12, 3857-3882, doi: 10.5194/acp-12-3857-2012, 2012.